A new look at the nature of the transitional layer at the K/T boundary near Gams, Eastern Alps, Austria, and the problem of the mass extinction of the biota

A. F. Grachev[1], O. A. Korchagin[2], H. A. Kollmann[3], D. M. Pechersky[1], and V. A. Tsel'movich[1]

[1] The results of detailed biostratigraphic, lithological, isotopic–geochemical, and petromagnetic analysis of the sedimentary sequence at the Cretaceous–Paleogene boundary in the Gams area, Eastern Alps, Austria, point to two stages in the evolution of the transitional layer at the Cretaceous–Paleogene boundary. During the earlier one of these stages (which lasted for approximately 1500 years, as follows from conservative estimates of the sedimentation rate), the transitional layer was formed under the effect of volcanic aerosol. The later one caused the presence of titanomagnetite, gold, and copper, as well as high concentrations of Ir, As, Pb, Cr, and other elements in the rocks. The occurrence of an Ir anomaly in the lower part of the transitional layer and the presence of titanomagnetite, Cu, and Au in it were related to volcanic activity. During the later stage, the character of sedimentation was affected by the fall of an asteroid (meteorite), and traces of its material are discernible as beads of metallic Ni, awaruite, and diamond crystals. The conclusions drawn from the results of our analysis principally differ from all preexisting data on the transitional layer between the Cretaceous and Paleogene and provide another look at the reasons for the mass extinction of living organisms at 65 Ma. These data eliminate the need for opposing volcanism to an impact event: both took place, but the changes in the biota were induced by volcanism, as also was the appearance of the Ir anomaly itself, whereas the fall of a cosmic body occurred approximately 500–800 years later. *INDEX TERMS:* 1051 Geochemistry: Sedimentary geochemistry; 1519 Geomagnetism and Paleomagnetism: Magnetic mineralogy and petrology; 1630 Global Change: Impacts of global change; *KEYWORDS:* K/T boundary, volcanism, impact event, Eastern Alps.

Introduction

[2] The discovery of anomalies of Ir and other platinum-group elements in clays at the boundary between the Cretaceous and Paleogene (the so-called Cretaceous–Tertiary, or K/T, boundary) [*Alvarez et al.,* 1980, 1984; *Ganapathy et al.,* 1981; *Preisinger et al.,* 1986; *Smit and Hertogen,* 1980] gave rise to the paradigm that the mass extinction of the biota was induced by an impact event and had been an impetus for studying this boundary throughout the world. This hypothesis was supported by the reasonable idea that high Ir concentrations, much higher than those know in terrestrial rocks, were related to the fall of a meteorite (or an asteroid) [*Alvarez et al.,* 1980].

[3] The establishment of the impact paradigm of the mass extinction of the biota was facilitated by the discovery of the world's largest Chicxulub meteoritic crater in Yucatan, Mexico [*Hildebrand et al.,* 1991; *Smith et al.,* 1992]. Moreover, some rock units at the K/T boundary were found out to bear shocked quartz and coesite [*Bohor et al.,* 1984; *Koebler,* 1997; *Preisinger et al.,* 1986; and several others].

[4] Later papers by *Alvarez et al.* [1980] demonstrated that the Ir anomaly in the transitional layer at the K/T boundary was present in virtually all of the inspected rock sequences, both in continents and in deep-sea drilling holes in oceans [*Alvarez et al.,* 1992; *Hsu et al.,* 1982; *Kyte and Bostwick,* 1995; and several others]. The problem of the mass extinction of the biota at the Cretaceous–Paleogene bound-

---

[1]Institute of Physics of the Earth, Moscow, Russia
[2]Geological Institute, Russian Academy of Sciences, Moscow, Russia
[3]National Museum of Natural History, Vienna, Austria
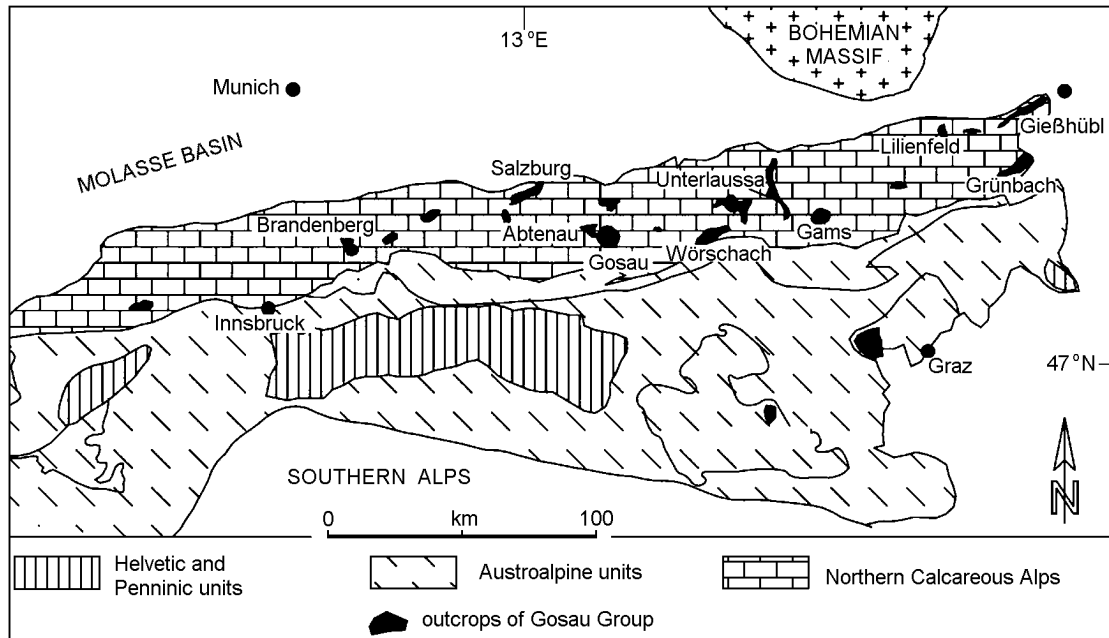
Figure 1. Localities of the Gosau Group of the Northern Calcareous Alps within the Eastern Alps [*Wagreich and Krenmayr, 2005*].

ary seemed to be resolved, although an almost unanimous consensus was distorted by several researchers who doubted the validity of the impact hypothesis and put forth arguments in support of magmatic (related to a mantle plume volcanism) reasons for the development of the transitional layer [*Officer and Drake,* 1985; *Officer et al.,* 1987; *Zoller et al.,* 1983]. In particular, several scientists pointed to data on the multiplicity of Ir anomalies and the possibility of explaining the unusual geochemistry of the transitional layer at the K/T boundary by the effect of volcanic activity [*Officer et al.,* 1987]. Research in early 1990s provided new, more detailed information on transitional layers at the K/T boundary. Along with new finds of shocked quartz in the transitional layers of different regions of the world, such high-pressure minerals as coesite and stishovite were found, as well as spinel with high (>5%) Ni concentrations and diamond [*Carlisle and Braman,* 1991; *Hough et al.,* 1997; *Leroux et al.,* 1995; *Preisinger et al.,* 2002]. Although all of these materials considered together provided irrefutable evidence of an impact event, the mechanisms relating it to the mass extinction of the biota remained uncertain.

[5] Meanwhile newly obtained data were amassing that indicated that Ir anomalies could occur both below and above the K/T boundary [*Ellwood et al.,* 2003; *Graup and Spettel,* 1989; *Tandon,* 2002; *Zhao et al.,* 2002; and others]. Furthermore, Ir anomalies were found in rocks with no relation at all to the Cretaceous–Paleogene boundary [*Dolenec et al.,* 2000; *Keller and Stinnesbeck,* 2000; and others]. Hence, the Ir anomaly itself, which was originally considered one of the milestone of the impact hypothesis for the mass extinction of living organisms at the K/T boundary [*Alvarez et al.,* 1980], could not be anymore (in light of newly obtained data) regarded as a geochemical indicator of such phenomena. It is also pertinent to recall that data on the Permian–Triassic

boundary also did not confirm that the reasons for the extinction of that biota were of an impact nature [*Zhou and Kyte,* 1988].

[6] The idea that the fundamental changes in the biota at the K/T boundary were related to volcanic processes became topical again [*Grachev,* 2000a, 2000b], particularly after the detailed studying of anomalies of Ir and other PGE in plume-related basalts in Greenland, at the British Islands, and Deccan [*Crocket and Paul,* 2004; *Phillip et al.,* 2001; *Power et al.,* 2003], which made it possible to explain the high Ir concentrations in sediments by the transportation of this element by aerosols during volcanic eruptions, as was earlier hypothesized in [*Zoller et al.,* 1983].

[7] All of these discrepancies became so obvious that W. Alvarez, one of the main proponents of the impact hypothesis, admitted that "...although I have long been a proponent of impact at the K/T boundary, I hold no grief for all extinctions being caused by impact. If the evidence for a flood-extinction link is compelling, we should accept that conclusion" [*Alvarez,* 2002, p. 3]. He also wrote: "It would be useful to the community of researchers to have a compilation of evidence for impact and for volcanism at prominent extinction levels. This is probably something that should be prepared by a group of workers experienced in the field" [*Alvarez,* 2002, p. 4].

[8] It is also worth mentioning two other approaches to the problem of relations between impact events and plume magmatism.

[9] In one of them, an attempt was undertaken to relate the onset of plume magmatism to the decompression and melting of deep lithospheric layers under the effect of the development of craters about 100 km diameter. Here the impact itself is considered to be a triggering mechanism for the origin of a plume [*Jones et al.,* 2003; and others]. Aside from

the implausibility of this process from the physical standpoint [*Molodenskii,* 2005, in press], there is direct and only one evidence of the impossibility of this process: the He isotopic signature of plume basalts. As it is well known, these basalts have a ^{3}He/^{4}He ratio more than $20{\times}10^{-6}$, which could be caused by the uprise of the melts from depths of more than 670 km, i.e., from the lower mantle or, more probably, from the core/mantle boundary (D″ layer) [*Grachev,* 2000b and references therein].

[10] In the latter instance, perhaps because no scientifically plausible resolution of the mass extinction could be found, it was proposed to regard mass extinction in the Phanerozoic as an accidental coincidence with coeval plume magmatism and impact events [*White and Saunders,* 2005].

[11] Nevertheless, the problem remains unsettled as of yet. How can one explain the fact that the study of the transitional layers at the K/T boundary over the past 25 years, with the use of state-of-the-art analytical equipment and techniques, did not result in the solution of this problem?

[12] In our opinion, the answer to this question stems from the methods employed in these studies: the layer was inspected as a single whole, and its characteristics obtained with different techniques were ascribed to the whole thickness of this rock unit. At the thickness of the transitional layer at the K/T boundary varying from 1 cm [*Preisinger et al.,* 1986] to 20 cm [*Luciani,* 2002], sampling sites were commonly spaced 5–10 cm apart, or 1–2 cm apart near the boundary [*Gardin,* 2002; *Keller et al.,* 2002b and others]. With regard to the known sedimentation rates of about 2 cm per 1000 years [*Stuben et al.,* 2002 and references therein], the transitional layers should have been produced over time spans from 500 to 10,000 years.

[13] The time during which an impact event could affect the character of sedimentation can be estimated from the numerical simulations of the nuclear winter scenario, according to which the duration of this event at the Earth's surface should range from 10 to 30 days [*Turko et al.,* 1984]. Because of this, even if such events took place in the geologic past, and even if some records of them could be discerned in sediments, evidence of these events cannot be identified visually but require a detailed and scrupulous investigation.

[14] The most interesting known stratigraphic successions in the Eastern Alps the boundary for which between the Cretaceous and Paleogene is considered proved faunistically are three localities in which transitional layers were determined to have Ir anomalies. One of them is situated not far from Gosau, southeast of Salzburg [*Preisinger et al.,* 1986], in the Ellengraben, near the village of Rusbach. Another one is located in the Bavarian Alps, southwest of Salzburg [*Graup and Spettel,* 1989], and the third one lies east of the village of Gams in Styria, where the Gams River and other streams in some places exposes the K/T boundary [*Lahodynsky,* 1988] (Figure 1).

[15] In the first sections, the transitional layer is 1 cm thick [*Preisinger et al.,* 1986], but we failed to identify and sample it in the field. The second locality is characterized by stratigraphic gaps, and it is unclear whether the stratigraphic succession is continuous [*Graup and Spettel,* 1989]. An exposure most suitable for studying the transitional layer at the K/T boundary is the third one, in the vicinity of Gams, which

Table 1. Interrelationship of the selected samples for different kinds of analyses

1	2	3	4	5	6
J-1/E$_{1,3}$	J-2/6	J-6/6	J-10/c	J-11/c	J-8/9c
	J-2/5	J-6/5			
				J-11/b-c	
J-1/C$_2$	J-2/4	J-6/4	J-10/b	J-11/b	J-8/9b
	J-2/3	J-6/3			
				J-11/a-b	
J-1/B$_2$	J-2/2	J-6/2	J-10/a	J-11/a	J-8/9a
J-1/A$_3$	J-2/1	J-6/1			

Note: 1 – carbon and oxygen isotope analysis, 2 – MS-ICP analysis, 3 – microprobe and petromagnetic analysis, 4 – clay minerals analysis, 5 – Ir and other trace elements and He isotope analysis, 6 – micropaleontological analysis.

is now under the protection of UNESCO. A monolithic rock block from this stratigraphic sequence was made available for us for studying under the supervision of the administration of the Museum of Natural History in Vienna.

[16] This publication is presents the results of the detailed and complex examination of boundary layer in the Gams area.

General Characterization the Gams Stratigraphic Succession

[17] The general setting of the stratigraphic sequence in the Gams area (Knappengraben) was characterized by *Lahodynsky* [1988], who determined that it belonged to the Nierental Formation (chron 29R). The part of the sequence below the transitional layer at the K/T boundary consists of alternating calcareous marlstone and marly limestone, and the transitional clay layer is overlain by a clay-dominated unit with variable proportions of Ca carbonate and occasional sandstone–siltstone intercalations. The transitional clay layer at the K/T boundary is enriched in smectite and has elevated concentrations of Ir (up to 10 ppb), Cr, Co, Ni, MgO, Al$_2$O$_3$, and TiO$_2$ [*Lahodynsky,* 1988]. The aforementioned paper presents no data on the faunal characteristics of the layer, neither does it describe any factual materials on the major- and trace-element chemistry concentrations or information on the analytical techniques.

[18] The monolithic rock block that was cut out of the exposure and that includes the clearly pronounced K/T boundary has a height of 46 cm and a widths of 30 cm at the bottom and 22 cm at the top; the thickness of the monolith is

Figure 2. General view of the Gams section monolith (photograph).

4 cm (Figure 2, Table 1). To obtain the general characteristics of the sequence, the monolith was divided into 2-cm units, which were labelled A through W from bottom to top (Figure 3), and each of the units was then marked from (1, 2, 3, and so on) at intervals of 2 cm. Transitional layer J at the K/T boundary was examined more thoroughly. It was subdivided into a number of units approximately 3 mm thick each (Figure 4).

[19] According to the decision of the International Union of Geological Sciences, the boundary between the Cretaceous and Paleogene, or the lower boundary of the Danian stage

of the Paleogene is determined by the Ir anomaly proximal to the mass extinction of typical Cretaceous faunal groups (foraminifers, nannoplankton, dinosaurs, etc.). The global stratotype of this boundary (GSSP) was chosen to be the El-Kef sequence in Tunisia "In the El-Haria section near El-Kef, Tunisia, at the base of the boundary clay" [*Cowie et al.,* 1989].

[20] In compliance with this, we drew the Cretaceous–Paleogene boundary in the Gams sequence in the Alps, Austria, through the middle part of clayey layer J, which is enriched in Ir, rests immediately on marls and clayey lime-
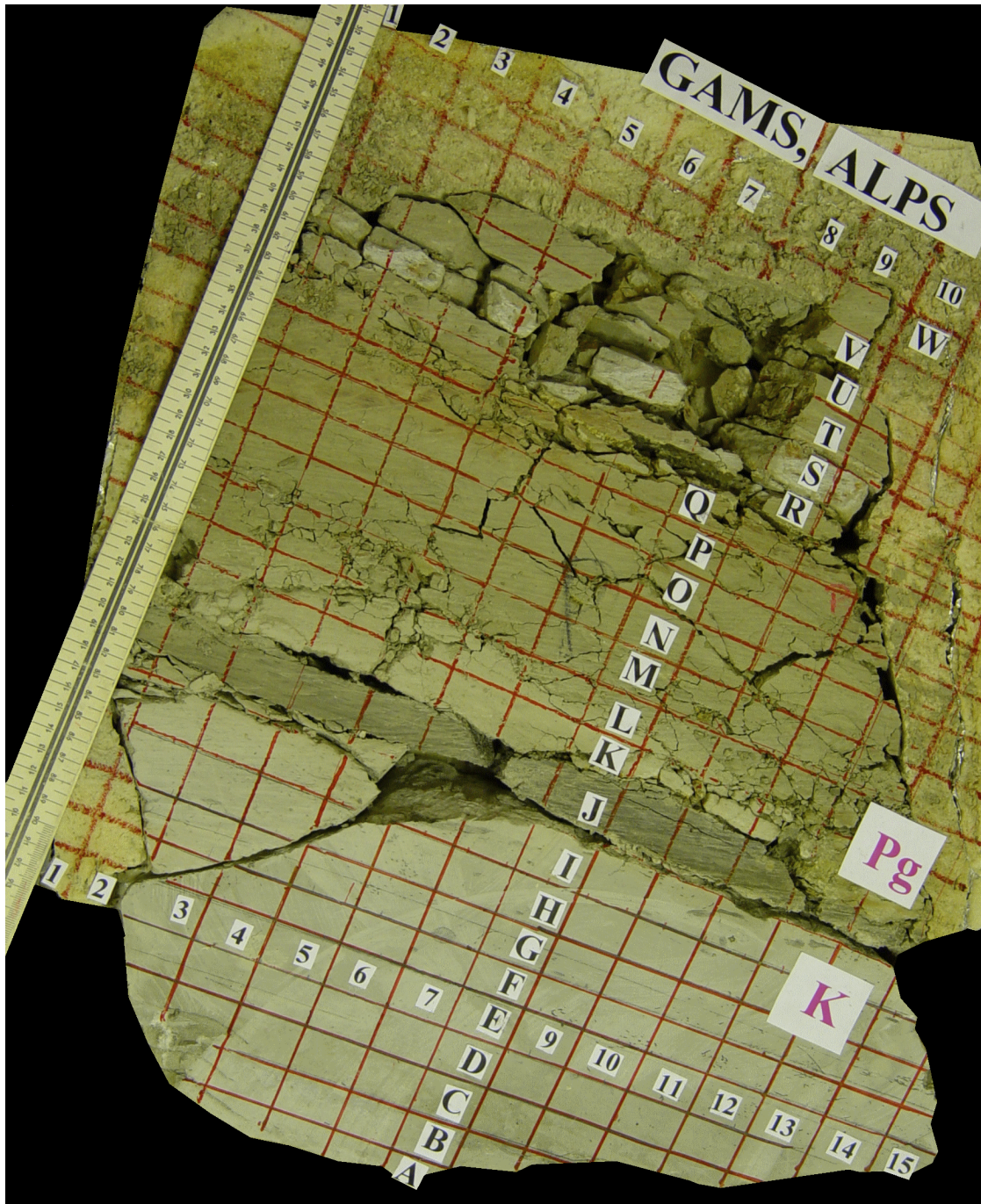
Figure 3. The Gams section monolith, prepared for sampling (photograph).

stone, and bears a wealth of typically Cretaceous planktonic foraminifers. The layer lies in the upper part of Nierental Formation of the Gosau Group [*Kollmann,* 1964], which consists of a thick unit of predominantly clayey limestone, marl, and siltstone. The layer separates the lower (predominantly calc–marly) and upper (predominantly silty–clayey) parts of the Gosau Formation or occurs near the roof of the lower portion of the Gosau Formation (Lower Gosau) [*Peryt et al.,* 1993; *Preisinger et al.,* 1986].

Methods of Material Preparation and Studying

[21] In order to examine the Gams sequence, the monolith was divided into 23 units (from *A* through *W*) 2 cm thick each (Figure 3), and transitional layer *J* at the K/T boundary was further split into six units (Figure 4). The methods applied to examine the material involved: the ex-
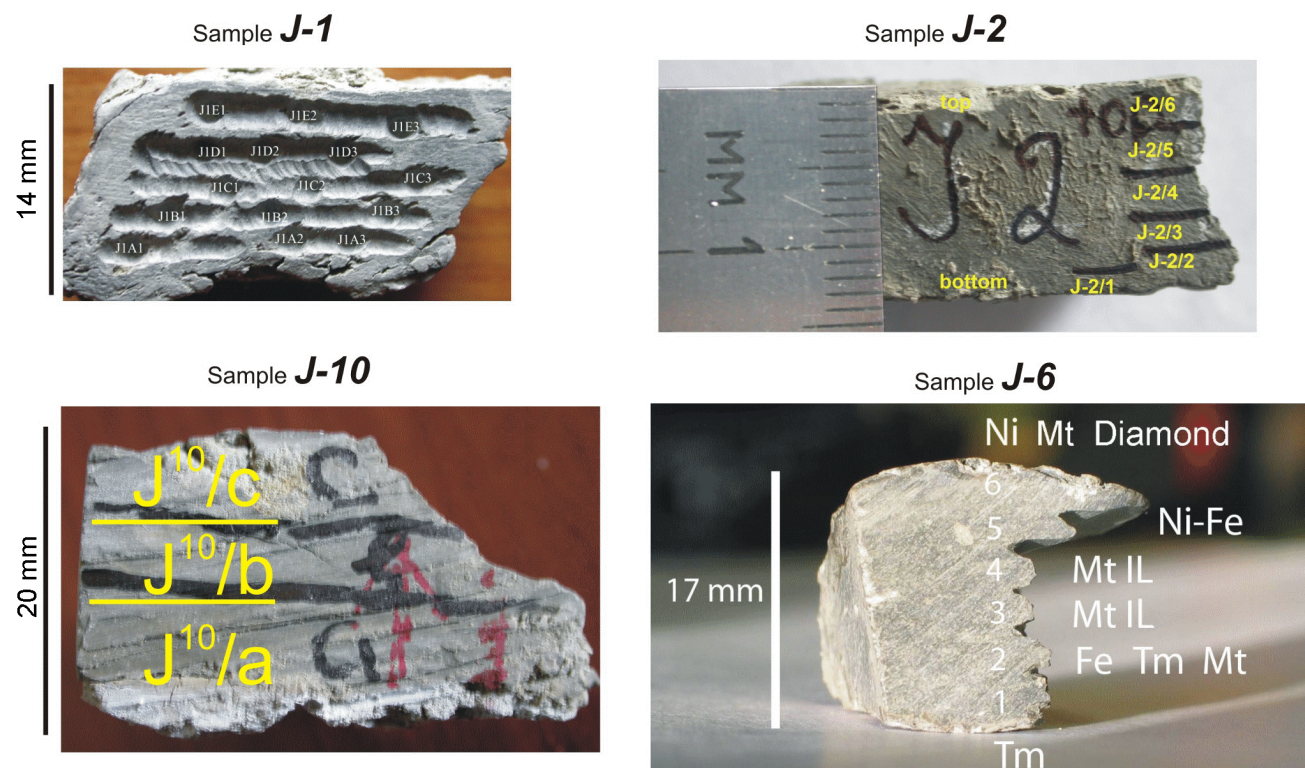
Figure 4. The subdivision of the transition layer J on the separate units for different kinds of analysis.

amination of thin sections and monomineralic fractions, conventional chemical analysis, XRF, neutron activation analysis, X-ray diffraction (XRD), analysis of the material for the isotopic composition of helium, oxygen, and carbon, microprobe analysis of minerals (MPA), and petromagnetic analysis.

[22] In order to obtain heavy-fraction minerals, a sample 10–15 g was crushed in a porcelain mortar and screened through a 0.25-mm sieve. Heavy-fraction minerals were separated from the carbonate–clayey mass using a heavy liquid (bromoform $CHBr_3$, density 2.89 g cm^{-3}). The heavy and light fractions were washed with alcohol and purified of magnetic minerals (magnetite) by a magnet. Heavy-fraction minerals were then separated according to their electric conductivity (on a magnetic separator) into non-electromagnetic, weakly electromagnetic, and electromagnetic fractions. Zircon and other minerals were hand-picked under a binocular magnifier, using a needle, and were glued to glass platelets with pits. The light fraction was used to obtain quartz (on a magnetic separator).

[23] Major components (SiO_2, TiO_2, Al_2O_3, total FeO, MgO, MnO, CaO, Na_2O, K_2O, P_2O_5, and total S) were determined by XRF.

[24] **Analysis for trace elements and REE.** The sample selected for analysis was decomposed in acids in a MULTIWAVE microwave furnace. 50- to 100-mg batches of the material were decomposed in a Teflon capsule in a mixture of hydrofluoric and nitric acids at a temperature of 240°C and a pressure of no more than 72 bar for

50 min. Fluorides of metals were decomposed by dissolving dry residues in 5–7 ml of 6.2 N HCl at 90°C for 1 h. After this the sample was spiked with an internal standard (In) and mixed with 3 ml of 3 N HNO_3. The chlorides were completely transformed into nitrates for 15–20 min at a temperature of about 200°C. The final concentration of HNO_3 was 0.5 N, and the dilution coefficient of the sample was close to 1000. This method ensured the complete decomposition of most minerals contained in the sedimentary rocks, including zircon and monazite (some spinels, such as chromite, were decomposed not fully). All of the acids utilized in this procedure were twice distilled in a quartz (or Teflon for HF) apparatus from starting analytical-grade reactants.

[25] Mass spectrometry was conducted on an Elan 6100 DRC analytical system (Elan 6100 DRC, Software Kit, May 2000, Perkin Elmer SCIEX Instrument) in a standard mode, under the following operation conditions: nebulizer argon flow of 0.91–0.93 l min^{-1}, auxiliary argon flow of 1.17 l min^{-1}, plasma-forming argon flow of 15 l min^{-1}, the plasma generator operating at 1270–1300 W, and a voltage of 1000 V at the detector in the counting mode. The sensitivity of the analytical system was calibrated throughout the whole mass scale against standard solutions that included all elements to be analyzed in the samples. The accuracy of the analyses was monitored and the sensitivity drift was taken into account by alternating the analyses of unknown samples and the monitor, which was standard basalt sample BCR-2 (United States Geological Survey). The detection limits (DL) were from 1–5 ppb for elements with heavy and medium masses (such as U, Th, and REE) to 20–50 ppb for light elements (such as

Be and Sc). The analyses were conducted accurate to 3–10% for elemental concentrations >20–50 DL.

[26] In a small number of samples, REE were determined by ICP-MS on a PLASMA QUARD PQ2+TURBO (VG Instruments) quadrupole mass spectrometer, following the procedure described in [*Dubinin,* 1993].

[27] **Analysis of clays.** The mineralogical analysis of the pelitic fraction <4 μm was conducted on an D/MAX-2200 (Rigaku, Japan) X-ray diffractometer with Cu monochromatic radiation. The operating conditions were: 40 mA, 40 kV, 0.5° scattering slit, 0.5° and 3 mm receiving slits, 0.02° step, and 2 s collection time at a spot.

[28] The phase analysis of clay minerals was accomplished on oriented samples in air-dry and saturated with ethylene-glycol states. Minerals were identified by series of integer reflections *OOl*. The raw specters were processed with the Jade-6.0 (MDI, United States) computer program. The quantitative proportions of clay minerals were derived from the basal reflections in the saturated state, following the method described in [*Biskaye,* 1965]. The sum of clay minerals was normalized to 100%.

[29] **Microprobe analysis.** In order to analyze the composition and microstructure of ferromagnetic minerals in the rocks, their samples were examined on a Camebax microprobe. Samples were mounted on a pellet 26 mm in diameter and fixed with Wood's alloy. After this, they were carefully polished and finished using diamond pasts, and were spray sputtered with carbon. The analyses were conducted at an accelerating voltage of 20 kV and a beam current of 10 nA. The effective beam diameter was 2–3 μm and was systematically monitored using small grains. Ore minerals were analyzed for TiO_2, FeO, MgO, MnO, Cr_2O_3, and Al_2O_3.

[30] **Micropaleontoligical analysis.** Foraminifers from the rocks were examined following the conventional techniques of their separation and preparation. Material for the analysis was taken from units *C, D, E, G, H, I, J, K, L, M, N, Q, R, S, T,* and *U*. The 50- to 70-g samples were crushed under a screw-down press into small fragments, which were then put into distilled water with dissolved caustic soda (depending on the rock hardness) and boiled for 30 min to 10 h. After this, the material was washed on various sieves. To identify buoyant hollow shells of planktonic foraminifers before washing on sieves under a water flow, the aqueous solution remaining after boiling was racked, and the solid material was dried. This material was washed on sieves with mesh of 1 mm, 250 μm, and 160 μm, and all the fine grained residue that remained at the sieves was elutriated in a pan. The residues at each of the sieves and pan were dried and weighted. Foraminifers were gathered into Franke cells and examined under an MBS-1 binocular magnified at magnifications of 28$^\times$, 56$^\times$, and 98$^\times$. Structural details of the shell surfaces and ultrastructure of their walls were conducted on a CamScan MV2300 scanning electron microscope, which was also used to obtain images of the shells. The material was preliminarily sputtered with gold at a HV cathode voltage of 5.0 kV. Admixtures on the walls of the shells were analyzed on an INCA Oxford Instruments microprobe.

[31] **Petromagnetic study.** In order to conduct standard pertomagnetic measurements, each of the samples was cut into a series of cubes with edges ranging from 1 cm to 2 cm. Thermomagnetic analysis was carried out in fragments less than 1 cm across.

[32] The petromagnetic measurements involved the determination of the specific magnetic susceptibility χ, hysteresis characteristics (saturation field H_s, saturation magnetization M_s, specific remanent saturation magnetization M_{rs}, coercivity H_c, and remanent coercivity H_{cr}), anisotropy A_k and A_{rs}, and coercivity spectra. The magnetic susceptibility and remanent magnetization were measured on susceptibility bridge KLY-2 and spin-magnetometer JR-4, respectively; and the hysteresis characteristics of the samples were examined on a coercivity spectrometer [*Burov et al.,* 1986; *Yasonov et al.,* 1998], which made it possible to obtain normal magnetization line up to 0.5 T in automated mode. The thermomagnetic measurements were carried out with a Curie balance. The concentrations of magnetite, iron, hemoilmenite, nickel, and "goethite" in the sample were estimated from the results of thermomagnetic analysis $M(T)$ as follows. The contributions of each phase to the magnetization was evaluated using the $M(T)$ curve, and this value was divided into the specific saturation magnetization of this mineral. The following values of the M_s of minerals were assumed: $\sim$90 Am^2 kg^{-1} for magnetite, $\sim$200 for iron, $\sim$0.2 for goethite, and from $\sim$4 to $\sim$40 Am^2 kg^{-1} for hemoilmenite at T_c from 300°C to 200°C [*Nagata,* 1965]. The value of $M_s = 0.02$ Am^2 kg^{-1} assumed here for goethite is the minimal one, and this leads us to the lower limit for the concentration of iron hydroxides (which include paramagnetic species). Moreover, the saturation field of fully crystalline goethite is much higher than the magnetic field in which the thermomagnetic analysis was conducted.

[33] The values of χ, M_s, and H_c are notably contributed by paramagnetic (clays) and diamagnetic (marly limestone) material. This contribution is eliminated from the values of M_s and H_c using the normal magnetization curves.

[34] **Carbon and oxygen isotopic analysis.** Samples were cut, grounded, and cleaned; and their sections were examined under an optical microscope. The rocks were powdered with a Dremel MiniMite microdrill tool. The amount of the powder prepared for a single analysis was 300 μg or more, depending on expected content of carbonates. Each sample was analyzed at several spots. The spots of duplicate analyses were spaced $\sim$1 cm apart. Carbon isotopes in calcite from the samples were analyzed a Finnigan MAT 253 mass spectrometer with a Gasbench II at the Department of Earth and Space Sciences, University of California, Los Angeles. The carbon isotopic composition is defined as a deviation, in $^o/_{oo}$, of the $^{13}C/^{12}C$ and $^{18}O/^{16}O$ ratios of a given sample from those of a standard, expressed in the conventional ^{13}C and ^{18}O notations relative to V-PDB and SMOW. The secondary standards were NBS-19 and IAEA-CO-1. The accuracy of the analyses was better than ±0.1 $^o/_{oo}$ for carbon and ±0.2 $^o/_{oo}$ for oxygen.

[35] **Helium isotopic composition.** Both the isotopic composition and concentration of He were measured on a MI-1201 no. 22-78 mass spectrometer at the Laboratory of
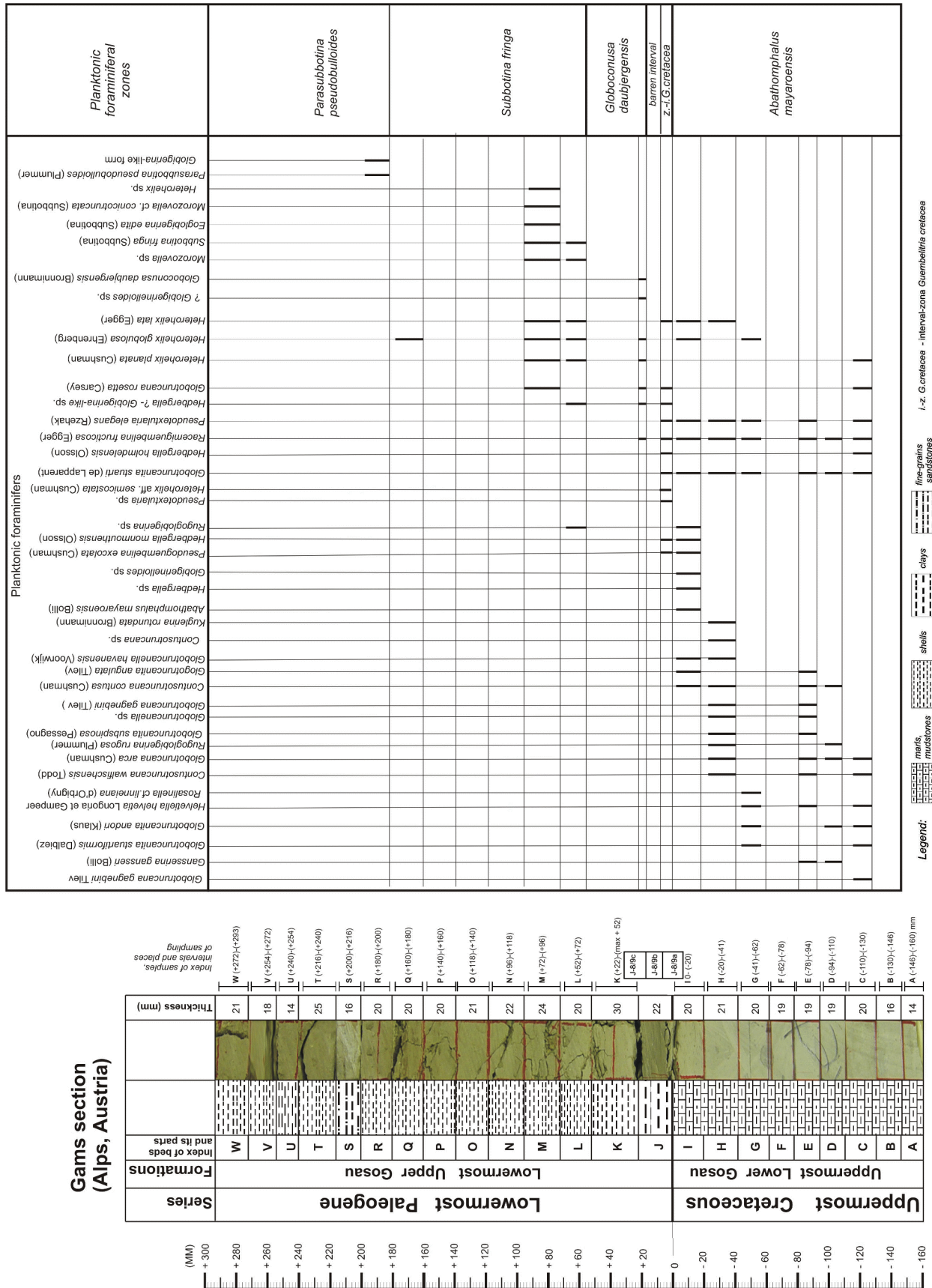
Figure 5. Distribution of the planktonic foraminifers in the Gams section.

Isotopic Analysis of the Geological Institute, Kola Research Center, Russian Academy of Science, in Apatity the sensitivity of 5×10^{-5} A Torr^{-1} for ^{3}He. The concentrations were deduced from the height of the peaks accurate to 5% ($\pm 1\sigma$), the errors of the isotopic ratios were $\pm 20\%$ at ^{3}He/^{4}He $= n \times 10^{-8}$ and $\pm 2\%$ at ^{3}He/^{4}He $= n \times 10^{-6}$. The blank experiments were conducted after the reloading of the holder, under the same conditions as those for the analysis of the samples. The analyses were conducted on a MI-1201 no. 22-78 mass spectrometer using the method of melting, as described in [*Kamensky et al.,* 1990].

Biostratigraphy and Foraminiferal Assemblages

[36] The studied interval of the section (units A–W) yields both planktonic and benthic foraminifers. Planktonic foraminifers are common in the lower calcareous marlstone part of the section (units A–I). The units contain numerous and diverse planktonic foraminifers though their tests are poorly preserved owing to properties of enclosing sediments and to imperfect techniques used for their extraction from these rocks. A poor preservation of many tests is manifested by the fact that certain elements of test morphology, for instance apertures, are covered with rock particles, which are unsusceptible to removal after washing. This fact makes a lot of planktonic foraminiferal shells badly illustrated on photos and hinders their study under electron microscope.

In the upper, clayey part of the section (units J–W) planktonic foraminifers occur only in certain intervals. Most of tests in the assemblages are well preserved; intact tests are encountered together with that partially or completely squeezed and those possessing a smoothed-out exterior sculpture. However, specific assignments were defined for most of specimens permitting the exact age estimate of enclosing sediments.

[37] Benthic foraminifers are diverse and numerous in both lower, calcareous marlstone, part of the section (units A–I) and upper, mainly clayey portion (units J–W). In the lower part they were identified in all studied units C, D, E, G, H, I. Species of *Gaudryina, Marssonella, Rzehakina, Gyroidinoides, Lenticulina, Arenobulimina, Trochammina, Eggrellina, Stensioeina,* and *Globorotalites* are the most common in the benthic assemblages. The benthic foraminifers are well preserved, commonly better than planktonic forms. In the upper, clayey part of the section benthic foraminifers are more numerous than planktonic taxa, however, they are also found only in certain layers. In layer J benthic foraminifers occur in samples J-8/9a and J-8/9c and are missing in sample J-8/9b. Upward from the base they were encountered in units $L, M, N, O, Q, R, T,$ and U.

[38] Planktonic and benthic foraminifers were not encountered in the middle portion of layer J (sample J-8/9b) and are missing in layers K and S. Their absence in the latter units results from unfavorable for test preservation composition of enclosing sediments: such rocks are usually barren of foraminifers. However, the lack of foraminifers in middle part of layer J (sample J-8/9b) can hardly be explained by this reason.

[39] In view of the decisive significance of planktonic foraminifers for studies of stratigraphic position of the Cretaceous–Paleogene boundary and reconstruction of concurrent environmental changes, in this paper the priority is given just to that group (Figures 5–12). The benthic foraminifer distribution will be analyzed later. Below is the description of zonal subdivision of the transitional units and substantiation of age of enclosing sediments using planktonic foraminifers (Figure 5).

Uppermost Upper Maastrichtian

[40] The *Abathomphalus mayaroensis* Zone (upper part) (upper boundary defined by the last occurrence of index species). The sediments are represented by light grey clayey limestones and marls of units $A - I$. The foraminiferal assemblage includes typical Cretaceous single- and two-keeled taxa of *Globotruncanidae*, scarce non-keeled *Hedbergellidae*, and numerous *Heterohelicidae*. Among the encountered characteristic species there are *Contusotruncana walfischensis* (Gandolfi), *Globotrincanita stuartiformis* (Dalbiez), *Globotruncana arca* (Cushman), *Globotruncana rosetta* (Carsey), *Globotruncanita andori* (Klaus), *Globotruncana gagnebini* Tilev, *Gansserina gansseri* (Bolii), *Contusotruncana contusa* (Cushman), *Globotruncanita stuarti* (de Lapparent), *Globotruncana arca* (Cushman), and *Rugoglobigerina rugosa* (Bronnimann). Additionally the studied assemblages contain rather peculiar species of the family Heterohelicidae: *Pseudotextularia elegans* (Rzehak) and *Racemiguembelina fructicosa* (Egger).

[41] The studied foraminifer assemblage clearly indicates the correspondence of enclosing sediments to the *Abathomphalus mayaroensis* or *Pseudoguembelina hariaensis* zones of standard zonations based on Globotruncanidae and *Heterehelicidae*, respectively [*Hardenbol et al.,* 1998].

[42] The disappearance of a great majority of typical Cretaceous planktonic foraminifers and especially of *Abathomphalus maryaensis* and *Globotruncanita stuarti*, evidences that the upper boundary of this zone corresponds to the top of the similar zone, and evidently to Bed 9, in the Rotwandgraben section in the Eastern Alps [*Peryt et al.,* 1993], to the top of the like zone in the Bavarian Alps [*Herm et al.,* 1981] and Tunisia [*Keller,* 1988], and probably exactly coincide or is close to the top of the *Abathomphalus maryaensis* Zone of the standard zonation [*Hardenbol et al.,* 1998].

Lowermost Paleogene

[43] The *Guembelitria cretacea* Zone-Interval (base defined by last occurrence of *Abathomphalus maryaensis*; upper boundary, by first occurrence of Globoconusa daubjergensis). Dark green, almost black, noncarbonate, 0.5-cm-thick clays of the lower and middle parts of layer J are referred to the zone. Planktonic foraminifers occur only in the lower part (sample J-8/9a). The middle portion of the bed (sample J-8/9b) is barren of

System	Stages	This paper	Peryt et al., 1993	Herm et al., 1981	Brinkhius, Zachariasse, 1988	Keller, 1988	Bolli, 1966	Berggren, Miller, 1988	Blow, 1979	Berggren et al., 1995 (Paleog.), and Robaszynski (Cret.) in Hardenbol et al., 1998
Paleogene	Danian	*Parasubbotina pseudobulloides*	*Subbotina pseudobulloides* (P0a, P1)	*Globorotalia pseudobulloides*	*Neogloboquadrina pseudobulloides*	*Globorotalia pseudobulloides* (P1c)	*Globorotalia pseudobulloides*	*Subbotina triloculina* (P1b); *Subbotina pseudobulloides* (P1a)	*Globorotalia (Turborotalia) pseudobulloides* / *Globorotalia (Turborotalia) archaeocompressa* (P1a)	*M. pseudobulloides* (P1b)
			Parvularugoglobigerina eugubina (Pα)	*Globigerina eugubina*	*Parvularugoglobigerina eugubina*	*Globigerina taurica*, *Eoglobigerina* spp., *Globigerina eugubina* (P1b, P1a)	*Globigerina eugubina*	*Parvularugoglobigerina eugubina* (Pα)	*Globorotalia (Turborotalia) longiapertura* (Pα)	*G. eugubina* (P1a)
		Subbotina fringa	*Globoconusa conusa* (P0b)	*Globigerina fringa*	*Parvularugoglobigerina fringa*	*Globoconusa conusa* (P0b)			*Rugoglobigerina hexacamerata* (M18)	P1α
		Globoconusa daubjergensis	*Guembelitria cretacea* (P0a, P0)		*Guembelitria cretacea*	*Guembelitria cretacea* (P0a)				
		barren interval				*Pseudotextularia deformis* / *Abathomphalus mayaroensis* (P0)				*Pseudoguembelina hariaensis* / *Abathomphalus mayaroensis*
		z.-i. G.cretacea								
Cretaceous	Maastrichtian	*Abathomphalus mayaroensis*	*Abathomphalus mayaroensis*	*Abathomphalus mayaroensis*	*Abathomphalus mayaroensis*	*Abathomphalus mayaroensis*	*Abathomphalus mayaroensis*	*Abathomphalus mayaroensis* (M17)	*Abathomphalus mayaroensis* (M17)	*Racemiguembelina fructicosa*

Figure 6. Correlation chart of the Cretaceous/Paleogene boundary divisions.
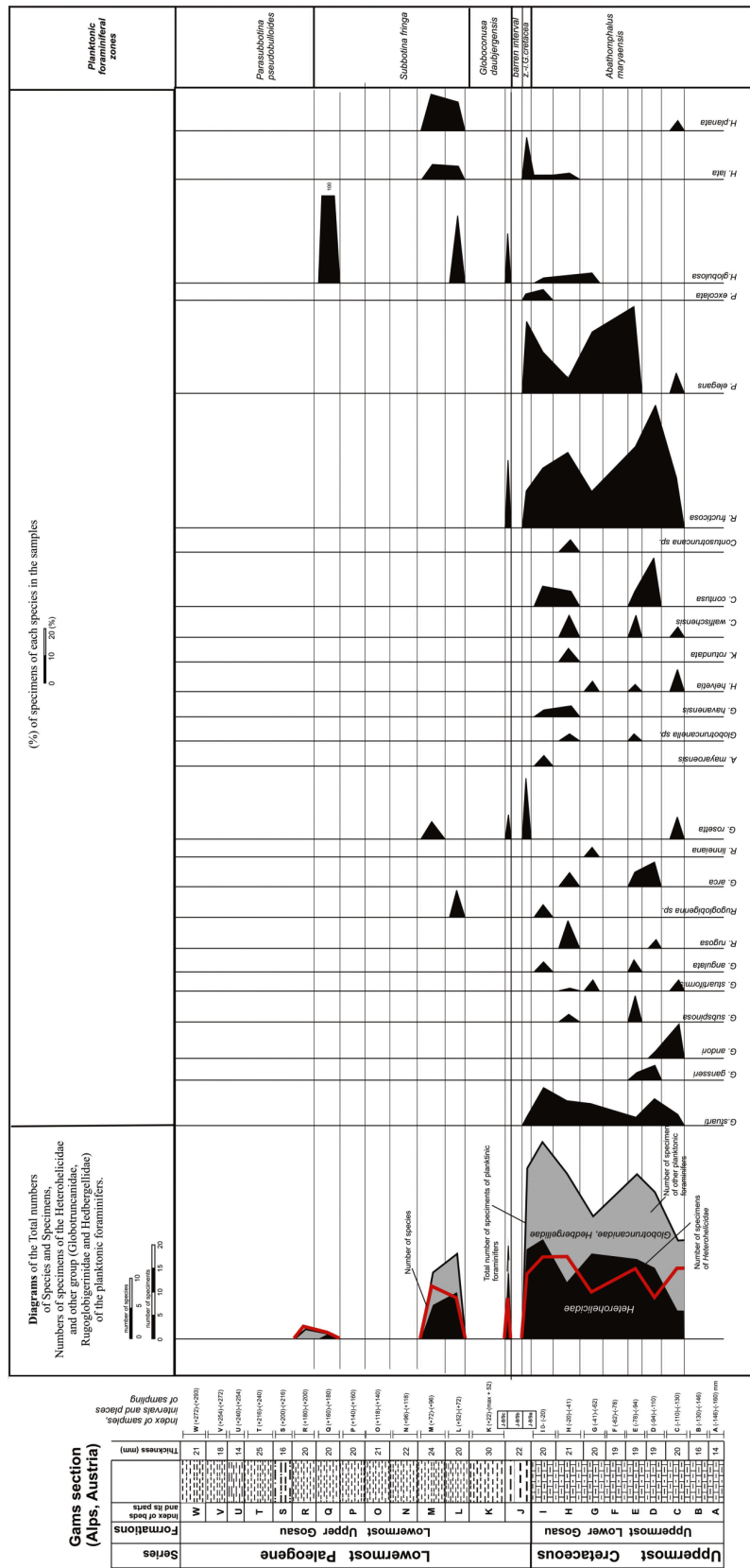
Figure 7. Diagram of quantities of specimens and relative percent abundances of planktonic foraminiferal species in the Gams section.
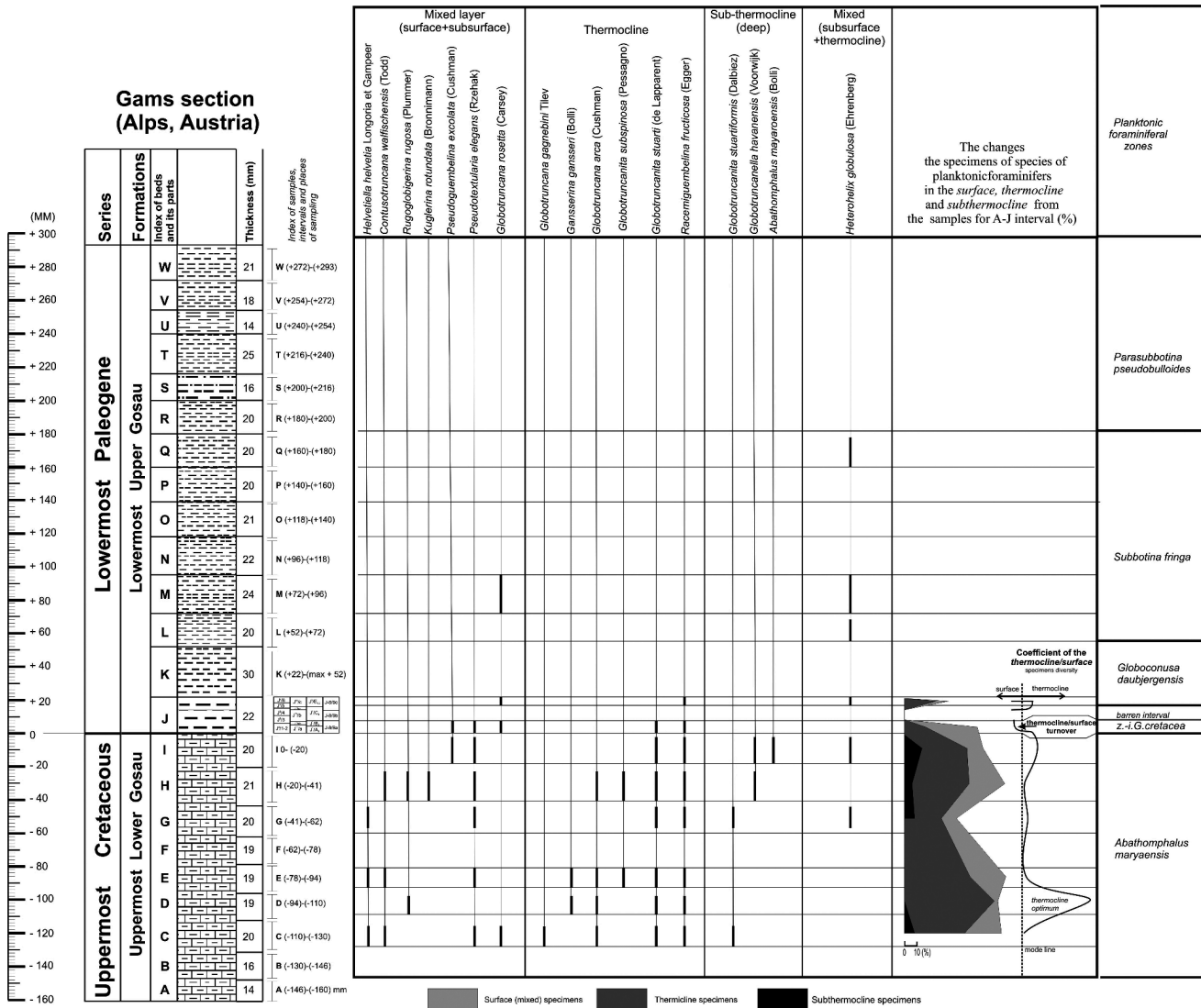
Figure 8. Distribution of surface, thermocline and subthermocline planktonic foraminifers species in the Gams section.

forams. Sediments in the lower part of layer J (sample J-8/9a) yield few specimens of *Globotruncanita stuarti* (de Lapparent), *Globotruncanita* sp., and several deformed tests of *Globotruncana rosetta* (Carsey) from the family Globotruncanidae. The interval also contains numerous *Pseudoguembelina excolata* (Cushman), *Pseudotextularia elegans* (Rzehak), *Racemiguembelina fructicosa* (Egger), *Heterohelix lata* (Egger), *Heterohelix globulosa* (Ehrenberg), and *Heterohelix* aff. *semicostata* (Cushman) of the family Heterohelicidae. Poorly preserved *Hedbergella monmouthensis* (Olsson) and *Hedbergella holmdelensis* (Olsson) were identified as well.

[44] *Barren interval* is represented by dark green to black, 0.2-cm-thick clays in the middle part of layer J (Sample J-8/9b) lacking foraminifers. It is still early to judge how geographically wide this interval with missing foraminifers, conventionally named Barren interval, is distributed. Through

distinguishing this part of the section as a separate stratigraphic unit we try to call attention to a possible occurrence of the similar bed in other sections.

[45] The *Globoconusa daubjergensis* Zone (base boundary defined by first occurrence of index species). Dark green to black, noncarbonate, 0.5-cm-thick clays of the upper part of layer J (sample J-8/9c) are referred to the zone. They are characterized by the first occurrence of single specimens of typical Paleogene species *Globoconusa daubjergensis* (Bronnimann) and Paleogene-like forms close to (?) *Hedbergella-Eoglobigerina trivialis* (Subbotina). The sediments also yield single deformed shells of *Globotruncanita rosetta* (Carsey), a typical Cretaceous member of Globotruncanidae, and the Cretaceous Heterohelicidae members *Heterohelix lata* (Egger), *Heterohelix globulosa* (Ehrenberg), and *Racemiguembelina fructicosa* (Egger). It is remarkable

that tests of the latter are rather numerous but have a slightly ornamented surface and look somewhat smoothed, i.e. can be redeposited.

[46] In the well-studied sections the earliest findings of *Globoconusa daubjergensis* are known from the zone P0 (0.8 m above GSSP) in the Elles II section in Tunisia [*Keller et al.,* 2002b] and slightly higher, from the zone P1a in Guatemala [*Keller and Stinnesbeck,* 2000], Egypt [*Keller,* 2002], Coxquinhui, Mexico [*Stinnesbeck et al.,* 2002, the Koshak section, Kazakhstan [*Padro et al.,* 1999] and from the zone P1c (Bed 23b) in the Stevns Klint section, Denmark (Figure 6). According to the latest records, this species most likely first occurred still earlier and can be considered as one of the earliest Paleogene planktonic foraminifers [*Patterson et al.,* 2004]. It is quite probable that findings of *Globoconusa daubjergensis* in the Gams section illustrate that very case.

[47] The *Subbotina fringa* Zone (base defined by first occurrence of index species). The sediments of the zone are represented by greenish-grey, slightly carbonate and carbonate, 14.0-cm-thick clays and siltstones. Planktonic foraminifers occur only in units *L, M* and *Q*. The foraminiferal assemblage of that part of the section includes in unit *L* (Sample *L*-6) a typical Paleogene species *Subbotina fringa* (Subbotina) and the Paleogene-like forms close to (?) *Morozovella* sp. cf. *M. conicotruncata* (Subbotina) and (?) *Morozovella* sp. though unsusceptible to exact identification owing to small amount of tests and their moderately poor preservation. The typical Paleogene species (?) *Hedbergella-Eoglobigerina trivialis* sp. also occur there, together with peculiar Upper Cretaceous forms *Heterohelix lata* (Egger), *Heterohelix planata* (Cushman), *Heterohelix globulosa* (Ehrenberg), *Heterohelix lata* (Egger), *Heterohelix* sp., and few *Rugoglobigerina* sp. and *Globotruncana rosetta* (Carsey).

[48] Thus there are grounds to believe that the units *L* and *M*, according to foraminiferal assemblage and first occurrence of Subbotina fringa, most likely correspond to units 17 and 18 in the Rotwandgraben section (Eastern Alps) and should be correlated with the recognized there *Globoconusa conusa* Zone [*Peryt et al.,* 1993]. Units *L* and *M* can also completely or partially correspond to the *Subbotina fringa* Zone distinguished in the Bavarian Alps [*Graup and Spettel,* 1989; *Herm et al.,* 1981] and in Tunisia [*Brinkhuis and Zachariasse,* 1988].

[49] The *Parasubbotina pseudobulloides* Zone (base defined by first occurrence of index species). This zone includes light, greenish-grey siltstones of unit *R* and likely a part of overlying sediments: fine-grained sandstone layers (unit *S*) and greenish-grey siltstones of units *T–W*. Planktonic foraminifers were encountered in unit *R* (sample *R*-6), which is characterized by the first occurrence of typical Paleogene *Parasubbotina pseudobulloides* (Plummer) and few specimens of "Paleogene taxa" defined as *Globigerina*-like *forms* that cannot be exactly identified owing to poor preservation.

[50] We consider that unit *R* corresponds to the recognized there *Parasubbotina pseudobulloides* Zone and to Bed 22 of the Rotwandgraben section in the Eastern Alps [*Peryt et al.,* 1993], i.e. it can be believed that the base of unit *R* corresponds to the base of the like zone in schemes by *Bolli* [1966] and *Herm et al.* [1981].

Paleoecologic Features of Planktonic Foraminiferal Assemblages

[51] The diversity of planktonic foraminiferal species is comparably high in the lower part of the section (Units *A–I*, the *Abathomphalus maryaensis* Zone) ranging from 6–7 to 14–15 species in the assemblage (Figure 7). A similar diversity (11–12 species) is recorded in the lower portion of layer *J* (Sample *J*-8/9a). In the middle part of layer *J* planktonic foraminifers are missing; though in its upper part the species diversity is somewhat lower than in units *A–I* and lower part of layer *J*, it still reaches 6–7 species. The total number of planktonic foraminifer specimens in units *A − I* is high; the maximum amount was recorded in units *D* and *I*, the minimum one is in unit *G*. In the lower part of layer *J* (sample *J*-8/9a) the abundance of planktonic foraminifers is as high as in the underlying units. In its upper portion their amount almost twice decreases compared to that of the Maastrichtian (units *A–I*) and Early Paleocene (lower part of layer *J*) assemblages and slightly exceeds the abundance of the above-lying associations. It is remarkable that in the Maastrichtian assemblage (units *A–I*) and lower part of layer *J* (sample *J*-8/9a) the members of two families, Globotruncanidae and Heterohelicidae, dominate. Other families – Rugoglobigerinidae and Hedbergellidae – are represented by few species with a low number of specimens. It is notable that Globotruncanidae are characterized by numerous species with comparatively small amount of specimens in the assemblage, whereas Heterohelicidae is represented by two, rarely five species, among which *Racemiguembelina fructicosa* and *Pseudotextularia elegans* are extremely abundant.

[52] Therefore, two species of the family Heterohelicidae constitute almost a half of planktonic foraminiferal assemblage. *Racemiguembelina fructicosa* and *Pseudotextularia elegans* occurred there in competitive relations, i.e. the increased number of specimens of one species was accompanied by a reduction of the other. For instance, units *D* and *H* are dominated by *Racemiguembelina fructicosa*, whereas units *E* and *I*, by *Pseudotextularia elegans*. In the lower part of layer *J* (sample *J*-8/9a) the assemblage is also dominated by Heterohelicidae, its five species constitute 53% of the total composition but the dominating form is *Heterohelix lata* and not *Racemiguembelina fructicosa* and *Pseudotextularia elegans*, as in units *A–I*. In that portion of layer *J* the Globotruncanidae members make up only about 33% of the assemblage and the share of Hedbergellidae species, namely, of *Hedbergella-forms*, significantly increase compared to the assemblages of units *A–I*.

[53] As indicated above, the upper part of layer *J* is marked by though lesser species diversity than its lower portion (sample *J*-8/9a) and units *A–I*, but still comparatively high (7 species); however, the most abundant species are *Heterohelix lata* and *Heterohelix globulosa* together with *Racemiguembelina fructicosa*. The Cretaceous *Globotruncana* and *Hedbergella* members and Paleogene *Globoconusa daubjergensis* occur in single specimens.

[54] In the upper part of the discussed section planktonic foraminifers are scarce. However, the assemblage from units
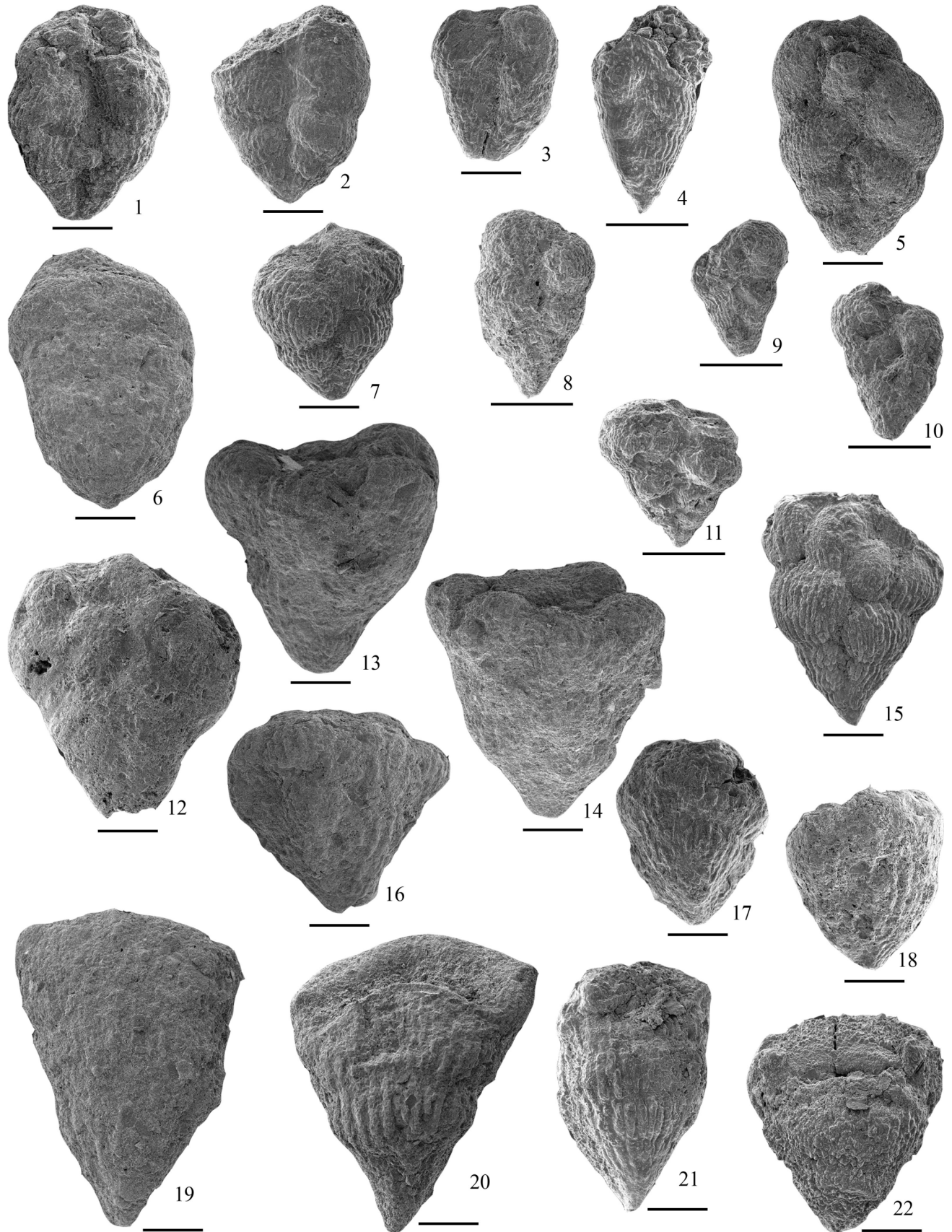
Figure 9. Planktonic foraminifers Heterohelicidae, Scale bar = 100 μm.
1, 5 – *Pseudoguembelina excolata* (Cushman), lateral side, 1 – sample J-8/9a, 5 – sample I-6;
2, 3, 7 – *Heterohelix lata* (Egger), view from lateral side: 2 – sample J-8/9a; 3 – sample J-8/9c, 7 – sample J-8/9a;
4 – *Heterohelix* aff. *semicostata* (Cushman), lateral side, sample J-8/9a;
6 – *Pseudotextularia elegans* (Rzehak), lateral side, sample G-2;
$\Leftarrow$ 7 – *Heterohelix lata* (Egger), lateral side, sample J-8/9a;
8–10 – *Heterohelix planata* (Cushman), lateral side, 8 – sample M-4, 9 – sample M-4, 10 – sample M-4;
11 – *Heterohelix globulosa* (Ehrenberg), lateral side, sample M-4;
12–16 – *Racemiguembelina fructicosa* (Egger), lateral side, 12 – sample J-8/9c, 13 – sample D-4, 14 – sample E-3, 15 – sample J-8/9a, 16 – sample B-4;
17–22 – *Pseudotextularia elegans* (Rzehak), lateral side, 17 – sample J-8/9c, 18 – sample J-8/9a, 19 – sample E-3, 20 – sample I-6, 21 – sample J-8/9a, 22 – sample J-8/9a.

L–M also consists of 8–9 species, whereas units *O* and *R* are characterized by single specimens of one or two species. This interval is also dominated by Heterohelicidae species *Heterohelix globulosa, Heterohelix lata, Heterohelix planata,* and *Heterohelix* sp.

[55] The studied assemblages of planktonic foraminifers contain a number of species, for which inhabiting conditions can be defined according to currently available notion [*Abramovich et al.,* 2003]. For instance, *Helvetiella helvetia, Contusotruncana walfischensis, Rugoglobigerina rugosa, Kuglerina rotundata, Pseudoguembelina excolata, Pseudotextularia elegans,* and *Globotruncana rosetta* most likely inhabited the surface+subsurface waters; *Globotruncana gagnebini, Gansserina gansseri, Globotruncana arca, Globotruncanita subspinosa, Globotruncanita stuarti,* and *Racemiguembelina fructicosa* occurred nearby the thermocline; *Globotruncanita stuartiformis, Globotruncanella havanensis,* and *Abathomphalus mayaroensis* preferred the sub-thermocline waters and are considered to be deep-water species; finally *Heterohelix globulosa* inhabited both subsurface and thermocline waters [*Abramovich et al.,* 2003]. The distribution of these species in the section is illustrated in Figure 8.

[56] From the distribution, abundance, and disappearance of the listed ecological (bathymetric) groups of planktonic foraminifers we can infer how favorable, and likely stratified, were different layers of the water column in the Gams paleobasin during the transitional Cretaceous–Paleogene time.

[57] Throughout the Cretaceous–Paleogene transition (interval of units (*A*)–(*J*-8/9a) and (*J*-8/9c)) favorable conditions constantly occurred in subsurface and thermocline waters. During the accumulation of units *C, G, H,* and *I* deep, subthermocline waters were also suitable. The thermocline fauna during the formation of units *A–I* and *J*-8/9c excelled the inhabitants of subsurface waters in both number of species and abundance.

[58] The number of planktonic foraminifer specimens from thermocline waters is commonly twice as large as that from subsurface layers. Only during the accumulation of unit *D* the thermocline inhabitants became extremely numerous and constituted 74% against 3% of subsurface dwellers. This could result from a temporary deterioration in subsurface water environments.

[59] However, it is remarkable that in the period of unit *J*-8/9a deposition the relationship of the assemblage dominants became inversed. Surface water inhabitants excelled the thermocline dwellers in both number of species (3 against 2) and abundance (42% against 7%). It is likely that in this period the inhabiting conditions could improve, or remain favorable in subsurface layer and deteriorate in the thermocline.

[60] During the accumulation of unit *J*-8/9c the conditions in subsurface and thermocline waters again became similar to those existed during the deposition of units *A–I*. The thermocline fauna is more abundant there than the subsurface association.

[61] Thus we can suppose that during the initial accumulation of layer *J* the thermocline and sub-thermocline environmental conditions were sharply deteriorated.

[62] During the deposition of unit *J*-8/9b the conditions most likely became still worse and to the thermocline interval the subsurface, sub-thermocline, and bottom waters became barren. The whole water sequence was unsuitable for the existence of planktonic and benthic foraminifers. At the stage of the layer *J*-8/9c accumulation the environmental conditions in subsurface and thermocline waters regained their original properties similar to that in units *A–I*. Only sub-thermocline waters remained unfavorable. The low abundance and diversity of planktonic foraminifers indicate that environmental conditions in the thermocline and surface waters though somewhat improved but were not completely suitable for foraminifers and did not manage to become inhabited after the crisis.

Composition of Rocks in the Gams Stratigraphic Sequence

[63] As can be seen at the photograph of Figure 2, which was taken before the complete drying of the monolith, the sequence consists of units of definitely distinct color: a lower carbonate part of pale gray color (units (*A–C*); transitional layer *J,* which consists of black clays; and a lens (which rests on the eroded top of layer *J*) of sandy clay gray rock (layer *K*) (Figure 13), in which slickensides can be seen (Figure 14).
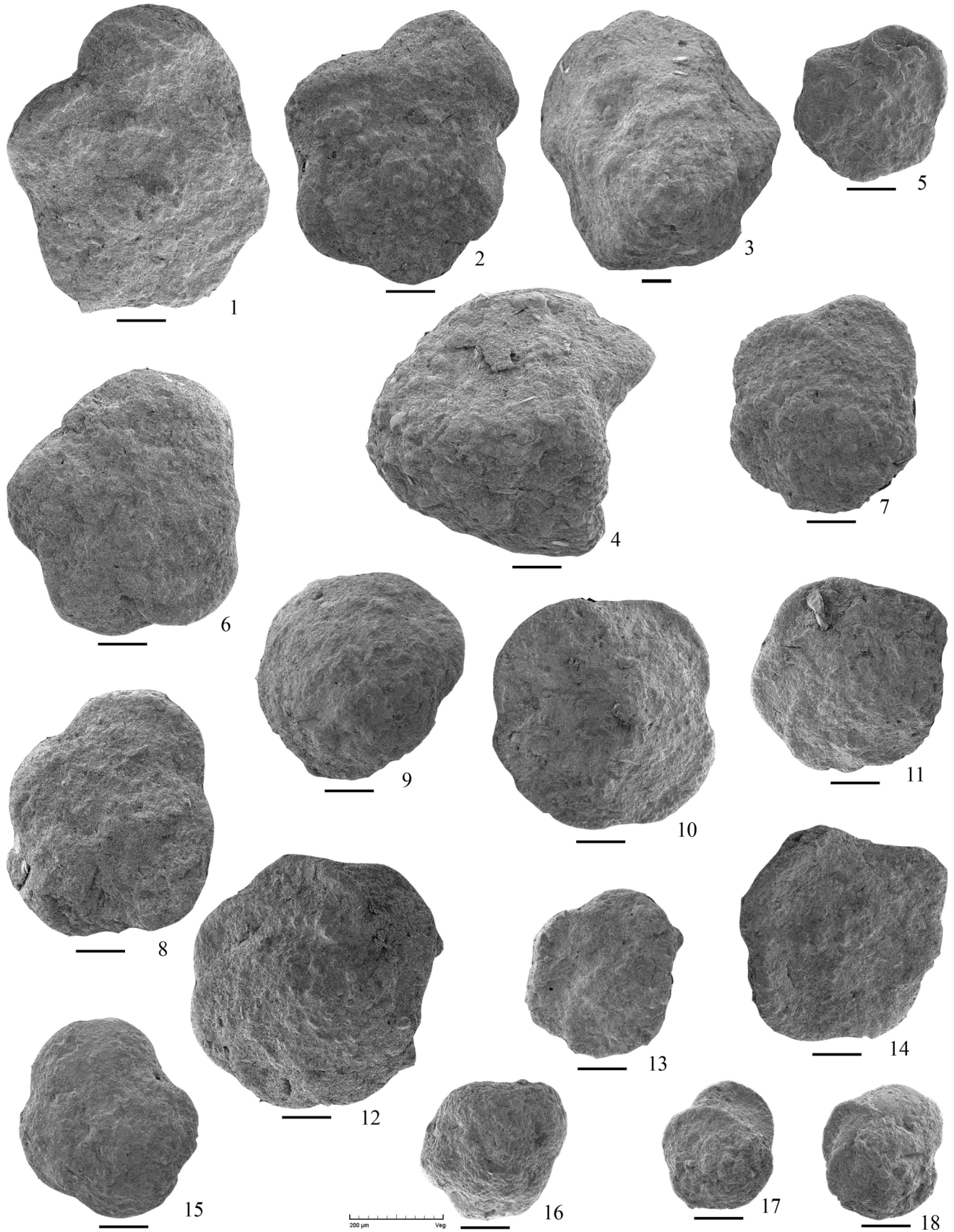
Table 2. Whole-rock chemistry (wt %) of the Gams section samples

Sample	Distance from K/T boundary, cm	SiO₂	TiO₂	Al₂O₃	Fe₂O₃	MnO	MgO	CaO	Na₂O	K₂O	P₂O₅	Al₂O₃/TiO₂	SiO₂/Al₂O₃
C4	−14	26.94	0.39	8.23	2.33	0.11	1.07	29.86	0.48	1.25	0.06	21.1	3.27
D4	−12	22.78	0.31	6.89	2.29	0.13	1.00	34.17	0.36	1.08	0.06	22.2	3.30
E4	−10	17.97	0.24	5.31	2.12	0.16	0.80	36.45	0.28	0.89	0.07	22.2	3.38
F4	−8	17.24	0.22	5.08	2.10	0.16	0.79	37.47	0.24	0.86	0.07	23.1	3.39
G3	−6	19.81	0.26	6.14	2.19	0.13	0.89	35.2	0.24	0.97	0.07	21.2	3.23
H6	−4	20.93	0.28	5.52	2.59	0.13	1.97	34.62	0.22	0.95	0.08	19.7	3.79
I3	−2	22.27	0.29	6.83	2.43	0.11	0.97	33.06	0.26	1.08	0.06	23.6	3.26
J2/2	0	57.87	0.97	19.19	7.97	0.03	2.88	5.30	0.56	3.98	0.07	19.8	3.01
J2/3	0.4	62.33	0.92	19.26	7.25	0.02	2.73	2.20	0.37	3.54	0.05	20.9	3.23
J2/4	0.8	61.85	0.89	19.54	7.23	0.02	2.56	2.61	0.40	3.34	0.06	22.0	3.19
J2/5	1.2	61.85	0.91	19.37	7.37	0.02	2.76	2.50	0.42	3.46	0.06	21.3	3.19
J2/6	1.6	61.77	0.91	18.85	7.43	0.02	2.37	2.54	0.40	3.43	0.06	20.7	3.27
J7	0	55.00	0.95	16.90	6.96	0.03	2.99	1.74	0.46	3.32	0.07	17.8	3.25
K2	2	50.90	0.65	5.71	3.47	0.06	1.06	18.27	0.99	1.02	0.04	8.8	8.91
K4	2	46.78	0.62	8.87	3.67	0.06	1.27	17.92	0.90	1.42	0.05	14.3	5.27
K5	2	50.68	0.64	8.27	4.74	0.07	0.92	22.08	0.68	1.67	0.01	12.9	6.13
L6	4	51.24	0.80	13.37	6.18	0.04	2.10	8.40	0.86	2.26	0.07	16.7	3.83
L6	4	56.81	0.87	14.45	6.53	0.03	1.72	10.93	0.59	2.62	0.04	16.6	3.93
M4	6	50.50	0.79	13.88	5.90	0.04	2.34	8.62	0.90	2.30	0.07	17.6	3.64
M7	6	55.22	0.89	15.13	6.74	0.03	2.33	11.08	0.95	2.94	0.09	17.0	3.65
N6	8	54.14	0.89	15.54	6.62	0.04	2.27	12.43	0.92	2.89	0.08	17.5	3.48
O2	10	55.40	0.83	15.95	7.21	0.03	2.48	11.06	0.44	2.71	0.05	19.2	3.47
O4/5	10	48.86	0.77	14.62	5.93	0.04	2.38	8.74	0.67	2.43	0.08	19.0	3.34
P7	12	54.57	0.82	13.90	6.94	0.04	2.67	12.77	0.43	2.63	0.05	17.0	3.92
P5/6	12	46.65	0.72	12.80	7.45	0.04	2.22	10.64	0.55	2.29	0.08	17.8	3.64
Q3	14	56.80	0.84	15.18	6.93	0.04	1.83	6.93	0.69	2.84	0.05	18.1	3.74
R2	16	54.11	0.81	15.12	7.59	0.04	2.37	12.43	0.60	2.63	0.05	18.7	3.58
S7	18	70.14	0.67	7.98	2.40	0.09	1.23	11.35	1.55	1.55	0.07	11.9	8.79
T4/5	20	68.30	0.69	8.24	2.99	0.06	0.84	12.12	0.93	1.60	0.04	11.9	8.29
U8	22	55.96	0.88	15.98	7.31	0.05	2.83	11.52	0.52	2.70	0.06	18.2	3.50

The upper part consists of clays of dark gray to black color (units *L–R*). Layering is discernible only in the topmost portion of the sequence, which contains carbonate layer *S* of pale gray color.

[64] Table 2 presents data on the bulk-rock composition of the samples taken over the whole vertical section of the Gams stratigraphic sequence. It can be seen that the contents of such components as SiO₂, Al₂O₃, CaO, and K₂O definitely divide the section into three parts.

[65] The lower part (units *C–I*) has low concentrations of SiO₂, Al₂O₃, and K₂O and high contents of CaO. In the middle part (layer *J*), whose composition was determined

---

Figure 10. Planktonic foraminifers Globotruncanidae, Scale bar = 100 μm.
1, 2, 14 – *Abathomphalus mayaroensis* (Bolli), spiral side, 1 – sample D-4, 2 – sample I-6, 14 – sample I-6;
3, 4 – *Contusotruncana contusa* (Cushman), 3 – spiral side, sample D-4, 4 – peripheral side, sample, D-4;
5, 12 – *Globotruncanita stuarti* (de Lapparent), spiral side, 5 – sample D-4, 12 – sample I-6;
6, 8 – *Gansserina gansseri* (Bolli), spiral side, 6 – sample E-3, 8 – sample D-4;
⇐   7, 11 – *Globotruncana arca* (Cushman), spiral side, 7 – sample H-6, 11 – sample C-6;
9 – *Contusotruncana walfischensis* (Todd), spiral side, sample H-6;
10 – *Globotruncanita stuartiformis* (Dalbiez), spiral side, sample C-6;
13 – *Globotruncana gagnebini* (Tilev), spiral side, sample H-6;
15 – *Globotruncanella* sp., spiral side, sample E-3;
16 – Globotruncanella sp., spiral side, sample H-6;
17, 18 – *Globotruncana rosetta* (Carsey), spiral side, 17 – sample C-6, 18 – sample C-6.
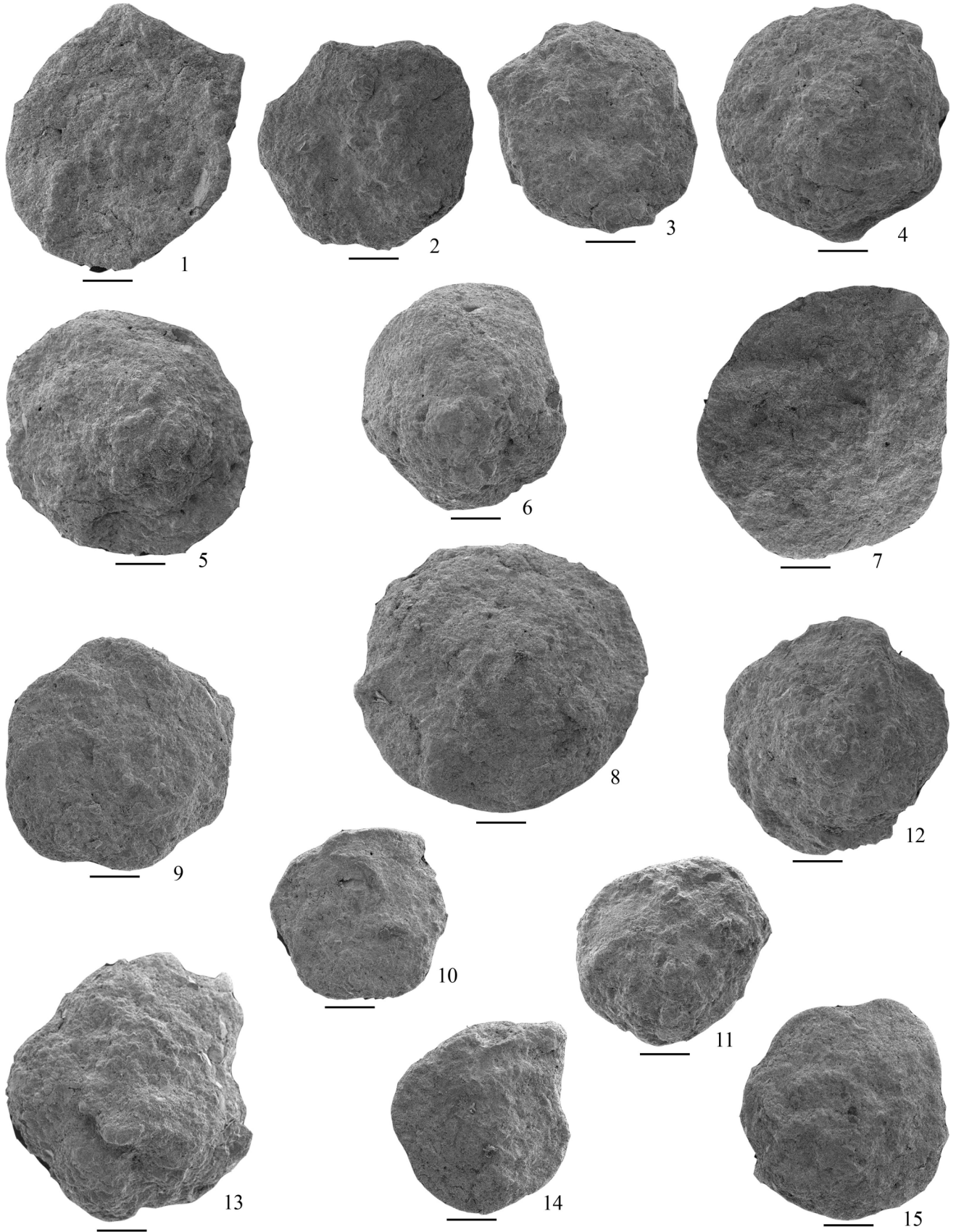
Table 3. Normative mineral composition (%) of the Gams section samples

Sample	Distance from K/T boundary. cm	Ab	An	Or	Q	Mm	Ill	Chl	Kn	Cc	Ank	Rch	Ap	Rt	Ore	Total
C4	−14	0.65	0.07	−	10.59	15.04	13.91	1.87	−	53.72	3.41	0.19	0.15	0.41	0.56	99.82
D4	−12	0.51	0.06	−	9.46	10.96	11.85	2.63	−	61.13	2.72	0.22	0.15	0.32	0.47	99.79
E4	−10	1.05	0.11	−	8.64	6.18	10.11	3.15	−	67.94	2.11	0.28	0.18	0.26	0.44	99.73
F4	−8	0.77	0.08	−	8.39	5.76	9.70	3.21	−	69.43	1.98	0.27	0.18	0.23	0.41	99.73
G3	−6	−	−	−	8.75	8.98	10.92	2.78	0.61	64.78	2.52	0.22	0.17	0.27	0.44	99.78
H6	−4	1.95	0.21	0.42	17.72	9.17	9.86	9.17	−	63.85	−	0.22	0.20	0.29	0.49	100.06
I3	−2	−	−	−	10.09	9.73	12.16	3.04	0.84	60.67	2.82	0.19	0.15	0.31	0.49	99.81
J2/2	0	2.80	0.30	−	25.40	6.91	39.95	12.70	−	6.72	4.10	0.05	0.16	0.91	1.07	99.95
J2/3	0.4	−	−	−	29.63	12.57	36.18	10.67	3.61	1.33	4.99	0.03	0.11	0.88	0.99	99.97
J2/4	0.8	−	−	−	28.59	13.52	33.98	9.84	5.67	1.63	5.75	0.03	0.14	0.85	0.99	99.97
J2/5	1.2	−	−	−	28.37	14.21	35.23	10.55	3.58	1.60	5.43	0.03	0.14	0.87	1.01	99.98
J2/6	1.6	−	−	−	29.56	13.64	35.19	9.01	3.63	1.00	6.93	0.03	0.14	0.87	1.01	99.97
K2	2	8.62	0.92	4.21	39.38	−	3.61	8.84	−	32.77	0.79	0.05	0.10	1.02	0.77	99.91
K4	2	6.78	0.72	−	31.13	4.45	15.64	6.61	−	31.47	2.34	0.10	0.12	0.54	0.76	99.60
K5	2	5.25	0.56	−	33.35	−	16.28	4.25	−	32.09	5.82	0.01	0.02	0.58	0.60	99.90
L6	4	5.50	0.58	−	29.09	9.24	25.56	11.02	−	13.37	4.55	0.07	0.18	0.85	1.03	99.94
L6/1	4	1.09	0.12	−	28.69	15.03	26.20	5.19	−	14.12	8.61	0.05	0.09	0.81	0.90	99.86
M4	6	5.32	0.56	−	26.64	11.42	25.96	11.08	−	14.05	3.89	0.07	0.18	0.83	1.01	99.93
M7	6	7.37	0.78	−	28.68	0.77	29.54	12.46	−	17.07	2.24	0.05	0.20	0.84	1.04	99.95
N6	8	5.65	0.60	−	37.85	6.44	28.52	10.28	−	18.33	3.78	0.06	0.18	0.82	1.00	99.95
O2	10	−	−	−	25.70	14.39	26.66	9.73	1.37	15.31	5.93	0.04	0.20	0.76	0.87	99.96
O4/5	10	1.75	0.19	−	23.13	17.84	27.47	9.42	−	13.73	5.40	0.07	0.20	0.81	1.01	99.94
P7	12	2.19	0.23	−	29.99	5.00	26.16	13.11	−	19.82	2.56	0.06	0.11	0.76	0.87	99.93
P5/6	12	4.12	0.44	−	27.99	3.41	25.96	15.11	−	17.92	4.01	0.07	0.20	0.76	0.96	99.92
Q3	14	2.90	0.31	−	36.36	12.08	30.03	7.42	−	8.29	8.02	0.06	0.12	0.83	0.95	99.94
R2	16	1.90	0.20	−	25.68	11.58	25.08	10.54	−	17.39	5.99	0.06	0.11	0.74	0.85	99.93
S7	18	12.13	1.29	1.19	48.91	−	13.17	−	−	17.82	4.60	0.13	0.15	0.62	0.77	99.88
T4/5	22	7.39	0.79	0.66	50.09	−	14.89	−	−	19.22	1.60	0.09	0.09	0.65	0.74	99.92
U8	24	0.24	0.03	−	24.91	15.71	26.12	10.75	−	16.06	5.19	0.07	0.13	0.80	0.93	99.64

Note: Ab – Albite, An – Anortite, Or – Orthoclase, Q – Quartz, Mm – Montmorillonite, Ill – Illite, Chl – Chlorite, Kn – Kaolinite, Cc – Calcite, Ank – Ankerite, Rch – Rhodochrosite, Ap – Apatite, Rt – Rutile, Ore – Ore mineral.

at spots spaced 0.4 cm apart, the concentrations of SiO_2, Al_2O_3, and K_2O dramatically increase, and the concentrations of CaO and MnO notably decrease. The transition to the upper part of the sequence occurs through intermediate layer K, the contents of which Al_2O_3, FeO, CaO, Na_2O, and K_2O differ from those in both the underlaying and overlaying rocks. The top of the sequence (units $L–U$, except layers

S and T) shows insignificant compositional variations.

[66] As it is fairly difficult to quantitatively determine the mineralogical composition of clay-rich sedimentary rocks, we recalculated the bulk chemical compositions of these rocks into normative minerals by the computer program [*Rosen et al.,* 2004]. This allowed us to determine that, starting with layer J, the concentrations of normative quartz and clay

Figure 11. Planktonic foraminifers Globotruncanidae and Rugoglobigerinidae, Scale bar = 100 μm.
1, 2, 3, 4 – *Globotruncanita subspinosa* (Pessagno), spiral side, 1 – sample I-6, 2 – sample G-2, 3 – sample E-3, 4 – sample E-3;
5, 6 – *Contusotruncana walfischensis* (Todd), spiral side, 5 – sample H-6, 6 – sample E-3;
7, 8 – *Globotruncanita stuarti* (de Lapparent), spiral side, 7 – sample D-4, 8 – sample H-6;
$\Leftarrow$　9 – *Rosalinella* cf. *linneiana* (d'Orbigny), spiral side, sample G-2;
10 – *Globotruncana gagnebini* (Tilev), spiral side, sample E-3;
11, 12 – *Globotruncana rosetta* (Carsey), spiral side, 11 – sample C-6, 12 – sample D-4;
13 – *Rugoglobigerina rugosa* (Bronnimann), spiral side, sample D-4;
14 – *Globotruncanita andori* (Klaus), spiral side, sample C-6;
15 – *Globotruncana arca* (Cushman), spiral side, sample D-4.
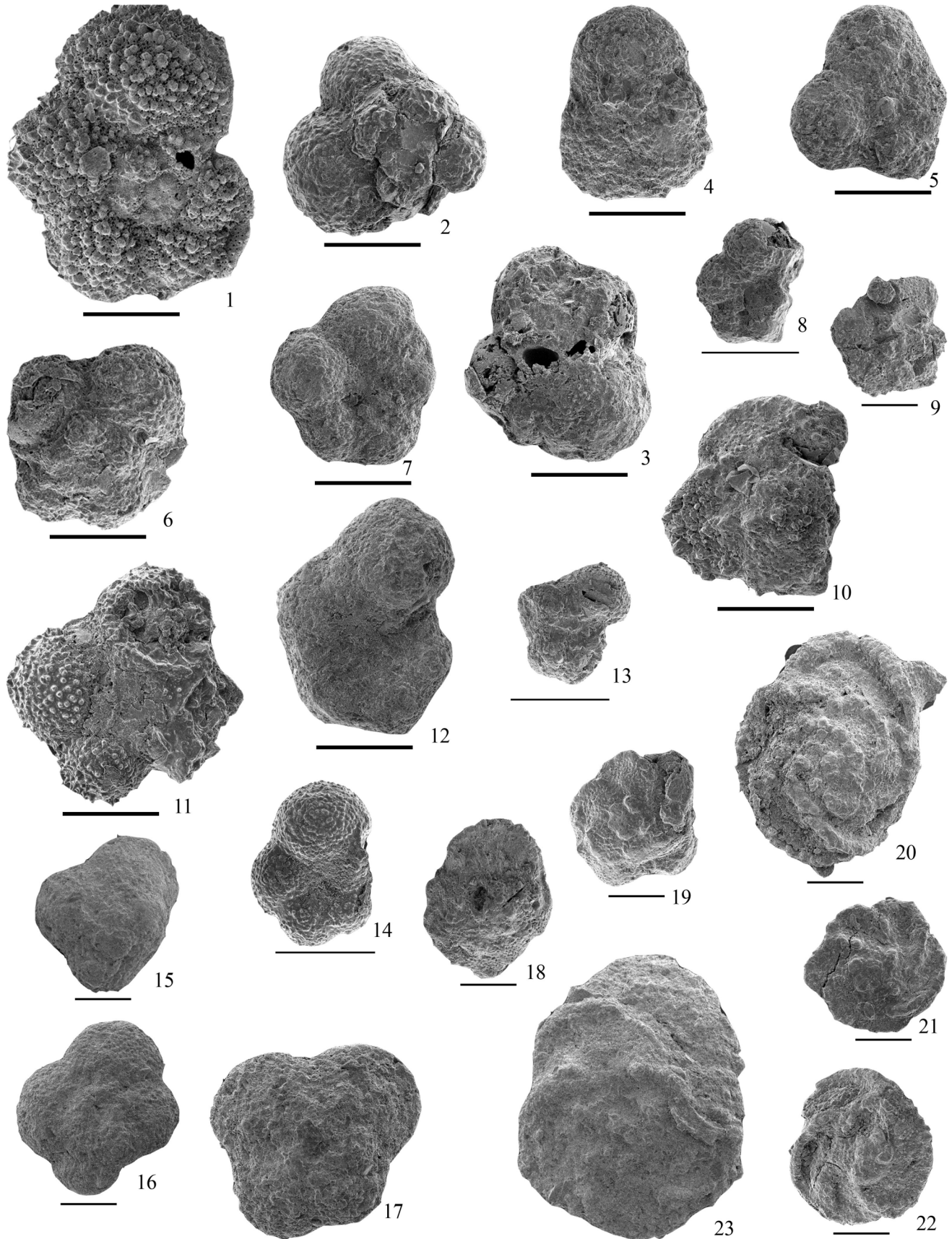
Figure 13. Photograph of transition layer J at the K/T boundary. Note the color and character of bottom and top of layer J.

Figure 14. Slickensides on the surface of layer K.

minerals notably increase, whereas the content of calcite decreases (Table 3). The contents of quartz and plagioclase display a strong correlation ($r = 0.8$) but are not correlated with the amounts of other minerals, a fact highlighting the terrigenous nature of these minerals. It should be mentioned that the mineralogical analysis of the heavy fraction has revealed that it contained, along with quartz, detrital zircon in layer J and all layers above it (Figure 15). These layers also contain garnet, epidote, and ore minerals [*Kollmann*, 1964].

[67] An important characteristic of the Gams sequence is a drastic increase in the amount of terrigenous material in the upper part of the sequence: the percentages of normative quartz and feldspathoids (which weakly vary in the bottom part of the sequence and amount to approximately 10%) increase to 40–70% above layer J (Table 3).

[68] As follows from Figure 16 and Table 3, layer K differs

from both the overlying and underlaying rocks, and layer J has the minimum concentration of normative calcite but is rich in terrigenous components, a feature that makes it similar to the upper portion of the succession. The anomalous character of layer K can be readily explained, because it has the shape of a lens, which was produced by a submarine landslide, as follows from the occurrence of slickensides (Figure 14).

[69] It is pertinent to list the principal trends in the variations in the contents of major components in the vertical section of the Gams sequence. Although correlation analysis reveals a linear character of correlations between major components in the lower and upper parts of the sequence and in its transitional layer J (Tables 4, 5, and 6), it does clearly illustrate the similarities and differences. This can be done using the technique of principal components of factor analysis (Table 7). Figure 17 presents a diagram of factors 1 and 2 on

---

⇐

Figure 12. Planktonic foraminifers Globotruncanidae, Hedbergellidae and Globogerinidae, Scale bar=100 μm.

1 – *Parasubbotina pseudobulloides* (Plummer), spiral side, sample R-6;

2, 3 – *Globoconusa daubjergensis* (Bronnimann), spiral side: 1 – sample J-8/9c, 2 – sample J-8/9c;

4, 5 – *Subbotina fringa* (Subbotina), spiral side: 4 – sample M-4, 5 – sample M-4;

6, 7 – *Eoglobigerina edita* (Subbotina), 6 – spiral side, sample M-4, 7 – umbilical side, sample M-4;

8 – *Globigerina*-like form (close to *Globigerina compressa* Plummer var. *compressa* Plummer sensu Subbotina, 1953, pl.II, Figure 4), umbilical side, sample R-6;

9, 10 – (?) *Morozovella* sp., spiral side, 9 – sample M-4, 10 – sample M-4;

11 – *Hedbergella holmdelensis* (Olsson), umbilical side, sample J-8/9a;

12, 13, 14 – *Hedbergella monmouthensis* (Olsson), umbilical side, 12 – sample I-6, 13 – sample J-8/9a, 14 – sample J-8/9a;

15 – *Globotruncanella havanensis* (Voorwijk), spiral side, sample H-6;

16 – *Globotruncanella* sp., spiral side, sample H-6;

17 – *Hedbergella* sp., spiral side, sample I-6;

18–22 – *Globotruncana rosetta* (Carsey), spiral side: 18 – sample M-4, 19 – sample J-8/9c, 20 – sample J-8/9a, 21 – sample J-8/9, 22 – sample J-8/9a;

23 – *Globotruncana gagnebini* (Tilev), spiral side, sample C-6.

Table 4. Correlation matrix of the major elements for the lower part of the Gams section (units C–I)

	SiO_2	TiO_2	Al_2O_3	Fe_2O_3	MnO	MgO	CaO	Na_2O	K_2O	P_2O_5
SiO_2	1.00	0.99	0.96	0.50	−0.86	0.22	−0.98	0.82	0.98	−0.59
TiO_2	0.99	1.00	0.95	0.44	−0.80	0.21	−0.97	0.87	0.97	−0.56
Al_2O_3	0.96	0.95	1.00	0.28	−0.84	−0.06	−0.95	0.85	0.99	−0.76
Fe_2O_3	0.50	0.44	0.28	1.00	−0.66	0.86	−0.50	−0.02	0.38	0.16
MnO	−0.86	−0.80	−0.84	−0.66	1.00	−0.29	0.89	−0.45	−0.86	0.49
MgO	0.22	0.21	−0.06	0.86	−0.29	1.00	−0.20	−0.17	0.05	0.58
CaO	−0.98	−0.97	−0.95	−0.50	0.89	−0.20	1.00	−0.78	−0.97	0.56
Na_2O	0.82	0.87	0.85	−0.02	−0.45	−0.17	−0.78	1.00	0.84	−0.68
K_2O	0.98	0.97	0.99	0.38	−0.86	0.05	−0.97	0.84	1.00	−0.71
P_2O_5	−0.59	−0.56	−0.76	0.16	0.49	0.58	0.56	−0.68	−0.71	1.00

the basis of the matrix of factor loads (Table 7), the sum of which makes a very significant contribution to the total dispersion (>80%), and shows the composition data points of the discrete layers of the sequence. Figure 17 clearly demonstrates that the layers of all of the three parts of the sequence compose three discrete fields, with the definitely separated compositions of units K, T, and S. This separation is related, first of all, to factor 1 (Al, K, Fe***, Mg, Ti, Si/Mn, and Ca), in which Mn and Ca are opposed to the other principal components (Table 7). It is pertinent to mention that layer J is characterized by elevated concentrations of K_2O, Al_2O_3, Fe_2O_3, and TiO_2 at a very low content of CaO. The variations in the concentrations of some elements in the vertical section are displayed in Figure 18.

[70] It is worth noting the Al_2O_3/TiO_2 ratio, which varies generally insignificantly in the Gams sequence below and above transitional layer J and remains within the limits of 17–23. The exceptions are layers K, S, and T, the Al_2O_3/TiO_2 ratio decreases to 9–13. In this context, it is pertinent to recall the well-known conclusion that "...the

constancy of the Al_2O_3/TiO_2 ratio in sedimentary rocks is an indication of the terrigenous genesis of these rocks" [*Strakhov,* 1962, p. 190].

[71] N. M. Strakhov also emphasized that variations in the concentrations of Al_2O_3 and TiO_2 during the post-Proterozoic evolution of the Earth are correlated. This fact led Strakhov to conclude that "...this correlation is established already when eluvium is formed and is later preserved when clays are redeposited mechanically in finite basins, for example, in seas" [*Strakhov,* 1962, p. 103]. An analogous viewpoint was expressed by *Lisitsyn* [1978]: "...The asso-
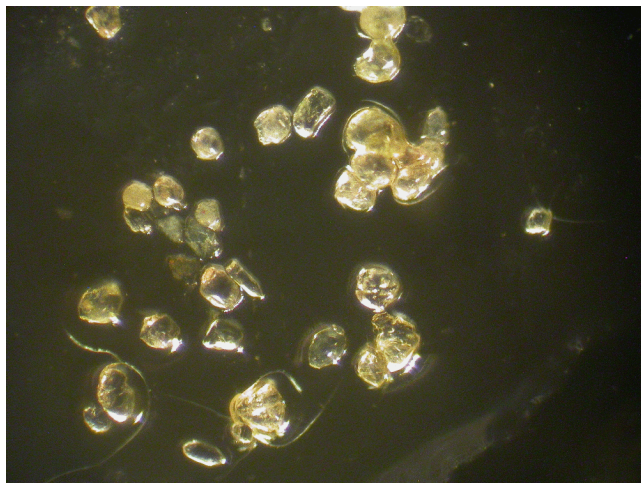
Figure 15. Rounded zircon grains as a characteristic feature of the upper portion of the Gams section.
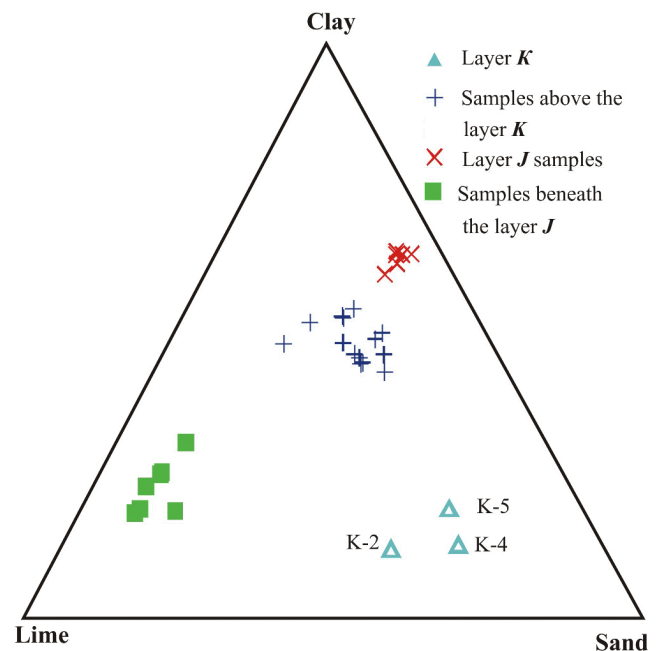
Figure 16. Diagram of Lime-Clay-Sand components for the Gams sections samples.

Table 5. Correlation matrix of the major elements for the transition layer of the Gams section (layers $J2$–$J6$)

	SiO$_2$	TiO$_2$	Al$_2$O$_3$	Fe$_2$O$_3$	MnO	MgO	CaO	Na$_2$O	K$_2$O	P$_2$O$_5$
SiO$_2$	1.00	−0.90*	0.13	−0.97*	−0.99*	−0.56	−1.00*	−0.99*	−0.93*	−0.86
TiO$_2$	−0.90*	1.00	−0.29	0.93*	0.93*	0.67	0.89*	0.87	0.99*	0.59
Al$_2$O$_3$	0.13	−0.29	1.00	−0.32	−0.11	0.43	−0.10	−0.08	−0.19	−0.10
Fe$_2$O$_3$	−0.97*	0.93*	−0.32	1.00	0.96*	0.50	0.96*	0.97*	0.93*	0.84
MnO	−0.99*	0.93*	−0.11	0.96*	1.00	0.62	0.99*	0.97*	0.96*	0.79
MgO	−0.56	0.67	0.43	0.50	0.62	1.00	0.56	0.59	0.71	0.27
CaO	−1.00*	0.89*	−0.10	0.96*	0.99*	0.56	1.00	0.99*	0.92*	0.86
Na$_2$O	−0.99*	0.87*	−0.08	0.97*	0.97*	0.59	0.99*	1.00	0.90*	0.90*
K$_2$O	−0.93*	0.99*	−0.19	0.93*	0.96*	0.71	0.92*	0.90*	1.00	0.62
P$_2$O$_5$	−0.86	0.59	−0.10	0.84	0.79	0.27	0.86	0.90*	0.62	1.00

Note: * Marked correlations are significant at $p < 0.05000$.

Table 6. Correlation matrix of the major elements for the upper part of the Gams section (units K–T)

	SiO$_2$	TiO$_2$	Al$_2$O$_3$	Fe$_2$O$_3$	MnO	MgO	CaO	Na$_2$O	K$_2$O	P$_2$O$_5$
SiO$_2$	1.00	−0.30	−0.55	−0.75*	0.65*	−0.59*	−0.00	0.66*	−0.49	−0.18
TiO$_2$	−0.30	1.00	0.92*	0.72*	−0.79*	0.77*	−0.51	−0.37	0.94*	0.39
Al$_2$O$_3$	−0.55	0.92*	1.00	0.88*	−0.90*	0.89*	−0.52	−0.57	0.97*	0.42
Fe$_2$O$_3$	−0.75*	0.72*	0.88*	1.00	−0.88*	0.82*	−0.24	−0.79*	0.88*	0.20
MnO	0.65*	−0.79*	−0.90*	−0.88*	1.00	−0.81*	0.46	0.75*	−0.85*	−0.29
MgO	−0.59*	0.77*	0.89*	0.82*	−0.81*	1.00	−0.47	−0.54	0.83*	0.54
CaO	− 0.00	− 0.51	−0.52	−0.24	0.46	− 0.47	1.00	−0.09	−0.43	−0.71*
Na$_2$O	0.66*	−0.37	−0.57	−0.79*	0.75*	−0.54	−0.09	1.00	−0.58*	0.25
K$_2$O	−0.49	0.94*	0.97*	0.88*	−0.85*	0.83*	−0.43	−0.58*	1.00	0.33
P$_2$O$_5$	−0.18	0.39	0.42	0.20	−0.29	0.54	−0.71*	0.25	0.33	1.00

Note: * Marked correlations are significant at $p < 0.05000$.

ciation of clay minerals in marine sediments is predetermined already in the drainage basins, i.e., the clay minerals of the World Ocean are not authigenic by terrigenous. Their systematic distributions correspond to the systematic distributions of terrigenous particles of corresponding size" [*Lisitsyn,* 1978, p. 156]. This conclusion has been also confirmed (with some limitations) by the latest studies of clay minerals [*Thiry,* 2000].

Table 7. Factor loadings matrix of the major elements for the Gams section (marked loadings are >0.7)

	Layers C–I		Layers $J2$–$J6$		Layers K–U	
	Factors		Factors		Factors	
	1	2	1	2	1	2
SiO$_2$	0.95*	0.22	0.12	−0.95*	−0.77*	0.13
TiO$_2$	0.94*	0.18	0.52	0.77*	0.71*	0.54
Al$_2$O$_3$	0.97*	−0.04	0.51	−0.80*	0.87*	0.46
Fe$_2$O$_3$	0.32	0.90*	0.96*	−0.14	0.97*	0.11
MnO	−0.81*	−0.38	0.42	0.80*	−0.91*	−0.27
MgO	−0.01	0.96*	0.08	0.81	0.80*	0.46
CaO	−0.94*	−0.22	0.97*	0.07	−0.15	−0.88*
Na$_2$O	0.85*	−0.25	0.74*	0.62	−0.87	0.36
K$_2$O	0.98*	0.06	0.94*	0.95	0.86	0.39
P$_2$O$_5$	−0.73*	0.53	0.34	0.50	0.09	0.87*
Total	66%	24%	41.6%	41.0%	58%	26%
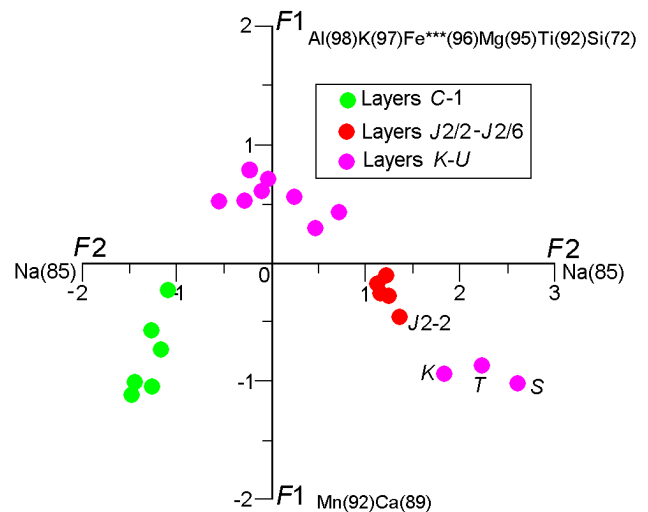
Figure 17. Factor diagram for the Gams sections samples.

Table 8. Trace elements concentrations (ppm) for the Gams section samples

Distance from K/T boundary, cm	Layer	Cr	Ni	Co	Sc	V	Cu	Pb	Zn	Bi	W	Mo	Rb	Cs	Ba	Sr	Tl	Ga	Ta	Nb	Hf	Zr	Y	Th	U
−14	C	137	22	3	nd	46	112	nd	69	nd	nd	nd	36	nd	165	397	nd	nd	nd	nd	nd	61	17	nd	nd
−12	D	86	23	7	nd	44	24	nd	56	nd	nd	nd	33	nd	153	418	nd	nd	nd	nd	nd	46	19	nd	nd
−10	E	76	21	3	nd	36	13	nd	25	nd	nd	nd	27	nd	99	398	nd	nd	nd	nd	nd	36	19	nd	nd
−8	F	65	21	5	nd	40	21	nd	21	nd	nd	nd	24	nd	113	420	nd	nd	nd	nd	nd	33	21	nd	nd
−6	G	60	24	9	nd	40	17	nd	23	nd	nd	nd	29	nd	100	433	nd	nd	nd	nd	nd	35	20	nd	nd
−4	H	44	64	18	7	51	25	7	39	0.3	16	0.57	59	2.6	162	881	0.36	9	1.03	6.1	1.46	54	25	4.5	1.13
−2	I	54	76	22	11	61	26	7	49	0.24	17	0.44	68	3.2	218	884	0.39	11	1.01	7.6	1.72	61	26	5.6	1.04
0	J2	183	155	35	7	167	97	40	162	0.92	10	0.87	145	7.2	330	141	0.84	21	1.36	15.3	4.53	154	17	12.2	1.74
0.4	J3	172	171	38	8	180	88	40	169	1.16	8	0.66	159	7.9	372	127	1.01	2	1.51	17.1	4.76	167	19	14.0	1.89
0.8	J4	175	175	39	11	185	78	42	180	1.10	15	0.68	162	8.1	396	138	0.97	23	1.49	17.0	4.46	158	21	13.9	1.88
1.2	J5	259	173	38	10	177	66	39	177	0.97	20	0.55	156	7.6	411	179	1.08	23	1.45	16.7	3.00	179	20	14.4	1.89
1.6	J6	175	191	44	18	190	68	41	192	0.98	10	0.43	166	8.6	463	171	1.09	25	1.46	17.8	5.01	172	19	13.8	1.91
2	K	115	78	31	5	100	33	25	74	0.15	158	1.55	78	2.8	415	775	0.48	13	1.92	10.0	2.45	95	20	5.5	1.59
4	L	146	165	53	15	151	29	16	90	0.35	110	0.84	132	5.4	457	315	0.79	21	1.42	16.8	4.36	170	20	10.5	1.57
6	M	130	186	55	17	150	37	13	78	0.41	47	0.53	145	6.5	449	303	0.77	22	1.32	17.5	4.29	166	24	11.4	1.79
8	N	115	229	54	nd	161	63	nd	73	nd	nd	nd	132	nd	437	302	0.48	nd	nd	nd	nd	191	5	nd	nd
10	O	120	202	65	17	154	40	15	79	0.40	33	0.33	140	6.5	449	313	0.83	22	1.90	17.2	4.37	171	23	11.9	1.68
12	P	116	180	43	16	141	34	13	80	0.43	35	0.25	139	6.4	449	412	0.96	22	1.93	17.3	4.70	166	25	11.6	1.67
14	Q	94	119	43	Nd	120	51	15	80	nd	nd	nd	110	nd	387	247	nd	19	nd	16	nd	137	25	nd	nd
16	R	97	123	51	26	111	53	28	84	nd	nd	nd	100	nd	360	296	nd	22	nd	18	nd	128	25	nd	nd
18	S	64	73	93	nd	85	58	nd	54	nd	nd	nd	60	nd	553	413	nd	nd	nd	nd	nd	181	1	nd	nd
20	T	43	87	39	18	62	36	17	43	nd	nd	nd	49	nd	441	282	nd	9	nd	13	nd	139	20	nd	nd
22	U	95	112	60	17	96	83	35	120	nd	nd	nd	104	nd	400	289	nd	20	nd	18	nd	156	30	nd	nd

Note: nd – not determined.

Table 9. Rare earth element contents (ppm) of the Gams section samples

Sample	La	Ce	Pr	Nd	Sm	Eu	Gd	Tb	Dy	Ho	Er	Tm	Yb	Lu	$(La/Sm)_N$	$(La/Yb)_N$	Analytical method
H4	27.27	56.10	6.86	25.86	5.44	1.42	5.29	0.77	4.41	0.88	2.33	0.34	2.11	0.30	2.93	8.23	ICP-MS
I4	28.67	60.63	7.41	28.50	6.08	1.42	5.44	0.80	4.55	0.87	2.28	0.33	2.04	0.30	2.76	8.96	ICP-MS
J2/2	21.17	39.78	4.97	18.39	3.57	0.74	3.07	0.47	2.74	0.53	1.53	0.24	1.55	0.24	3.47	8.70	ICP-MS
J2/3	25.75	48.20	6.05	22.18	4.47	0.85	3.69	0.55	3.05	0.60	1.75	0.27	1.79	0.28	3.37	9.18	ICP-MS
J2/4	25.79	48.05	6.03	22.54	4.57	0.96	3.93	0.59	3.37	0.68	1.96	0.29	1.93	0.29	3.30	8.52	ICP-MS
J2/5	28.12	52.38	6.63	24.58	4.91	0.99	3.98	0.61	3.39	0.68	1.94	0.30	1.93	0.30	3.35	9.29	ICP-MS
J2/6	24.31	48.61	6.40	23.77	4.86	1.11	3.95	0.60	3.58	0.73	2.04	0.31	2.00	0.31	2.92	7.75	ICP-MS
J6	24.38	45.70	5.75	20.73	4.26	0.93	3.54	0.56	3.20	0.64	1.85	0.28	1.81	0.28	3.35	8.59	ICP-MS
K5	19.21	40.67	4.91	18.56	3.99	0.88	3.64	0.57	3.44	0.69	1.85	0.27	1.61	0.24	2.82	7.61	ICP-MS
K4	27.61	56.35	6.83	25.20	5.20	1.17	4.55	0.69	3.90	0.75	2.08	0.30	1.83	0.28	3.10	9.62	ICP-MS
L6	23.73	46.85	6.04	22.03	4.54	1.01	3.82	0.57	3.27	0.65	1.80	0.27	1.85	0.28	3.06	8.18	ICP-MS
L6*	26.67	51.13	6.60	24.43	5.08	1.12	4.49	0.67	3.83	0.76	2.14	0.31	2.01	0.31	3.08	8.46	ICP-MS
M7	27.70	54.54	7.21	27.38	5.66	1.30	4.52	0.67	3.97	0.76	2.17	0.32	2.12	0.32	2.86	8.33	ICP-MS
O4/5	27.70	55.34	7.33	27.26	5.63	1.24	4.56	0.68	3.78	0.73	1.97	0.30	2.00	0.30	2.88	8.83	ICP-MS
O2	28.43	55.76	7.30	27.10	5.65	1.21	4.52	0.68	3.77	0.74	2.04	0.32	2.02	0.30	2.95	8.98	ICP-MS
P7	29.77	61.18	8.10	29.76	6.30	1.39	5.19	0.75	4.31	0.82	2.28	0.33	2.19	0.32	2.76	8.67	ICP-MS
P5/6	28.33	56.81	7.37	27.38	5.78	1.37	4.68	0.71	4.03	0.76	2.09	0.32	2.04	0.30	2.87	8.83	ICP-MS
Q3	20.40	49.28	6.04	22.09	4.26	1.00	3.70	0.47	2.28	0.43	1.06	0.18	0.91	0.17	2.80	14.3	NAAA
R2	22.55	52.37	6.44	24.01	4.60	0.90	3.88	0.58	2.51	0.47	1.08	0.18	0.98	0.17	2.87	14.68	NAAA
S7	18.22	43.27	4.46	16.60	3.16	0.68	3.16	0.40	1.92	0.37	0.89	0.17	0.90	0.14	3.37	12.91	NAAA
T4/5	22.05	54.69	5.68	22.65	4.32	0.91	4.17	0.57	2.84	0.59	1.32	0.21	1.06	0.14	2.98	13.28	NAAA

Note: * – Element analyses for clay fraction.

Trace and Rare Earth Elements

[72] Tables 8 and 9 report the distribution of the concentrations of trace elements and REE in the vertical section of the sequence, and Table 10 presents the contents of Ir and some other chalcophile elements in transitional layer J at the K/T boundary. The variations of the most informative elements (lithophile Cr, V, Rb, Cs, Ba, Sr, Nb, and Zr; chalcophile Cu, Zn, and Ga; and siderophile Co, Ni, and Mo) are the most dramatic and mutually correlated in the vicinity of transitional layer J.

[73] In terms of the character of these variations, the lower part of the sequence (below layer J) notably differs from the upper part, which includes a number of units with anomalously high concentration of siderophile, chalcophile (Zn, Cu,

Table 10. Ir (ppb) and some others elements concentrations (ppm) in the transition J^* layer of the Gams section

Sample	As	Ag	Sb	Ir	Au	Br
Ja	57	<0.2	1.86	5.7±1	0.013	0.1
Ja/b	49	0.2	1.96	5.5±1	0.027	0.4
Jb	46	0.4	1.76	4.8±1	0.015	0.5
Jb/c	12	1.9	1.59	9.0±1	0.059	2.5
Jc	7.8	<0.2	1.37	3.1±1	0.012	0.7

Note: * See Figure 4 for samples position in the J layer.

and Ni), and some other elements (layers K, S) (Figures 19, 20). These variations in the upper part of the sequence were caused by the varying conditions in the source area of the sediments, which is also reflected in the amounts of normative quartz (Table 3).

[74] The results of correlation analysis for the upper and lower parts of the sequence and for the transitional layer (Tables 4, 5, and 6) reveal differences between the elemental correlations. The most illustrative example is offered by the behavior of Cu: layer J displays negative correlations of Cu with Ni, Co, Sc, V, and many other elements ($r > -0.7$), whereas these correlations are absent both below and above this layer. It is important to mention that this layer was found out to bear particles of native copper and gold (Figure 21).

[75] Since layer J is of particular interest, it was subdivided into a number of units (Figure 4) in order to determine how concentrations of Ir and other elements vary from the bottom to top of this layer. It was revealed that the Ir concentration drastically increases from 5 ppm to 9 ppm upward (from $J1$ to $J4$) and then drops to 3 ppb at $J5 - J6$ (Table 10). The contents of As, Pb, Ag, Au, and Br also change in the same units (Figure 20).

[76] In contrast to trace elements, variations in the concentrations of REE in the Gams sequence are insignificant (Table 10). In a few samples, REE were analyzed in their whole-rock material and clay fractions. The REE concentration in sample L6 is systematically higher in the clay fraction than in the whole-rock sample.

[77] The chondrite-normalized REE patterns of the Gams

Figure 18. Variations of Al_2O_3, CaO, Fe_2O_3 and K_2O above and below the K/T boundary at the Gams section.

sequence generally confirm the known characteristic of clayey shales, namely, their uniform REE patterns [*Taylor and McLennan,* 1985]. The most conspicuous features of the REE patterns of the rocks is their pronounced enrichment in LREE and weak Eu anomalies. Compared with the REE patterns of North American Clayey Shales (NASC) (Figure 22), our rocks are poorer in HREE. Figures 23, 24 and 25 demonstrate the NASC-normalized REE patterns of the upper and lower parts of the rock sequence and its transitional layer *J*. All of these patterns are similar and show weakly pronounced negative anomalies at Ce, Nd, and Dy.

[78] This flat configuration of the NASC-normalized REE patterns is typical of the rocks of Mesozoic and Cenozoic continental margins (including those in the modern Atlantic)

[*Murray,* 1994] and testify to a significant contribution of terrigenous material to the character of REE fractionation. In this context, the similarities in the REE patterns of rocks from the examined portion of the Gams sequence suggest that the conditions in the source area (which was not far from the marine basin) did not vary.

Composition of Clay Minerals

[79] The mineralogical analysis of samples of the fraction <4 μm was conducted by means of X-ray diffraction on a D/MAX-2200m diffractometer. The raw specters were then
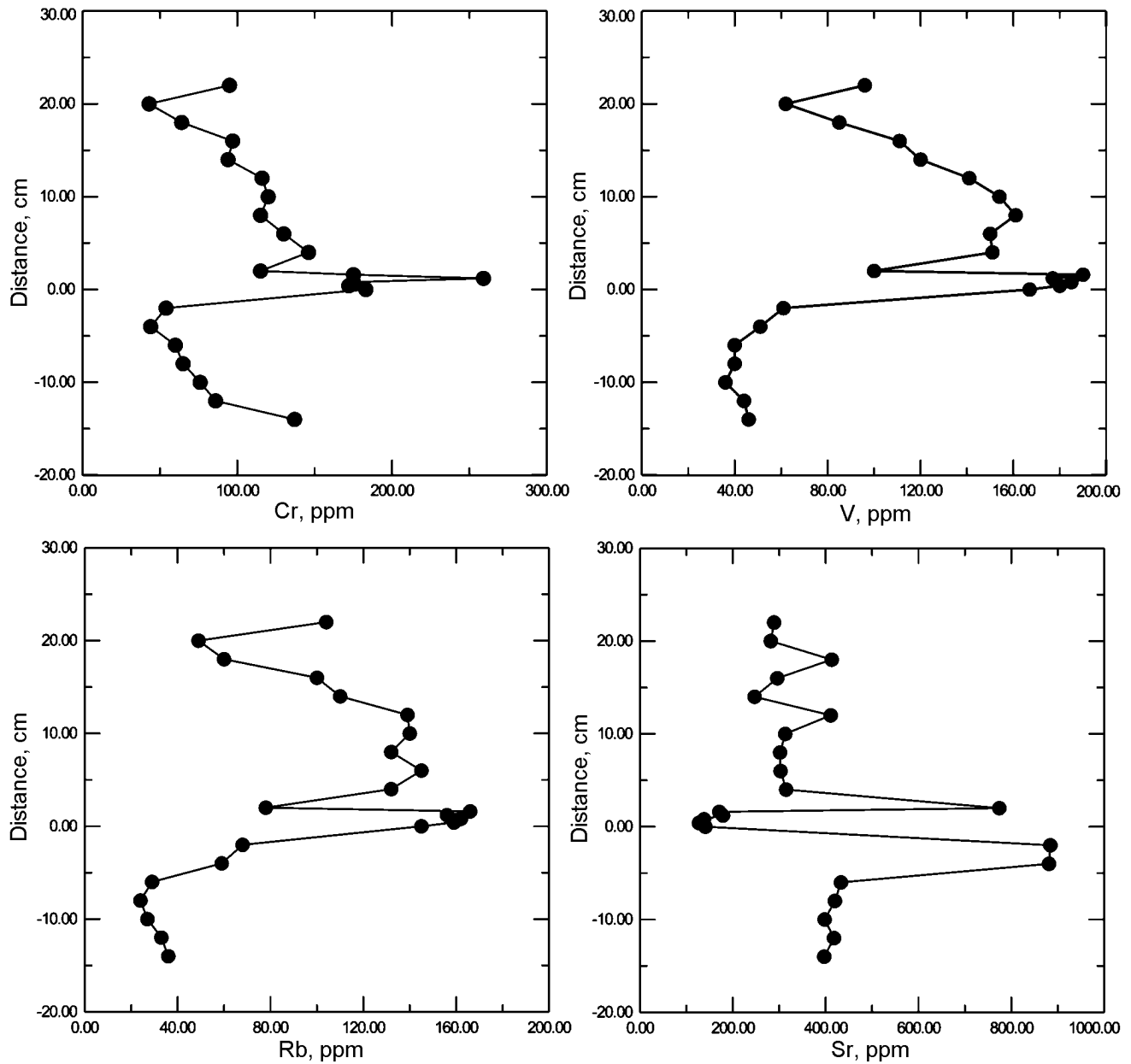
Figure 19. Variations of Cr, V, Rb and Sr concentrations above and below the K/T boundary at the Gams section.

processed by the Jade-6.0 (MDI, United States) computer program. The quantitative proportions of clay minerals were calculated using the basal reflections in a saturated state, following the method described in [*Biskaye,* 1965]. The sums of clay minerals were normalized to 100%.

[80] The identified clay minerals are smectite (*Sm*), illite (*Il*) of the muscovite series, and chlorite (*Ch*). The proportions of clay minerals are listed in Table 11. The absence of kaolinite or its insignificant contents (no more than 5%, which is close to the detection limit of the method) is an important indication of the paleogeographic environment in source area of the sediments (see below).

[81] As follows from Table 11, the upper part of the se-

quence (above layer *K*) is characterized by the occurrence of a relatively homogeneous assemblage of clay minerals, which is dominated by smectite (37–62%) and illite (29–45%). An analogous assemblage was also found below layer *J*. The situation with layer *K* is different: its illite fraction amounts to 70.5%, perhaps due to the intensification of erosion in the source area, because this mineral is usually formed during the erosion of crystalline rocks [*Deconinck et al.,* 2000].

[82] Of particular interest is layer *J*, smectite and chlorite contents of which are equal and whose clay mineral assemblage of it is smectite–chlorite–illite (Table 11). Smectite in sample *J*-6 has a composition different from those in other samples. The more detailed examination of the compositions
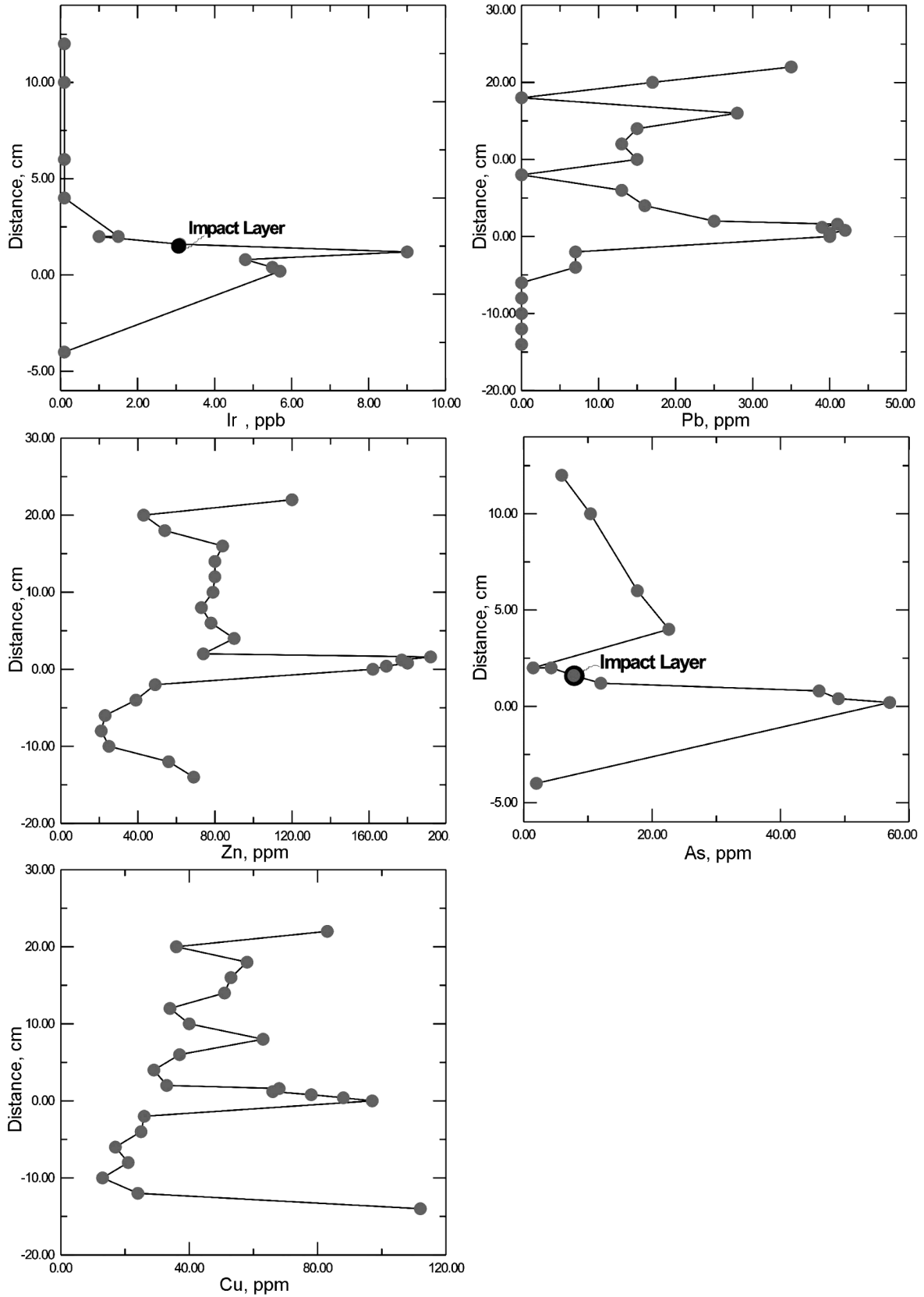
Figure 20. Variations of concentrations above and below the K/T boundary at the Gams section.
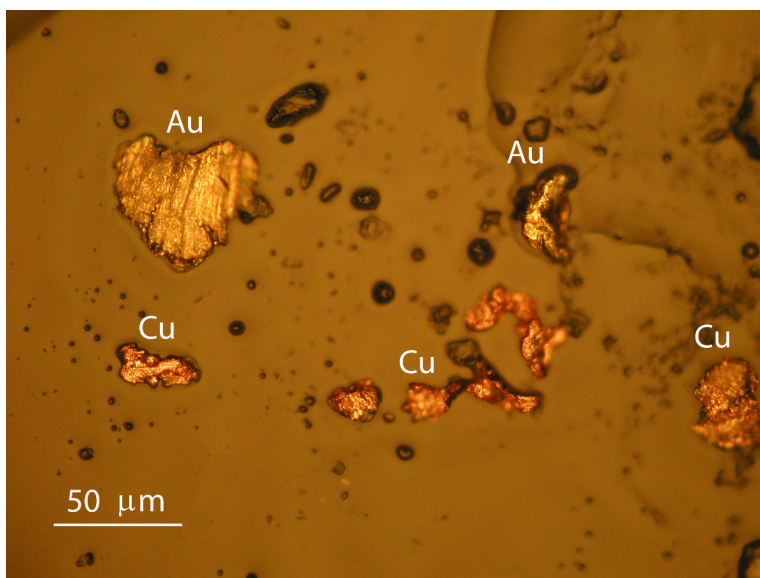
Figure 21. Disrupted and skeletal grains of Cu and Au in layer *J*-6/2.

within layer *J* (Table 12) has revealed that, having relatively high contents of clay minerals, this layer shows an increase in the ratio of clay to non-clay minerals from *Ja* to *Jc*. The illite content also simultaneously increases, whereas that of smectite decreases.

[83] The changes in the spacings of smectites in the air-dry state suggest different occupancies of the crystallographic sheets: Na–Ca smectite (13.0 Å) is contained in unit J_a, Na–Ca smectite with Ca predominance (13.9 Å) occurs in unit J_b, and Ca-smectite (14.5 Å) is borne in J_c. These conclusions are of preliminary character and require further X-ray diffraction studies.

[84] Nevertheless, it is important that the lower part of layer *J* (unit *J-a*) has a smectite content of >65%, and it systematically decreases upward, whereas the percentage of illite increases to 20% (Table 12). Taking into account that

this layer was found out to contain titanomagnetite of composition corresponding to the composition of this mineral in basalts, it can be concluded that smectite was formed at the expense of volcanic material.

[85] In interpreting data on the composition of clay minerals from the Gams sequence, which corresponds to a very brief time span (of the order of ten thousand years at conservative estimates of the sedimentation rate), it should be noted that these variations could hardly be caused by climatic changes.

[86] As it was emphasized by *Thiry* [2000, p. 211], "...sequential changes in the sedimentary clay mineral assemblages with periods of less than 1 Ma cannot be caused by climatic changes. Records of short-term changes in palaeoclimates appear unrealistic; it is probable that only longer sequences are able to reflect palaeoclimatic changes".

Table 11. Clay minerals composition (%) of the Gams section samples

Distance from the K/T boundary, cm	Sample	Smectite (*Sm*)	Illite (*IL*)	Chlorite (*Ch*)	Mineral associations
20	T-4	53.7	39.3	7.0	illite-smectite
14	Q-3	53.0	37.9	9.1	illite-smectite
14	Q-2	47.7	44.2	8.0	illite-smectite
12	P-5/6	62.2	28.8	9.0	illite-smectite
10	O-4/5	36.8	44.7	18.5	illite-smectite
8	N-7/8	45.1	41.5	13.4	illite-smectite
6	M-4	48.1	40.0	12.0	illite-smectite
4	L-6	51.6	38.1	10.3	illite-smectite
2	K-4	11.9	70.5	17.6	Illite
0	J-6	24.3	49.7	26.0	smectite-chlorite-illite
−8	E-F4	69.8	25.2	13.4	illite-smectite
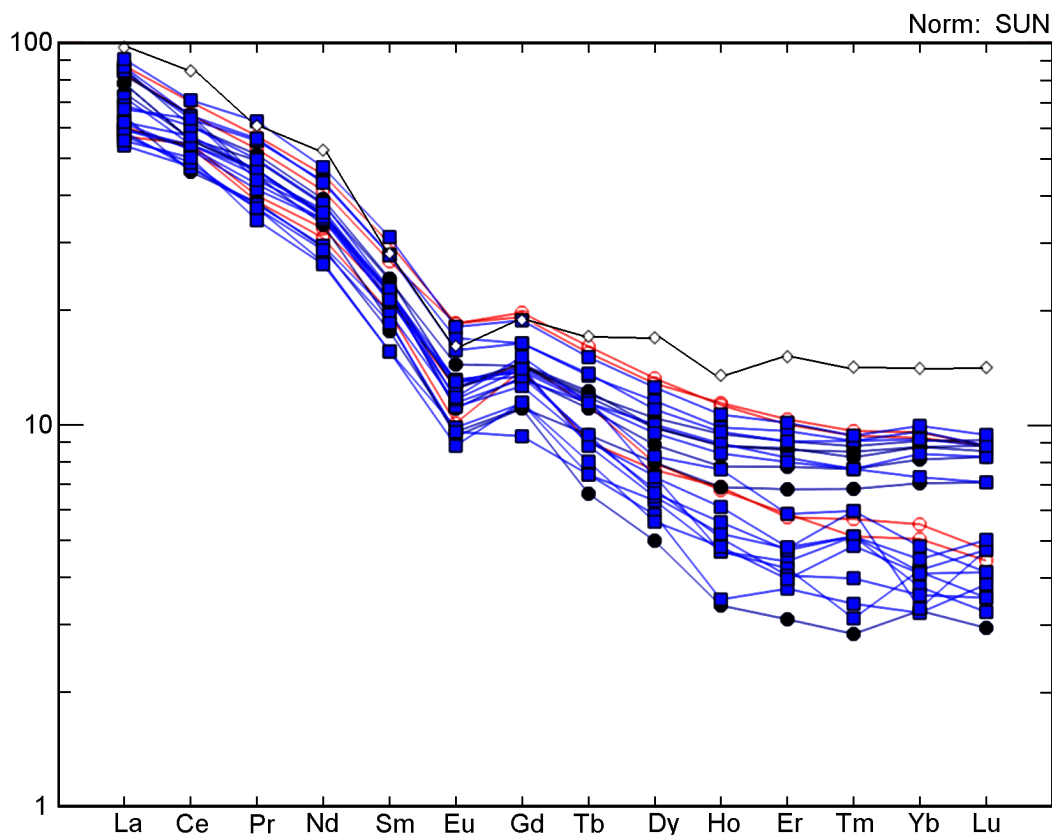
Figure 22. Chondrite–normalized REE pattern for the Gams sections samples. Box filled – samples of the upper portion of section, red open circle – samples of the lower portion of section, black filled circle – layer J, open black circle – NASC.

Isotopic Compositions of Helium, Carbon, and Oxygen

[87] Helium isotopic systematics was studied in samples from transitional layer J, in both whole-rock samples and clayey fractions. As follows from Table 13, the ^{3}He/^{4}He ratio in the whole-rock samples and clayey fractions is also lower than the atmospheric one (1.39×10^{-6}), whereas this value of abyssal oceanic sediments is two orders of magnitude higher [*Krylov et al.*, 1973]. The high ^{3}He/^{4}He ratios of the latter sediments are caused by the addition of extraterrestrial material at an extremely low sedimentation rate. In our samples from layer J of the Gams succession, the fraction of primary solar ^{3}He is very low, because the material of this layer was provided by the erosion of the adjacent source area, whose rocks were enriched in radiogenic He.

[88] As we possessed only very little material, we failed to obtain enough heavy fractions to examine the He isotopic composition of the uppermost part of layer J, which contains beads of metallic Ni and diamond grains (see below). This task will be hopefully accomplished in our further research. It is particularly interesting to study the He isotopic composition of diamond, because the nature of this mineral in transitional layers at the Cretaceous–Paleogene boundary remains obscure as of yet.

[89] The isotopic compositions of carbon $(^{13}C/^{12}C$ or $\delta^{13}C)$ and oxygen $(^{18}O/^{16}O$ or $\delta^{18}O)$ were examined in ma-

Table 12. Clay minerals composition (%) of the J layer

	Layer	Smectite (Sm)	Illite (IL)	Chlorite (Ch)
1	Ja	65.8	31.6	2.5
2	Jb	53.2	36.0	10.8
3	Jc	44.9	51.1	4.0

Table 13. Isotopic ratios and He abundances in the J layer

Sample	Mass, g	^{4}He, ncm^3/g(10^{-6})	^{3}He/^{4}He,10^{-8}
$J2/1$-$2/3$	1.2436	0.81	15.0
$J2/4$+$2/5$+$2/6$	0.8225	1.30	12.0
Ja-c	0.6044	0.25	10.3
Jb	0.5843	0.14	25.0

Note: Temperature of melting 1600°C.
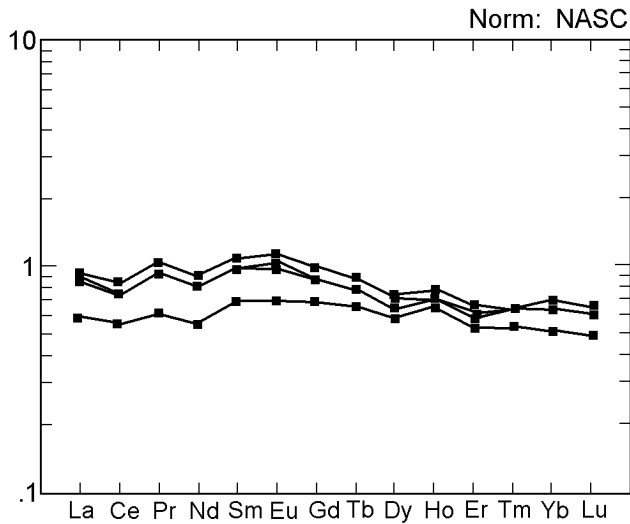
Figure 23. NASC-normalized REE patterns for the upper portion of the Gams sections.
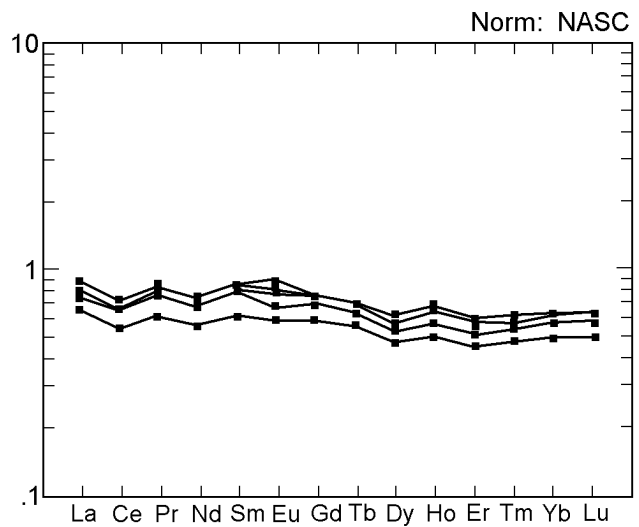
Figure 25. NASC-normalized REE patterns for layer J of the Gams sections.

terial taken at intervals of 2 cm in whole-rock samples from intervals starting 4 cm above to 12 cm above the K/T boundary. Within transitional layer J, sampling sites were spaced 0.4 mm apart (the study of the $\delta^{13}C$ and $\delta^{18}O$ is still not completed) (Table 14).

[90] The distribution of $\delta^{13}C$ in the vertical section is generally controlled by the distribution of the CaO concentrations, and transitional layer J is characterized, as could be expected, by a pronounced minimum in the content of this component (Figure 18) and in $\delta^{13}C$ (Figure 26). The variations in $\delta^{18}O$ in the vertical section reflect the general variations in $\delta^{13}C$ and show a clearly pronounced shift toward

negative values at the K/T boundary, from $5^o/_{oo}$ to $23^o/_{oo}$ PDB $\delta^{18}O$ (Figure 26).

[91] These anomalies in the variations in the carbon and oxygen isotopic composition in the Gams sequence are quite similar to those documented previously elsewhere [*Brinkhuis et al.,* 1998; *Magaritz,* 1989; *Stuben et al.,* 2002; and others]

Table 14. Carbon and oxygen isotope composition of the Gams section samples

Sample	$\delta^{13}C$, $^o/_{oo}$PDB	$\delta^{18}O$, $^o/_{oo}$PDB	$\delta^{18}O$, $^o/_{oo}$SMOW
H2	1.72	−1.98	28.86
H2-2	1.79	−2.03	28.80
I2	1.34	−2.86	27.93
I2-2	1.69	−2.50	28.31
J1A3	−3.52	−22.90	7.11
J1B2	0.41	−4.64	26.09
J1C2	−0.89	−19.49	10.66
J1E1	−1.41	−22.67	7.36
J1E3	0.82	−4.81	25.91
K2	0.69	−3.95	26.80
K2-2	0.32	−4.21	26.53
L5	−1.16	−4.57	26.17
L5-2	−0.31	−4.22	26.53
M5	−1.11	−4.82	25.90
M5-2	−1.97	−5.04	25.67
N3	−1.49	−4.90	25.82
N3-2	−1.17	−4.88	25.84
O3	−1.74	−5.11	25.60
T2	0.86	−3.90	26.85
T2-2	0.77	−3.87	26.89
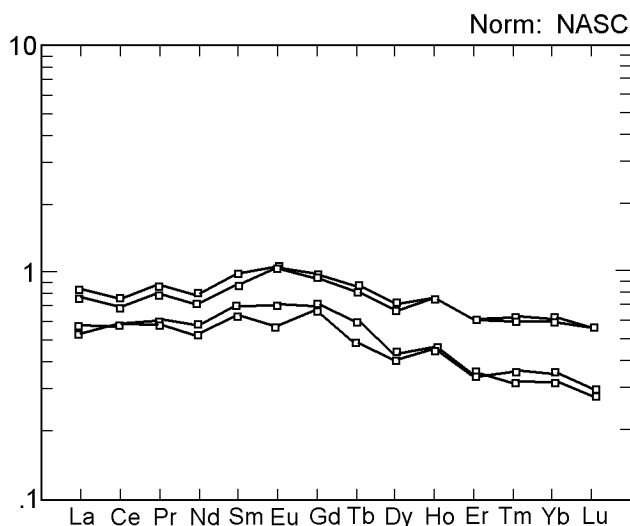
Figure 24. NASC-normalized REE patterns for the lower portion of the Gams sections.

Table 15. Magnetic properties of the Gams section samples

Sample	χ	$A\chi$	$M_{\rm rs}$	$A_{\rm rs}$	$E_{\rm rs}$	$M_{\rm s}$	$M_{\rm p}$	$M_{\rm d}$	$H_{\rm cr}$	$H_{\rm c}$	Texture χ	$M_{\rm rs}$
W9-1	13.37	1.14	124.01	1.31	1.24						I	I
W9-2	16.45		123.09	1.34	1.32	205	33					I
V9-1	12.5	1.08	114.2	1.32	1.31						I	I
V9-2	14.41		111.4	1.24	1.16	179	32					I
U3-1	10.97	1.21	84.99	1.36	1.23						N	N
U3-2	11.14	1.12	78.27	1.31	1.17	372	15		102	20	N	N
U3-3	9.89		75.47	1.28	1.15							N
T3-1	3.49		28.18	1.13	1.05		6				?	N
T3-2	3.78		41.06	1.13	1.11						?	N
T3-3	3.64		22.3	1.1	1.07	50		−12	93	35	?	N
S7-1	3.99		42.21	1.31	1.24						?	N
S7-2	4.15		46.34	1.17	1.17						?	N
R2-1	11.69		39.9	1.19	1.12	206	27		104	17		N
R2-2	11.87	1.08	49.32	1.16	1.11							N
R2-3	11.53	1.02	44.27	1.22	1.11	190	30					I
Q1-1	10.88	1.06	39.11	1.2	1.2						I	I
Q1-2	11.59	1	45.99	1.16	1.16							I
P1-1	12.44	1.02	38.3	1.01	1.01	214	24		106	15	N	N
P1-2	12.33		49.11	1.06	1.06							I
O1-1	12.7		38.17	1.15	1.13	210	25		113	18		I
O1-2	12.55		53.64	1.16	1.12							I
O1-3	12.11	1.03	51.35	1.15	1.09	169	21				N	N
N1-1	12.34		72.36	1.07	1.06						I	I
N1-2	12.34	1.05	63.05	1.18	1.03						I	I
N1-3	12.07	1.1	59.1	1.16	1.12	225	23		118	23	I	I
M1-1	12.05	1.03	50.12	1.19	1.19						I	I
M1-2	11.85		73.68	1.15	0.9	162					I	I
M6-1	12.4	1	74.78	1.02	0.99		32					N
L1-1	10.33		72.3	1.16	1.04	309	31		113	19		N
L2-1	11.16	1.07	69.4	1.17	1.07	256	26		129	27	I	I
L8-1	13.35	1.02	69.81	1.2	1.19							N
L8-2	13.23		62.09	1.21	1.08							N
K2-1	4.31	1.22	30.03	1.08	1.08						?	N
K2-2	4.02	1.09	34.68	1.01	1.01	53					?	N
K2-3	4.37		40.87	1.05	1.03						?	N
K2-4	5.3		47.6	1.09	0.93	129		−1.3	91	35	?	N
J7-1	15.44	1.03	41.53	1.02	0.98							N
J7-2	15.71		42.05	1.14	1.09							N
J3-1	15.48	1.04	67.6			165	26		68	11		
J3-2	15.96		31.7	1.31	1.29		34					N
J4-1	15.64		39.1	1.31	1.3	156	31		66	13		N
J4-2	15.58		30.2	1.31	1.27	201	36		51	9		N
J5-1	15.12	1.04	40.67	1.29	1.19							N
J5-2	15.54		41.88	1.28	1.24							N
I4-1	6.65	1.04	22.92	1.16	1.13	79					I	I
I4-2	5.68	1.01	19.5	1.13	1.07							I
I4-3	5.58											
H4-1	5.78		21.88	1.06	1							N
H4-2	5.05		7.76	1.09		36		−1.4	76	16		N
H6-1	4.98		8.71	1.2	0.96							N
H6-2	5.14	1.02	9.71	1.19	0.99						N	N
H6-3	5.12		9.38	1.07	0.98							N

Table 15. Continued

Sample	χ	$A\chi$	M_{rs}	A_{rs}	E_{rs}	M_s	M_p	M_d	H_{cr}	H_c	Texture χ	Texture M_{rs}
G3-1	5.05		9.44	1.24	0.84							N
G3-2	4.87		9.29	1.15	1.01							N
G3-3	4.9		8.49	1.18	1	73						N
G6-1	5.19	1.01	9.68	1.2	1.06							N
G6-2	5.1		8.9	1.22	1.04							N
G6-3	4.97		7.54	1.18	1.08	55	1		98	13		N
F6-1	4.74		8.85	1.22	1.04							N
F6-2	4.68		8.89	1.24	1.04	66						N
F6-3	4.7	1.03	8.8	1.2	1.02							N
E6-1	4.64		7.24	1.22	1.03	68		−2	93	16		N
E6-2	4.63		9.51	1.19	1.03							N
E6-3	4.62	1.02	9.78	1.15	1							N
D6-1	4.8		11.32	1.14	1	92		−2	78	12		N
D6-2	4.93		14.34	1.13	1.03							N
D6-3	4.19	1.03	12.44	1.15	1.03							N
C6-1	5.23		13.48	1.17	0.98	73		−2	102	18		N
C6-2	4.96	1.03	20.14	1.18	0.99							N
C6-3	5.02		21.45	1.15	1.05							N
B6-1	4.06	1.02	17.02	1.13	0.98							N
B6-2	3.93		17.2	1.17	0.95							N
B6-3	4.18		12.26	1.17	1.02	48	2.5		95	28		N
A6-1	4.87		16.71	1.22	1.14	65						N
A6-2	4.62		15.99	1.12	1.04							N
A6-3	4.84		18.03	1.09	1.05							N
A6-4	4.76		18.41	1.17	1.13							N
A6-5	4.8		16.31	1.23	1.09							N

Note: Sample – number of sample; χ – specific magnetic susceptibility, $10^{-8}\,\mathrm{m^3\ kg^{-1}}$; $A\chi = \chi_{max}/\chi_{min}$ – anisotropy of magnetic susceptibility; M_{rs} – specific saturation remanent magnetization, $10^{-5}\,\mathrm{Am^2\ kg^{-1}}$; $A_{rs} = M_{rs\,max}/M_{rs\,min}$ – anisotropy of saturation remanent magnetization; $E_{rs} = M_{rs\,in}M_{rs\,in}/M_{rs\,max}M_{rs\,min}$ – magnetic fabric; M_s – specific saturation magnetization, $10^{-5}\,\mathrm{Am^2\ kg^{-1}}$; M_p – paramagnetic magnetization, $10^{-5}\,\mathrm{Am^2\ kg^{-1}}$; M_d – diamagnetic magnetization, $10^{-5}\,\mathrm{Am^2\ kg^{-1}}$; H_{cr} – remanent coercive force, mT; H_c – coercive force, mT; Texture – inversion (I) and normal (N) fabric.

and resemble most closely the sequences at El Kef in Tunisia and Agost in SW Spain [*Keller et al.,* 1996; *Rodrigues-Tovar et al.,* 2004]. The variations in the temperature cannot be evaluated until the isotopic compositions of the foraminifers is determined.

Petromagnetic Measurements

[92] **The specific magnetic susceptibility (χ), specific saturation magnetization (M_s), and the specific remanent saturation magnetization (M_{rs})** vary within broad limits (Table 15) depending on the lithological characteristics of the rocks, first of all, their concentration of carbonate material. A positive correlation between M_s and M_{rs} testifies to the determining role of the concentration of magnetic minerals. The correlations of M_s and M_{rs} with the magnetic susceptibility χ are less clear.

[93] **Thermomagnetic data.** The analysis of the $M(T)$ curves allowed us to identify six magnetic phases (Figure 27):

[94] (1) $T_c = 90$–$150°C$, the fraction of this phase M_s is equal to 10–20%, and it is contained in all of the examined samples and corresponds to ferromagnetic iron hydroxides, such as goethite. Assuming that this is goethite with $M_s = 0.02\ \mathrm{Am^2\ kg^{-1}}$, the concentration of this goethite in the sequence was estimated as ranging from 0.5% in its lower part to 2–2.5% in the upper part of section (Figure 28a).

[95] (2) $T_c = 180$–$300°C$, this phase is present in all of the samples. The contribution of this phase to M_s is equal to 5–40%. After heating to $800°C$, the percentage of this phase in many samples notably increases (to 30–90%), and the Curie point usually decreases. Judging from the increase in M_s at decreasing T_c, this phase is hemoilmenite, which partly homogenizes during heating, and, consequently, its $M_s(T)$ curve becomes concave. The check heating of some samples to $1000°C$ indicates that the $M_s(T)$ curve ceases to be concave, and the M_s notably increases compared with that at heating to $800°C$. This corresponds to the diagram of state of hemoilmenite of intermediate composition, which is homogeneous at temperatures above $900°C$ [*Nagata,* 1965]. The concentration of hemoilmenite is determined from the results of the second heating (it is read from the T_c vs. hemoilmenite
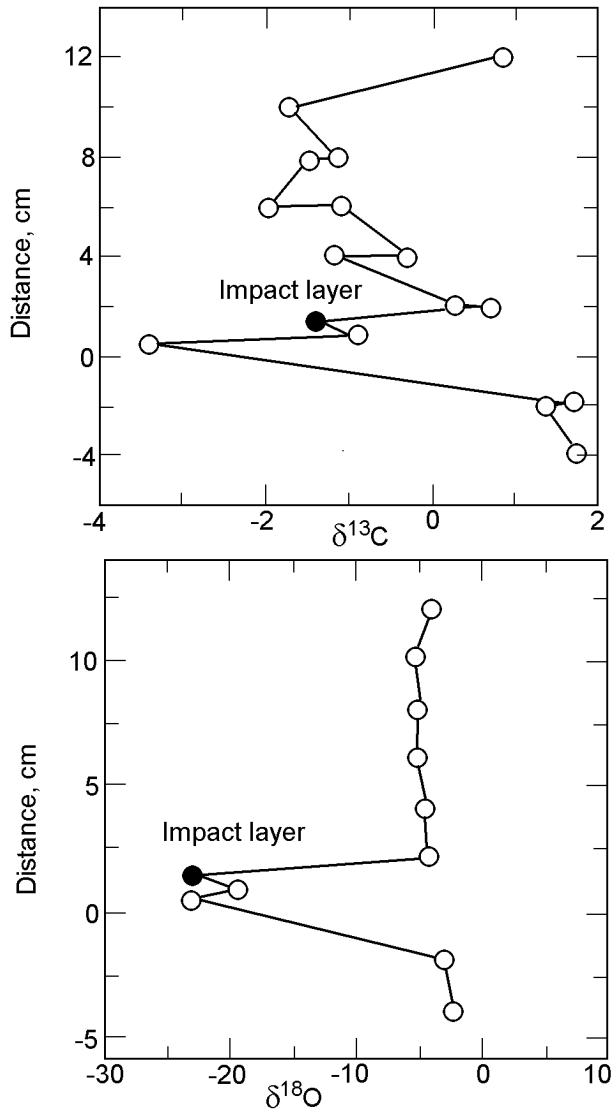
Figure 26. Variations of $\delta^{13}C$ and $\delta^{18}O$ values at the Gams section samples.

composition diagram from [*Nagata,* 1965]). This concentration varies from less than 0.0001% to 0.02% (Figure 28b).

[96] (3) $T_c = 350$–$360°C$ was encountered only in sample from layer J during the thermomagnetic analysis of the

$M_r(T)$ curves (which testifies that the material contains metallic Ni), but not the $M(T)$ curves. These results suggest that Ni occurs in the form of very small grains, whose concentration is likely below 0.0001% and which are unevenly distributed in layer J.

[97] (4) $T_c = 550$–$610°C$ was identified in all of the samples, and the fraction of this phase M_s ranges from 20% to 60% (Figure 5). This is most probably predominantly titanomagnetite, which is heterogeneously oxidized to magnetite. The latter is, in places, also homogeneously oxidized ($T_c > 580°$ C). The presence of titanomagnetite was confirmed by microprobe analyses: the composition of the grains is identical to those of titanomagnetite from basalts (they contain $\sim$20–25% TiO_2) (Table 16). When heated, titanomagnetite grains partly homogenize. The approximate concentration of titanomagnetite and magnetite in the samples varies from <0.0001% to 0.001% (Figure 28c).

[98] (5) $T_c = 640$–$660°C$ was found only in samples from layer J. The contribution of this phase to M_s equals 10–15%. As samples from layer J contain Ni, it can be suggested that this phase is a Ni–Fe alloy. A simple calculation based on the T_c and M_s values indicates that this can be a phase of the composition Fe_3Ni.

[99] (6) $T_c = 740$–$770°C$ was identified in eleven samples, the fraction of this phase in M_s is 10–30%. Upon heating to $800°C$, this phase partly or completely disappears. This is metallic Fe with minor admixtures, which oxidizes when heated to $800°C$. Its concentration is less than 0.0006%. Practically no metallic Fe was identified in layer J, but it contains a Fe–Ni alloy with $T_c = 650$–$660°C$, whose concentration does not exceed 0.0002%. The distribution of Fe in the vertical section is quite homogeneous (Figure 28d).

[100] After heating to $800°C$, half of the samples appear to contain hematite, which is produced by magnetite oxidation and the dehydration of iron hydroxides.

[101] **Coercivity of magnetic minerals KC.** The assemblage of magnetic phases is similar in all of the samples and slightly differs in the carbonate rocks from the bottom part of the sequence and clayey rocks from its upper part. The KC values are the most similar in the Maastrichtian rocks, which are, in turn, closely similar to the Danian layers $K, S,$ and T.

[102] Beginning with unit L, the KC gradually increases to the limiting field of measurements of 800 mT (Table 15) and farther up gradually changes: from sample from unit M

Table 16. Electron microprobe analyses (wt. %) of iron-titanium oxide minerals in the Gams section

	Layer $J6$-1			Layer $J6$-2		Layer $J6$-3		Layer $J6$-4	
Oxides	Tm	Tm	Ilm	Tm	Ilm	Mt	Ilm	Mt	Ilm
TiO_2	23.00	20.80	46.10	22.20	45.20	0.00	46.90	0.00	45.60
FeO^*	72.20	74.90	52.20	73.10	53.20	93.10	52.10	92.90	53.70
MgO	0.10	0.10	0.60	0.20	0.30	0.10	0.30	0.40	0.30
MnO	0.10	0.20	0.10	0.20	0.10	0.20	0.10	0.10	0.10
Cr_2O_3	0.00	0.00	0.00	0.10	0.10	0.10	0.10	0.00	0.00
Al_2O_3	0.10	0.20	0.10	0.10	0.10	0.10	0.10	0.40	0.20
Total	96.50	96.20	99.10	95.90	98.90	93.60	98.90	93.80	99.00
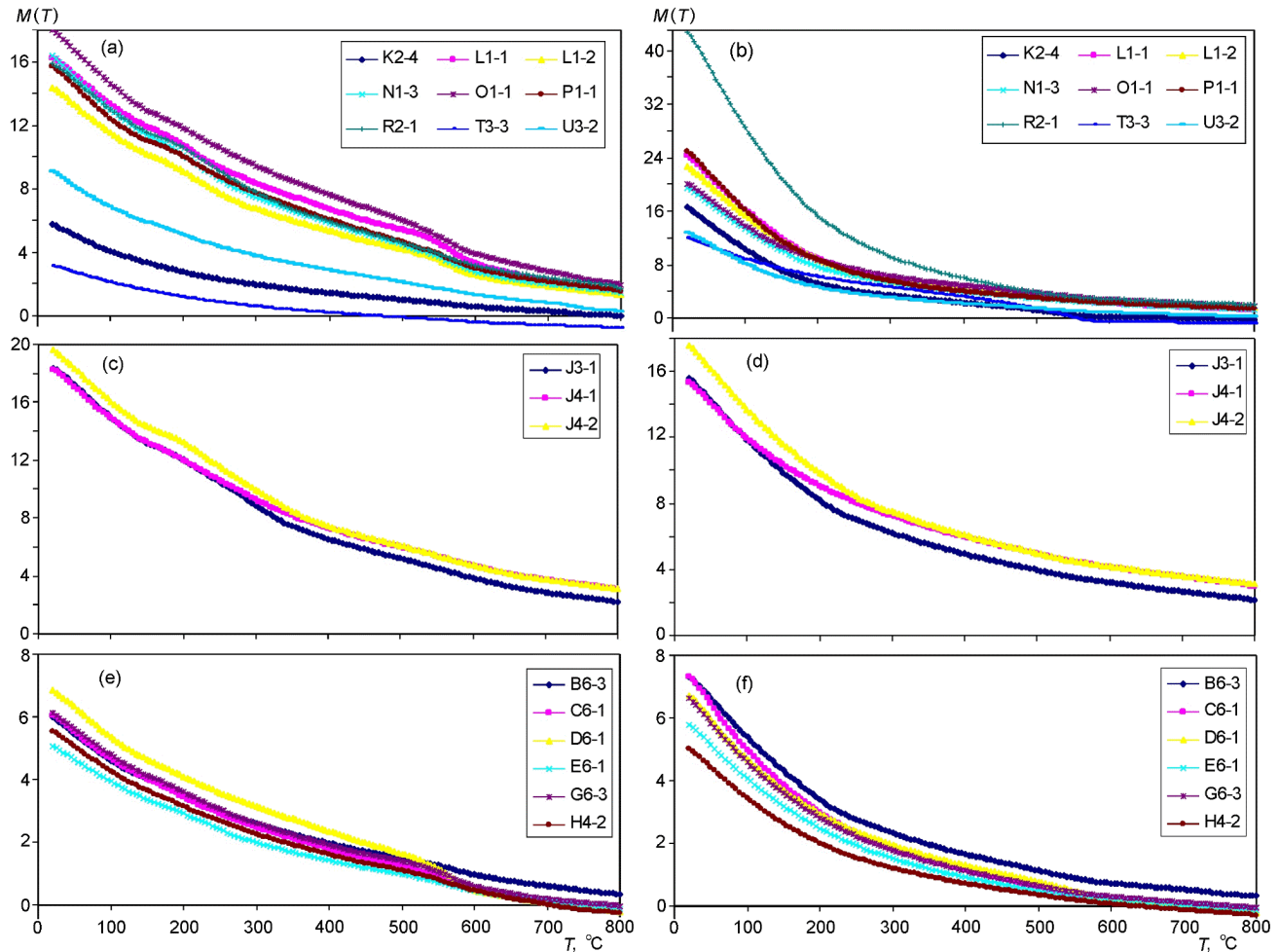
Figure 27. Thermomagnetic analysis of induced magnetization $M(T)$. a, c, e – the first heating; b, d, f – the second heating.

to those from S and T, the curve first shows a plateau and then a clearly pronounced maximum at 130–160 mT and a minimum at ∼400 mT.

[103] The coercivity KC of layer J is principally different in its low-coercive field in having a maximum or a plateau at 25–40 mT. In the rest of it, the KC of layer J is similar to those of samples from units N and O. The changes in the coercivity in layer J is also seen from the behavior of the H_{cr} (Table 15).

[104] Judging from the values of H_{cr} and M_{rs}/M_s (Table 15), the rocks are dominated by single-domain and pseudosingle-domain grains. The low coercivity of magnetic grains in layer J is not reflected in M_{rs}/M_s or H_{cr}/H_c (thus highlighting the absence of relations with the sizes of magnetic grains) but rather results from the presence of Ni and its alloys with Fe.

[105] There are no correlations of such characteristics of the coercivity spectra as the position and heights of the major extrema with the Fe concentrations, a fact that can be explained only by a low contents of this phase. The weakly pronounced correlation for goethite is presumably explained

by the occurrence of a complicated assemblage of iron hydroxides in sedimentary rocks. The contents of magnetite and hemoilmenite are related through a weak positive correlation. This implies that the coercivity spectra of the rocks are determined mostly by the presence of magnetite and hemoilmenite grains. In addition to these minerals, layer J (its low-coercivity part) contains grains of metallic Ni and its alloy with Fe.

[106]   **Anisotropy.** We measured the anisotropy of magnetic susceptibility (A_k) and remanent saturation magnetization (A_{rs}). The former is a characteristic of all minerals, magnetic, paramagnetic, and diamagnetic, while the latter is typical only of magnetic minerals. In general, both types of anisotropy behave similarly (with rare exceptions, see Table 15). The values of A_k of the main group of samples range from 1 to 1.1 and increase to >1.1 only in four samples, whereas the values of A_{rs} of most samples lie within range of 1.12–1.36 and decrease to $A_k \leq 1.1$ only in four samples. The likely reason for this is that the paramagnetic and diamagnetic constituents of sediments are generally isotropic, although calcite and clay minerals are anisotropic (A_k is
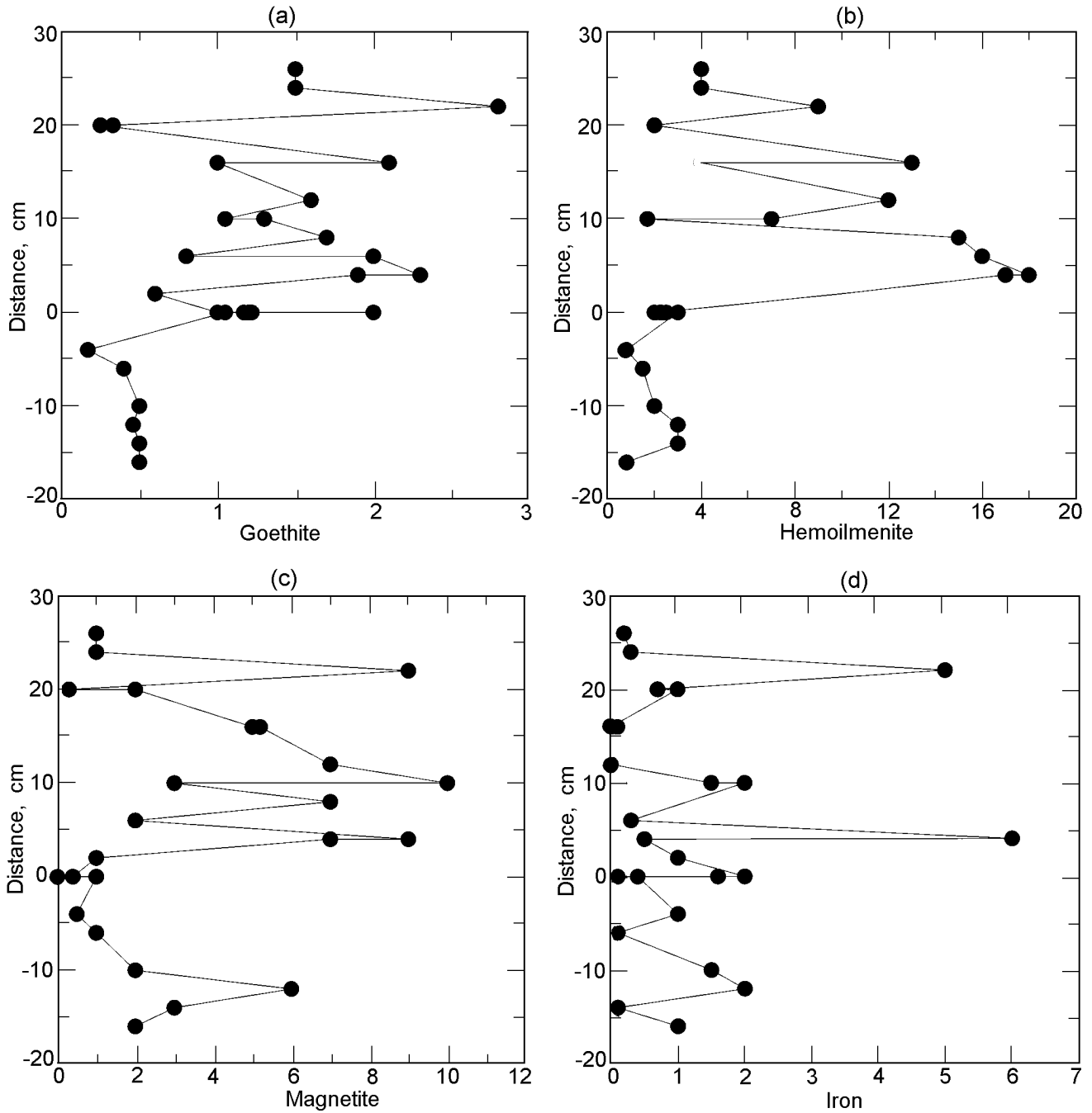
Figure 28. Magnetic minerals concentration for the Gams section samples: a – goethite, (%), b – hemoilmenite, $(10^{-3}$ %), c – magnetite, $(10^{-4}$ %); d – iron, $(10^{-4}$ %).

equal to 1.13 for calcite and 1.2–1.35 for clays [*Rochette et al.,* 1992]), and the distribution of their symmetry axes is close to the matrix one.

[107] In terms of A_{rs}, virtually all of the sediments (with rare exceptions: layers K and T) are anisotropic, and this anisotropy is only insignificantly dependent on the rock composition. From units A to R, A_{rs} varies within a narrow range and notably increases in the upper part of the sequence, in units U–W. Within individual units, A_{rs} varies

insignificantly. The exception is clay layer J, whose anisotropy shows the greatest scatter: from 1.02 to 1.32.

[108] Most of the sediments are characterized by a foliation magnetic fabric, $E > 1$, and only occasional layers have either $E \sim 1$ or very weak linearity ($E < 1$ (Table 15). The aforementioned features can be explained by the presence of elongated grains of magnetic minerals, the compaction of the sediments, some structuring of the sediments under the effect of flows and currents, etc. The occurrence of anisotropy and

foliation testifies that the magnetic minerals (which are the major causes of the magnetization of the rocks) are of terrigenous nature. Conceivably, isotropic samples from units K and T contain authigenic magnetic minerals.

[109]   **Variations in magnetic characteristics in the vertical section.**   The vertical section of the rocks displays two levels of χ, M_{rs}, and M_s: Maastrichtian calcareous marls and Danian clays, which include layers K, S, and T (Table 15). The occurrence of these levels is confirmed by the distribution of magnetite, hemoilmenite, and goethite in the vertical section and the absence of any systematic trend in the distribution of metallic iron (Figure 28). A notable differences between the vertical distributions of χ, on the one hand, and M_{rs} and M_s, on the other, seem to be controlled by the significant contribution of paramagnetic material and, most significantly, tiny superparamagnetic grains, to the susceptibility.

[110] Layer J does not differ from other layers in the content of magnetic minerals (Figure 28) but has obviously lower coercivity (Table 15). The latter fact is likely explained by the presence of Ni and Fe–Ni alloy. The distributions of magnetite, hemoilmenite, and "goethite" in the vertical section are generally similar. These minerals seem to have been accumulated simultaneously, under lithological control, without any relation to the Cretaceous–Paleogene boundary.

Characteristics of Transitional Layer J at the K/T Boundary Derived from the Results of Thermomagnetic and Microprobe Analysis

[111] Thermomagnetic analysis (TMA) was carried out in samples 1–10 mm^3 in volume, and minerals for microprobe analysis (MPA) were separated from 100–200 mm^3 of the material. TMA was originally conducted on a series of samples taken in different parts of layer J. Then one of the samples, sample $J6$, was divided into six units (Figure 4), and each of them was subjected to TMA. Simultaneously, magnetic minerals for MPA were separated from each of the units by using a powerful permanent magnet. The sizes of the separated mineral particles ranged from a submicrons to tens of microns. The characteristics of layer J are described in detail below (they are listed in order from the bottom to the top).

[112]   **Sample J-1.**   According to TMA data, this sample contains notable amounts of titanomagnetite with $T_c = 540°C$ (Figure 29a), and this is confirmed by MPA data, which point to the presence of titanomagnetite and ilmenite, sometimes in aggregates. The composition of TM grains (Table 15) does not correspond to the Curie point, a fact testifying to the heterogeneous alteration of TM grains (their oxidation and decomposition). The grains are small and oxidize and disappear when heated (as can be inferred from the drastic drop in the magnetization value at heating to >700°C) and partly homogenize (the Curie point shifts to the left to 510°C after the first heating of the sample, which

also results in a decease in the magnetization). A small bend on the curve at 300°C that disappears after the second heating is likely caused by maghemite, which is transformed into hematite at this temperature. Its fraction relative to the titanomagnetite content is approximately 10%.

[113]   **Sample J-2.**   Judging by the TMA data, the samples contains (a) maghemite, (b) magnetite with $T_c \sim 570°$ C, and, perhaps, also (c) metallic iron (Figure 29b). The sample was "underheated", and it was thus difficult to definitely determine whether it contained iron, but an iron spherule was identified under the microprobe[1]. The sample is very weakly magnetic, and a notable contribution to its magnetization is made by paramagnetic material. We failed to separate titanomagnetite and magnetite grains from the clayey material of this layer. Compared with sample J-1, this sample contains approximately 20 times less magnetic minerals.

[114]   **Sample J-3.**   The TMA data on this sample are similar to those on sample J-1 and suggest the presence of titanomagnetite, whose $T_c \sim 500°$ C and shifts to 480°C as a result of the partial homogenization of the mineral, and the magnetization dramatically drops (Figure 29c). In addition to titanomagnetite, the rock contains magnetite with $T_c = 590°C$. This sample differs from sample J-1 in having much lower (by more than one order of magnitude) concentrations of magnetic minerals, and the horizontal segment of the curve more probably testifies to the absence of metallic iron. One particle of magnetite and one of ilmenite were found in this sample under a microprobe (both of them are no larger than 10 μm), along with numerous minute grains of supposedly magnetite.

[115]   **Sample J-4.**   Judging from the TMA data, this sample contains (a) maghemite (the curve shows a bend corresponding to the maghemite–hematite transition), (b) metallic Ni ($T_c = 350°C$), (c) magnetite ($T_c = 590°C$), and (d) iron ($T_c > 730°$ C, determined by an extrapolation). Ni is the predominant phase. The total content of magnetic minerals is roughly 15 times lower than in sample J-1 (Figure 29d).

[116]   **Sample J-5.**   According to TMA data (Figure 29e), the sample contains (a) maghemite (bend on the curve at 170–300°C), (b) magnetite with $T_c = 590°C$, (c) "hemoilmenite" with $T_c = 300°C$ (concave curves of the second and third heating), and (d) iron (?) with $T_c \sim 700$–$750°C$ (extrapolation). Three small Ni grains with awaruite were found in the magnetic fraction by microprobe analyses (Figures 30).

[117]   **Sample J-6.**   Ni with $T_c = 350°C$ was found in this sample (as the predominant phase) by MTA and was confirmed by MPA (Figure 29f). This richness of the rock in Ni is of local character and was not detected in any other samples from layer J.

[118] In general, the results of MPA and TMA contribute each other, and their analysis led us to the following conclusions:

---

[1]The similar iron spherule was found in unit M.
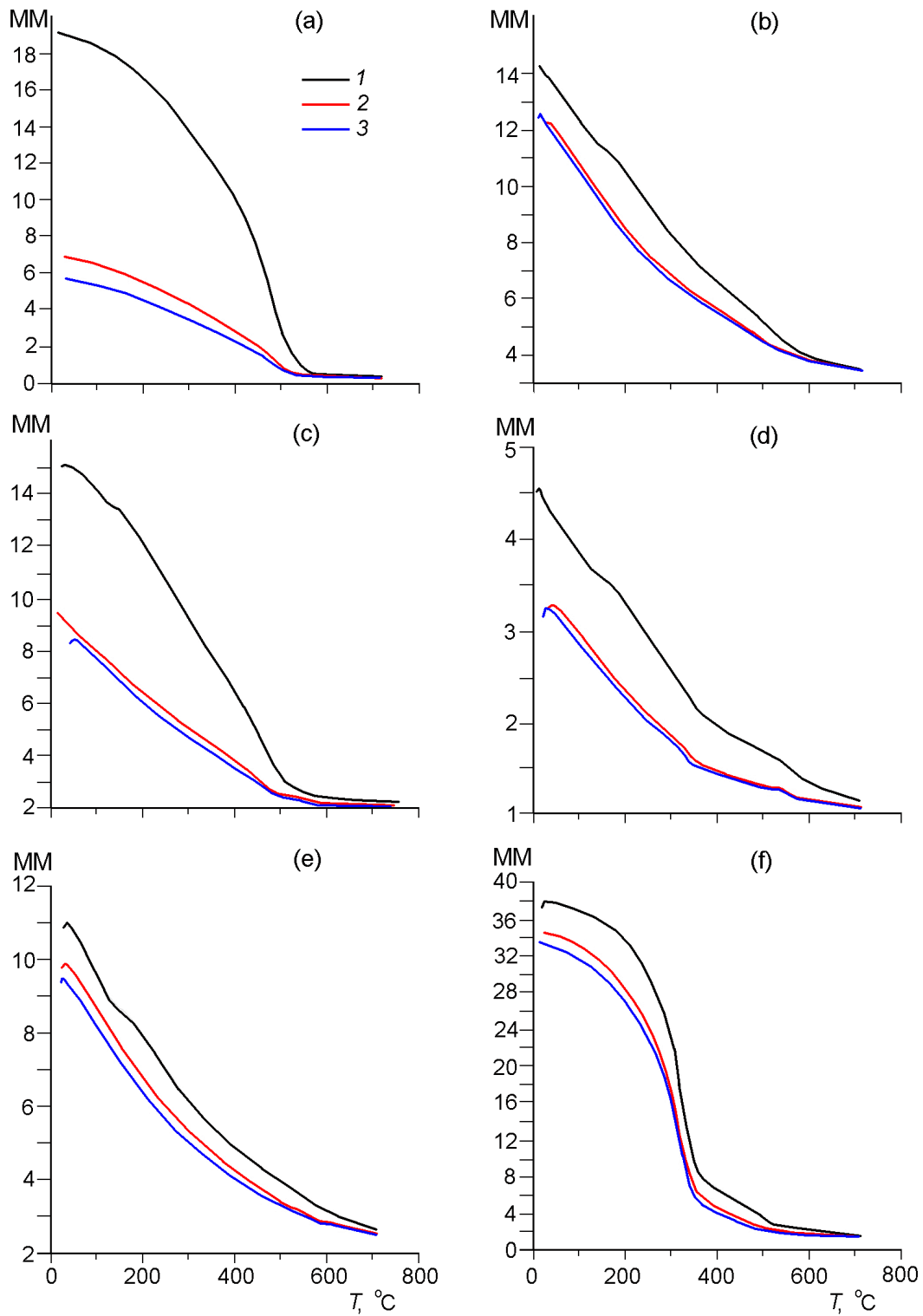
Figure 29. Thermomagnetic analysis of layer J: a – unit $J1$, b – unit $J2$, c – unit $J3$, d – unit $J4$, e – unit $J5$, f – unit $J6$. The first heating – black line (1), the second heating – red line (2), the third heating – dark blue line (3). MM – magnetic moment, 10^{-5} Am^2.
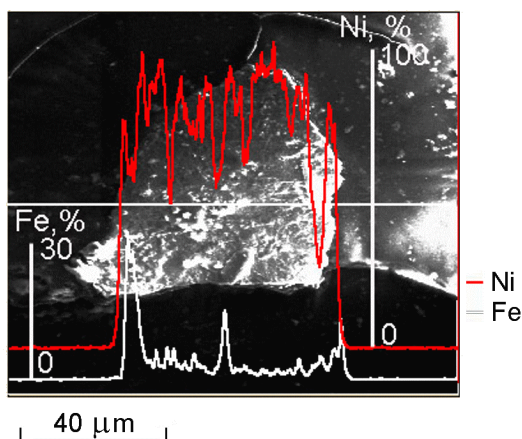
Figure 30. Awaruite grain in the unit $J5$.

Figure 31. SEM image of Au in unit J-6/2.

[119] The lower part of layer J (unit $J1$) is slightly enriched in titanomagnetite and ilmenite, which have compositions typical of these minerals from basalts. It can be concluded that this layer provides record of the deposition of volcanic particles, when the largest particles had been already settled, and the settling process gradually attenuated. No titanomagnetite was found in higher units $J4$ and $J5$, but Ni appears in the rocks starting from layer $J4$. It appears in aggregates with awaruite (Figure 30) and in unit $J5$ and as metallic spherules of practically pure Ni in unit $J6$.

[120] The distribution of Ni particles within layer J is extremely uneven: single particles start to appear in unit $J4$, and the amount of the particles reaches a maximum in the uppermost part of layer J (numerous Ni beads were found in unit $J6$), with this enrichment in Ni detected only in one sample. The Ni beads range from a submicrons to tens of microns.

[121] Finally, the mineralogical analysis of the heavy fraction from sample $J2$ has revealed single platelets of copper. The microprobe study of these particles confirms that they contain not only pure Cu but also particles with up to 30% Au and 1–2% Ni (Figure 31). The morphology of these particles is unusual (Figure 21).

Nickel Spherules and Diamond Grains as Indicators of an Impact Event

[122] The detailed examination of layer J (its uppermost, very thin sedimentary unit $J6$, whose thickness does not exceed 200 μm) has revealed Ni beads and diamond grains (Tables 17, 18). A layer fragment 1 cm^2 in area separated from a stone cube contained tens of diamond grains (ranging from a submicrons to tens of microns) and hundreds of Ni spherules whose sizes also ranged from a submicrons to tens

Table 17. Electron microprobe analyses (at. %) of Ni globules in layer $J6$

Element	globule 1	globule 2	globule 3
O	6.76	8.66	9.31
Na	0.00	–	–
Mg	0.25	–	0.16
Al	0.61	–	1.04
Si	1.23	1.19	0.95
P	0.11	–	–
S	0.00	–	0.02
Cl	0.11	0.55	0.04
K	0.02	–	0.02
Ca	0.13	0.46	0.09
Ti	0.11	0.43	0.07
Cr	0.01	–	0.00
Mn	0.00	–	0.03
Fe	0.23	–	0.35
Co	0.02	–	0.07
Ni	90.41	88.71	87.85

Table 18. Electron microprobe analyses (at. %) of diamonds in the layer $J6$

Element	Diamond 1	Diamond 2
C	93.61	89.91
O	6.26	9.38
Al	–	0.04
Si	0.13	0.14
Cl	–	0.13
Ca	–	0.03
Ti	–	0.03
Mn	–	0.05
Ni	–	0.30
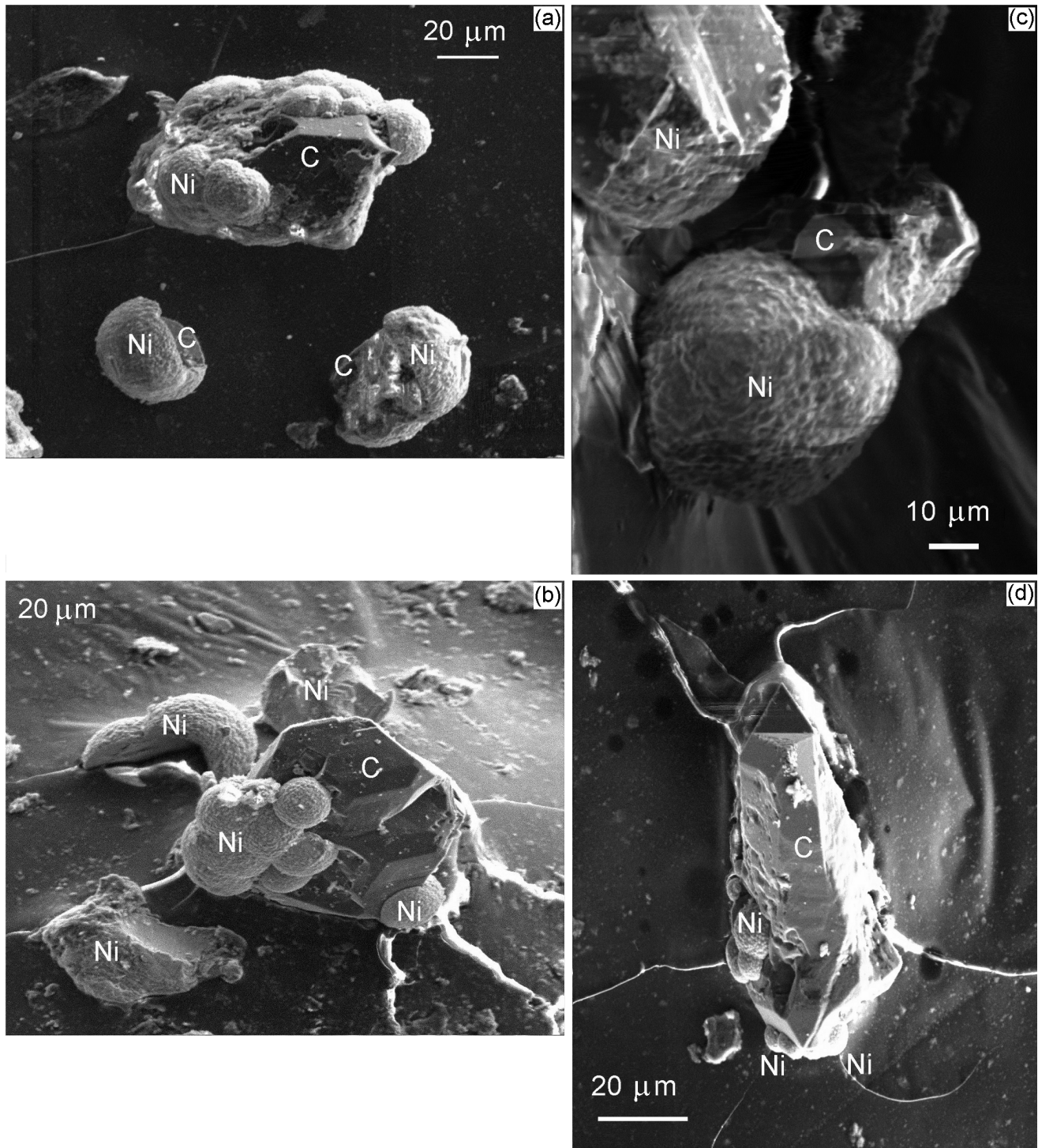
Figure 32. SEM images of Ni bubbles and diamonds in the unit *J*-6/6 (see explanation in text).

of microns. Diamond grains and Ni beads of the most typical morphology were examined under a microprobe.

[123] The MPA of Ni beads was conducted on two microprobes (one equipped with WDS and the other with EDS) and have demonstrated that the Ni beads consist of practically pure Ni with a thin outermost film of NiO (Table 17). The surface of all Ni beads is covered with euhedral crystals, which have sizes of 1–2 μm. Such pure Ni in the form

of beads, whose surface is lined with crystals has never been found either in magmatic rocks or meteorites, in which Ni always contains significant admixtures.

[124] The examination of Ni beads and diamond crystals from unit $J6$ have determined the following modes of their joint occurrence: a – diamond crystals included in Ni spherules (Figure 32a); b – Ni beads sticking to a diamond crystal (Figure 32b). This micrograph also displays individual Ni beads with contact surfaces with diamond and Ni aggregates of unusual shape, which resembles pillow lava (upper top quadrant in Figure 32b); c – Ni bead with traces of its contact with diamond (Figure 32c); d – Ni spherules on a large prismatic diamond (or, perhaps, lonsdaleite) crystal (Figure 32d).

Discussion

[125] The Gams stratigraphic sequence is characterized by a clearly pronounced transitional layer at this boundary, with this layer characterized by pronounced compositional differences from the over- and underlying rocks. The major- and trace-element composition of the rocks display correlations between the variations in the contents of certain elements in the vertical section.

[126] 1. The lower part (units $C - I$) has a low concentration of SiO_2, Al_2O_3, and K_2O at a high content of CaO. In transitional layer J, the concentrations of SiO_2, Al_2O_3, and K_2O dramatically increase, and the contents of CaO and MnO decrease. The transition to the upper part of the sequence occurs through intermediate layer K, whose concentrations of Al_2O_3, Fe_2O_3, CaO, Na_2O, and K_2O differ from those in both the underlying and the overlying rocks. Although the upper part of the sequence (units $L-U$, except layers S and T) shows significant variations in the bulk-rock chemical composition, its content of the terrigenous constituent (quartz and feldspathoids) drastically increases.

[127] The extent of the variations in the lower part (below layer J) significantly differ from that in the upper part, which includes a number of units with anomalous concentrations of siderophile, chalcophile (Zn, Cu, Ni), and some other elements. These variations in the upper part of the sequence were caused by unstable conditions in the source area of the sediments.

[128] The variations in the concentrations of lithophile (Cr, V, Rb, Cs, Ba, Sr, Nb, and Zr), chalcophile (Cu, Zn, and Ga), and siderophile (Co, NI, and Mo) elements demonstrate that the most significant and mutually correlated variations occur in the vicinity of boundary layer J. A remarkable compositional feature of this layer is its elevated contents of K_2O, Al_2O_3, Fe_2O_3, and TiO_2 at a very low concentration of CaO.

[129] 2. The more detailed study of the composition of layer J has revealed that, having a fairly high concentration of clay minerals, this layer has a ratio of clay to non-clay mineral increasing upward in its vertical section. In the lower part of layer J, the fraction of smectite is equal to 60% and systematically decreases upsection, whereas the frac-

tion of illite simultaneously increases by 20%. Taking into account that this layer was detected to contain titanomagnetite of composition corresponding to that of this mineral from basalts, it is reasonable to conclude that the smectite developed after volcanic material. It should be emphasized that the Ir concentration also increases from 5 ppb to 9 ppb in the direction from unit $J1$ to $J4$ and then decreases to 3 ppm in $J5 - J6$. The concentrations of As, Ag, Au, and Br change simultaneously with it.

[130] 3. Our detailed magnetological, magneto-mineralogical, and microprobe examination of the Gams sequence have revealed the following tendencies important for understanding the nature of transitional layer J at the K/T boundary:

[131] The lower part of the layer J (unit $J1$) contains notable amounts of titanomagnetite, whose composition is identical to that of titanomagnetite from basalts (the mineral contains $\sim$20–25% TiO_2). The rocks above unit $J4$ contain nickel, iron, and iron–nickel alloy, whose composition is similar to that of awaruite (Fe_3Ni) and whose amount reaches a maximum in unit $J6$. The same unit contains beads of metallic Ni. The comparison of the TMA and MPA data reveals the extremely heterogeneous character of the distribution of Ni, Fe, and their alloy in layer J.

[132] Our microprobe studies indicate that the Ni beads consist of practically pure Ni with an outermost film of NiO. Such pure Ni in the form of spherules with a highly crystalline surface has never been found in magmatic rocks or meteorites, whose Ni always contains significant admixtures of other elements. The characteristic structure of the surface of the Ni beads could be produced during the fall of an asteroid (or meteorite), which resulted in the release of energy sufficient not only for the melting of the projectile (asteroid) itself but also for its evaporation. Metal vapors could be lifted by the explosion to a significant altitude (perhaps, to tens of kilometers) and crystallized there.

[133] During the detailed study of layer J (in its uppermost, very thin sedimentary unit $J6$, whose thickness is not more than 200 μm), we detected not only Ni spherules but also diamond grains. Their number was close to a few dozen, and they ranged from a submicrons to a few microns in size, whereas the number of the Ni spherules amounted to a few hundreds.

[134] The diamond crystals could be formed in the same vapor nebula, during its subsequent cooling. Synthetic diamond is produced by the method of spontaneous crystallization of a carbon solution in a metallic (Fe, Ni) melt above the diamond–graphite equilibrium line. The diamond is obtained in the form of single crystals, twins, polycrystalline aggregates, skeletal crystals, acicular crystals, and anhedral grains [*Bokii et al.,* 1986]. Practically all of the aforementioned typomorphic features of diamond crystals were also identified in our sample.

[135] This led us to conclude that the processes of diamond crystallization were similar in the nebula of nickel–carbon vapor during its cooling and during spontaneous crystallization from a carbon solution in nickel melt in experiments. However, the nature of the diamond can be completely elucidated only after its detailed isotopic studying, which will require a significant amount of the material.

[136] Finally, the mineralogical analysis of the heavy fraction from unit $J2$ have revealed a few platelets of copper. The microprobe examination of these particles indicated that they consisted not only of pure Cu but also of particles with up to 30% Au and 1–2% Ni. The morphology of these particles is very unusual, they have uneven ragged edges.

[137] Shocked quartz, coesite, and stishovite (minerals serving as indicators of an impact event), as well as spinel with a high Ni concentration, found in boundary layers at the K/T boundary elsewhere [*Leroux et al.,* 1995; *Preisinger et al.,* 1986, 2002] were not detected in the upper part of layer J in the Gams sequence (which does not mean, however, that these minerals are absent in this layer).

[138] The variations in $\delta^{18}O$ and $\delta^{13}C$ in the vertical section show a pronounced shift toward negative values at the K/T boundary, from $5^o/_{oo}$ to $23^o/_{oo}$ PDB for $\delta^{18}O$. It is important to emphasize that the minimum $\delta^{18}O$ and $\delta^{13}C$ values are characteristic of the units of layer J occurring below the unit corresponding to the impact event (samples J-6/3 and J-6/4). The most remarkable fact is that no microfauna was found in these units. These anomalies in the variations of the carbon and oxygen isotopic ratios in the Gams sequence are close to the analogous variations documented elsewhere [*Brinkhius et al.,* 1998; *Magaritz,* 1989; *Stuben et al.,* 2002; and others] and are pronounced most similarly to the variations in the El Kef sequence in Tunisia and Agost sequence in southeastern Spain [*Keller et al.,* 1995; *Rodrigues-Tovar et al.,* 2004]. The temperature variations still are to be evaluated by the isotopic composition of the organogenic carbon in the skeletons of the foraminifers.

[139] Our data on the He isotopic composition of material in transitional layer J (both on whole-rock and clay-fraction samples) indicate that the $^3He/^4He$ ratio has the atmospheric values, which provides additional evidence for the contribution of the terrigenous component during the sedimentation. At the same time, it will be interesting to further examine in more detail the upper part of layer J in the context of the problem of fullerenes [*Heymann et al.,* 1994, 2001], whose $^3He/^4He$ ratio in sediments at the Permian/Triassic boundary is two orders of magnitude higher than the atmospheric value [*Becker et al.,* 2001].

[140] 4. The distribution of foraminifers in the Cretaceous–Paleogene transitional beds in the Gams section shows that the extinction of foraminifer genera began well before the accumulation of the layer J.

[141] The genera *Gansserina, Kuglerina*, and *Helvetiella* consecutively disappeared in the interval A–I. The greatest number of genera (*Abathomphalus, Globotruncanella*, and *Contusotruncana*) were extinct simultaneously just prior to the accumulation of layer J and else two genera *Globigerinelloides* and *Rugoglobigerina* probably emigrated from this region. In its lower part the foraminifer assemblage is impoverished and is represented by typical Cretaceous genera *Globotruncana, Globotruncanita, Heterohelix, Racemiguembelina, Pseudotextularia*, and *Hedbergella*. Only two genera, *Globotruncanita* and *Pseudotextularia*, were extinct there; the benthic foraminifers remained significantly diverse.

[142] In the middle part of layer J (sample J-8/9b) planktonic and benthic foraminifers are missing. The upper part of layer J (sample J-8/9c) contains an impoverished planktonic assemblage dominated by typical Cretaceous Heterohelicidae members (genera *Racemiguembelina* and *Heterohelix*) and only genus *Racemiguembelina* disappeared to the top of this level. Few *Globotruncana* still occurred and rare typical Paleogene *Globoconusa dawbjiergensis* appeared. The benthic foraminiferal assemblage is slightly impoverished though rather diverse.

[143] In the upper part of the section (units L–W) planktonic foraminifers are scarce; the assemblages yield small Paleogene-like forms. The last typical Cretaceous genera *Globotruncana* disappeared in unit M; the last *Heterohelix*, in unit Q.

[144] Our investigation showed that in the Gams section the so-called "mass extinction" of foraminifers in the terminal Cretaceous resulted in the disappearance of three genera. The rest genera were gradually extinct below the transitional bed and above it.

Conclusions

[145] The results obtained for the Gams sequence allowed us to draw the following conclusions:

[146] 1. For the first time it was demonstrated that the evolution of the transitional layer at the Cretaceous–Paleogene boundary had proceeded in two stages.

[147] During the earlier one (which lasted approximately 1500 years, assuming conservative estimates for the sedimentation rate), the transitional layer was formed by volcanic aerosol, which was responsible for the presence of titanomagnetite, Au, Cu, and for high concentrations of Ir, As, Cr, Br, and some other elements. The occurrence of an Ir anomaly in the lower part of the transitional layer was caused by volcanic activity (which also resulted in the presence of titanomagnetite, copper, and gold). The idea that Ir anomalies could be related to volcanic activity was previously expressed with reference to the Deccan flood basalts [*Bajapai and Prasad,* 2000; *Crocket and Paul,* 2004; *Tandon,* 2002].

[148] During the other stage, the character of sedimentation was affected by the fall of an asteroid (meteorite), whose material was detected in the form of trace amounts of metallic Ni, awaruite, and diamond crystals.

[149] 2. The study of distribution of planktonic foraminiferal assemblages inhabiting different levels of the water column including subsurface, thermocline, and sub-thermocline waters, and of their dominating taxa revealed that in the terminal Maastrichtian the species strongly prevailed in subsurface and thermocline waters. This indicates unstable conditions with frequently changing food resources, which repeatedly increased alternately in thermocline and subsurface waters.

[150] We can also suggest that at the early stage of the layer J (unit J-8/9a) (see Table 1) accumulation the thermocline and subthermocline environmental conditions were sharply deteriorated. During the deposition of unit J-8/9b

the conditions became still worse and in addition to thermocline layers the subsurface, subthermocline (deep), and bottom waters became uninhabited. All water environment appeared to be completely unsuitable for existence of planktonic and benthic foraminifers. That deterioration could result from an input of arsenic and other siderophile elements as volcanic activity products in water, which resulted in arsenious pollution of water environment.

[151] Our conclusions principally differ from all preexisting interpretations of the transitional layer at the boundary between the Cretaceous and Paleogene and make it possible to resolve the problem of the reasons for the mass extinction of living organisms at 65 Ma. Our research eliminates the need in opposing volcanism to an impact event, because both of them took place, but the changes in the biota were related to volcanism, as also was the appearance of the Ir anomaly itself. The cosmic body fell only some 500–800 years later!

[152] In conclusion, we would like to quote W. Alvarez who wrote that "...the time for unbridled speculation is past" [*Alvarez et al.,* 1984, p. 1186].

References

Abramovich, S., G. Keller, D. Stuben, and Z. Berner (2003), Characterizaton of late Campanian and Maastrichtian planktonic forminiferal depth habitats and vital activities based on stable isotopes, *Palaeogeogr. Palaeoclimatol. Palaeoecol., 202,* 1.

Alvarez, W. (2002), Compiliny the evidence for impact at seven mass extinctions, in *Impacts and the origin, evolution and extinction of life, A Rubey Colloquim,* p. 66, Univ. California, Los Angeles.

Alvarez, L. W., W. Alvarez, F. Asaro, and H. V. Michel (1980), Extraterrestrial cause for the Cretaceous-Tertiary extinction, *Science, 208,* 1095.

Alvarez, W., L. W. Alvarez, F. Asaro, and H. V. Michel (1984), The end of the Cretaceous: sharp boundary or gradual transition?, *Science, 223,* 1183.

Alvarez, W., J. Smit, W. Lowrie, and A. Asaro (1992), Proximal impacts deposits at the Cretaceous-Tertiary boundary in the Gulf of Mexico: a restudy of DSDP Leg 77, Sites 536 and 540, *Geology, 20,* 697.

Bajapai, S., and G. V. R. Prasad (2000), Cretaceous age for Ir-rich Deccan intertrappen deposits: paleontological evidence from Anjar, western India, *J. Geol. Soc. London, 157,* 257.

Becker, L., R. J. Poreda, A. G. Hunt, and Th. E. Bunch (2001), Rampino M. Impact event at the Permian-Triassic boundary: evidence from the extraterresdtrial noble gases in fullerenes, *Science, 291,* 1530.

Biskaye, P. E. (1965), Mineralogy and sedimentation of recent deep-sea clay in the Atlantic Ocean and adjacent seas and oceans, *Geol. Soc. Am. Bull., 73,* 803.

Bohor, B. F., E. E. Foord, and P. J. Modreski (1984), Triplehorn D.M. Mineralogic evidence for an impact event at the Cretaceous-Tertiary boundary, *Science, 224,* 867.

Bokii, G. B., G. N. Bezrukov, Yu. A. Klyuev, A. M. Neletov, and V. I. Nepsha (1986), *Natural and Synthetic Diamonds,* 221 pp., Nauka, Moscow.

Bolli, H. M. (1966), Zonaton of Cretaceous to Pliocene marine sediments based on planktonic foraminifera, Assoc, *Venez. Geol. Min. Petrol. Bol. Inform., 9,* 2.

Brinkhuis, H., and W. J. Zachariasse (1988), Dinoflagellate cysts, sea level changes and planktonic foraminifers across the Cretaceous/Tertiary boundary at El-Haria, northwest Tunisia, *Mar. Micropaleont., 13,* 153.

Brinkhuis, H., J. P. Bujak, J. Smit, G. J. M. Versteegh, and H. Visscher (1998), Dinoflagelatte-based sea surface temperature reconstructions across the Cretaceous-Tertiary boundary, *Palaeogeogr. Palaeoclimatol. Palaeoecol., 141,* 67.

Burov, B. V., D. K. Nurgaliev, and P. G. Yasonov (1986), *Paleomagnetic Analysis,* 167 pp., Kazan Gos. Univ., Kazan.

Carlisle, D. B., and D. R. Braman (1991), Nanometre-size diamonds in the Cretaceous-Tertiary boundary clay of Alberta, *Nature, 352,* 708.

Cowie, J. W., W. Ziegler, and J. Remane (1989), Stratigraphic Commission accelerates progress, 1984–1989, *Episodes, 112,* 79.

Crocket, J., and D. K. Paul (2004), Platinum-group elements in Deccan mafic rocks: a comparison of suites differentiated by Ir content, *Chem. Geol., 208,* 273.

Deconinck, J. F., M. M. Blanc-Valleronb, J. M. Rouchyb, G. Camoinc, and D Badaut-Trauthb (2000), Palaeoenvironmental and diagenetic control of the mineralogy of Upper Cretaceous–Lower Tertiary deposits of the Central Palaeo–Andean basin of Bolivia (Potosi area), *Sediment. Geol., 132,* 263.

Dolenec, T., J. Pavsic, and S. Lojen (2000), Ir anomalies and other elemental markers near the Palaeocene-Eocene boundary in a flysch sequence from the Western Tethys (Slovenia), *Terra Nova, 12,* 199.

Dubinin, A. V. (1993), Inductively coupled plasma mass spectrometry: determinations of REE in standard references samples of oceanic deposits, *Geokhimia* (in Russian), *24*(11), 1605.

Ellwood, B. D., W. D. MacDonald, C. Wheeler, and S. L. Benoist (2003), The K/T boundary in Oman: identified using magnetic susceptibility field measurements with geochemical information, *Earth Planet. Sci. Lett., 206,* 529.

Ganapathy, R., S. Gartner, and M.-J. Jiang (1981), Iridium anomaly at the Cretaceous-Tertiary boundary in Texas, *Earth Planet. Sci. Lett., 54,* 393.

Gardin, S. (2002), Late Maastrichtian to early Danian calcareous nannofossils at Elles (Northwest Tunisia), A tale of one million years across the K-T boundary, *Palaeogeogr. Palaeoclimatol. Palaeoecol., 178,* 211.

Grachev, A. F. (2000a), Mantle plumes and problems of geodynamics, *Fizika Zemli* (in Russian), *36*(4), 3.

Grachev, A. F. (2000b), Geodynamic reasons for global catastrophes, *Zemlya i Vselennaya* (in Russian), (5), 13.

Graup, G., and B. Spettel (1989), Mineralogy and phase-chemistry of an Ir-enriched pre-K/T layer from the Lattengebirge, Bavarian Alps, and significance for the KTB problem, *Earth Planet. Sci. Lett., 95,* 271.

Hardenbol, J., J. Thierry, M. B. Farrey, T. Jacquin, P.-Ch. Graciansky, and P. R. Vail (1998), Cretaceous sequence chronostratigraphy (chart 4), Cenozoic biostratigraphy (chart 3), *SEPM, Spec. Publ., 60,* 150.

Herm, D., A. Hillebrandt, R. Hofling, E. Martini, and K. Perch-Nielsen (1981), Exkurtion E. Lattengebirge und Untersberg-Vorland, *Geol. Bavarica, 82,* 181.

Heymann, D., L. P. Felipe Chibanre, R. R. Brooks, W. S. Wolbach, and R. E. Smalley (1994), Fullerenes

in the Cretaceous-Tertiary boundary layer, *Science, 265,* 645.

Hildebrand, A. R.,   G. T. Penfield,   and D. A. Kring (1991), Chicxulub crater: a possible Cretaceous-Tertiary boundary impact crater on the Yucatan peninsula, Mexico, *Geology, 19,* 867.

Hough, R. M., I. Gilmour, C. T. Pillinger, F. Langerhorst, and A. Montanari (1997),   Diamonds from the iridium-rich K/T boundary alyer at Arroyo el Mimbral, Namaulipas, Mexico, *Geology, 25,* 1019.

Hsu, K. J.,   Q. He,   and A. McKenzie (1982),   Mass mortality and its environmental and evolutionary consequences, *Science, 216,* 249.

Jones, A. P.,   D. G. Price,   P. S. DeCarli,   N. Proce,   and R. Clegg (2003),   Impact decompression melting: a possible trigger for impact induced volcanism and mantle hotspots?, in *Impact Markers in the Stratigraphic Record,* edited by C. Koeberl and F. Martinez-Ruiz*,* p. 91, Springer, Berlin.

Kamensky, I. L.,   I. N. Tolstikhin,   and V. R. Vetrin (1990), Juvenile Helium in Ancient Rocks: I, [3]He Excess in Amphiboles from 2.8 Ga Charnokite Series–Crust-Mantle Fluid in Intracrustal Magmetic Processes, *Geochim.   Cosmochim. Acta, 54,* 3115.

Keller, G. (1988),   Extinction, survioship and evolution of planktonic foraminifera across the Cretaceous/Tertiary boundary at El-Kef, Tunisia, *Mar. Micropaleontol., 13,* 239.

Keller, G. (2002),   *Guembelitria*-dominated late Maastrichtian planktic foraminiferal assemblages mimic early Danian in central Egypt, *Mar. Micropaleontol., 47,* 71.

Keller, G.,   L. Li,   and N. MacLeod (1996),   The Cretaceous/ Tertiary boundary stratotype section at El-Kef, Tunisia: how catastrophic was rhe mass extinction?, *Palaeogeogr. Palaeoclimatol. Palaeoecol., 119,* 221.

Keller, G.,   and W. Stinnesbeck (2000),   Iridium and the K/T boundary at El Caribe, Guatemala, *Int. J. Earth Sci., 88,* 840.

Keller, G.,   Th. Adatte,   W. Stinnesbeck,   and V. Luciani (2002),   Paleoecology of the Cretaceous-Tertiary mass extinction in planktonic foraminifera, *Palaeogeogr. Palaeoclimatol. Palaeoecol., 178,* 1.

Koebler, C. (1997),   Impact cratering: the mineralogical and geochemical evidence, in *The Ames Structure and Similar Features,* edited by K. Johnson, J. Campbell*,* p. 30, Geol. Survey Circular, Oklahoma.

Kollmann, H. A. (1964),   Stratigraphie und tectonik des Gosaubeckens von Gams (Steinmark, Osterreich), *Jb.   Geol. B.A., Bd. 107,* 71.

Krylov, A. Ya., B. A. Mamyrin, Yu. I. Silin, and L. V. Khabarin (1973),   Helium isotopes in oceanic sediments, *Geochem. Int., 10,* 202.

Kyte, F. T., and J. A. Bostwick (1995), Magnesioferrite spinel in Cretaceous/Tertiary boundary sediments of the Pacific basin: remnants of hot, early ejecta from the Chicxulub impact?, *Earth Planet. Sci. Lett., 132,* 113.

Lahodynsky, R. (1988),   Lithostratigraphy and sedimentology across the Cretaceous/Tertiary boundary in the Flyschgosau (Eastern Alps, Austria), *Riv. Espanola de Paleontologia,* no. Extraordinario, 73.

Leroux, H., R. Rocchia, and L. Froget (1995), The K/T boundary at Beloc (Haiti): compared stratigraphic distributions of the boundary markers, *Earth Planet. Sci. Lett., 132,* 255.

Lisitsyn, A. P. (1978),   *Processes of Oceanic Sedimentation,* 392 pp., Nauka, Moscow.

Luciani, V. (2002),   High-resolution planktonic foraminiferal analysis from the Cretaceous-Tertiary boundary at Ain Settara (Tunisia): evidence of an extended mass extinction, *Palaeogeogr. Palaeoclimatol. Palaeoecol., 178,* 299.

Magaritz, M. (1989),   [13]C minima follow extinction event: A clue to faunal radiation, *Geology, 17,* 337.

Molodenskii, S. M. (2005), On Stress in the Earth's Mantle during the Fall of a Large Cosmic Body, *Rus. J. Earth. Sci., 7,* 1.

Murray, R. W. (1994),   Chemical criteria to identify the depositional environment of cherts: general principales and applications, *Sediment. Geol., 90,* 213.

Nagata, T. (1965),   *Rock Magnetism,* 350 pp., Maruzen, Tokyo.

Officer, Ch. B.,   and Ch. L. Drake (1985),   Terminal Cretaceous environmental events, *Science, 227,* 1161.

Officer, Ch. B.,   A. Hallam,   Ch. L. Drake,   and J. D. Devine (1987),   Late Cretaceous and paroxysmal Cretaceous–Tertiary extinctions, *Nature, 326,* 143.

Padro, A.,   T. Adatte,   G. Keller,   and H. Oberhansli (1999), Paleoenviromental changes across the Cretaceous-Tertiary boundary at Koshak, Kazakhstan, based on planktic foraminifera and clay mineralogy, *Palaeogeogr. Palaeoclimatol. Palaeoecol., 154,* 247.

Patterson, T. R.,   A. D. Fowler,   and B. T. Huber (2004), Evidence of hierarchical organization in the planktonic foraminiferal evolutionary record, *J. Foraminiferal Res., 34,* 85.

Peryt, D.,   R. Lahodynsky,   R. Rocchia,   and D. Boclet (1993),   The Cretaceous/Paleogene boundary and planktonic foraminifera in the Flyschgosau (Eastern Alps, Austria), *Palaeogeogr. Palaeoclimatol. Palaeoecol., 104,* 239.

Phillipp, H.,   J.-D. Eckhardt,   and H. Puchelt (2001), Platinum-group elements (PGE) in basalts of the seaward-dipping reflector sequence, SE Greenland coast, *J. Petrol., 42,* 407.

Power, M. R., D. Pirrie, and J. C. O. Andersen (2003), Diversity of platinum-group element mineralization styles in the North Atlantic Igneous Province: new evidence from Rum, UK, *Geol. Mag., 140,* 499.

Preisinger, A.,   E. Zobetz,   and A. J. Gratz (1986),   The Cretaceous/Tertiary boundary in the Gosau Basin, Austria, *Nature, 322,* 794.

Preisinger, A.,   S. Aslanian,   F. Brandstatter,   F. Grass, H. Stradner,   and H. Summesberger (2002),   Cretaceous–Tertiary profile, rhythmic deposition and geomagnetic polarity of marine sediments near Bjala, Bulgaria, *Geol. Soc. Am., Special Paper, 356,* 213.

Rochette, P.,   M. Jackson,   and C. Aubourg (1992),   Rock magnetism and interpretation of anisotropy of magnetic susceptibility, *Rev. Geophys., 30,* 209.

Rodrigues-Tovar, F. J.,   F. Martinez-Ruiz, and S. M. Bernasconi (2004),   Carbon isotope evidence for the timing of the Cretaceous-Paleogene macrobenthic colonosation at the Agost section (southeast Spain), *Palaeogeogr.   Palaeoclimatol. Palaeoecol., 203,* 65.

Rosen, O. M., A. Ali, A. A. Abbyasov, and J. C. Tipper (2004), MINLITH–an experience-based algorithm for estimating the likely mineralogical compositions of sedimentary rocks from bulk chemical analyses, *Computers & Geosciences, 30,* 647.

Smit, J.,   and J. Hertogen (1980),   An extraterrestrial event at the Cretaceous-Tertiary boundary, *Nature, 285,* 198.

Smit, J.,   T. B. Roep,   W. Alvarez,   and A. Montanari (1992), Coarse grained, clastic sandstone complex at the K/T boundary around the Gulf of Mexico: deposition by tsunami waves induced by the Chicxulub impact?, *Geol.   Soc.   Am., Spec. Pap., 307,* 151.

Stinnesbeck, W., G. Keller, P. Schulte, D. Stuben, Z. Berner, U. Kramar,   and L.-O. Guadalupe (2002),   The Cretaceous-Tertiary (K/T) boundary transition at Coxquinhui, state Veracruz, Mexico: evidence for an early Danian impact event?, *J. South Am. Earth Sci., 15,* 497.

Strakhov, N. M. (1962),   *Fundamentals of the Theory of Lithogenesis,* vol. 2, 574 pp., Nauka, Moscow.

Stuben, D.,   U. Kramar,   Z. Berner,   W. Stinnesbeck,   and G. Keller (2002),   Trace elements, stable isotopes, and clay mineralogy of the Elles II K/T boundary section in Tunisia: indications for sea level fluctuations and primary productivity, *Palaeogeogr. Palaeoclimatol. Palaeoecol., 178,* 321.

Tandon, S. K. (2002),   Records of the influence of Deccan volcanism on contemporary sedimentary environments in Central India, *Sediment. Geol., 147,* 177.

Taylor, S. R.,   and S. M. McLennan (1985),   *The Continental Crust: Its Composition and Evolution,* 151 pp., Blackwell, Oxford.

Thiry, M. (2000), Palaeoclimatic interpretation of clay minerals in marine deposits: an outlook from the continental origin, *Earth Sci. Rev., 49,* 201.

Turko, R. P., O. B. Tun, T. P. Akkerman, J. B. Pollack, and L. Sagan (1984), Climatic Consequences of a Nuclear War, *V Mire Nauki* (in Russian), *(10),* 4.

Wagreich, M., and H.-G. Krenmayr (2005), Upper Cretaceous oceanic red beds (CORB) in the Northern Calcareous Alps (Nierental Formation, Austria): slope topography and clastic input as primary controlling factors, *Creataceous Res., 26,* 57.

White, R. V., and A. D. Saunders (2005), Volcanism, impact and mass extinctions: incredible or credible coincidences?, *Lithos, 79,* 299.

Yasonov, P. G., D. K. Nourgaliev, B. V. Bourov, and F. Heller (1998), A modernized coercivity spectrometer, *Geologica Carpathica, 49,* 224.

Zhao, Z. K., X. Y. Mao, Z. F. Chai, G. Ch. Yang, P. Kong, M. Ebihara, and Z. H. Zhao (2002), A possible causal relationship between extinction of dinosaurs and K/T iridium enrichment in the Nanxiong Basin, South China: evidence from dinosaur eggshells, *Palaeogeogr. Palaeoclimat. Palaeoecol., 178,* 1.

Zhou, L., and F. T. Kyte (1988), The Permian-Triassic boundary event: a geochemical study of three Chinede sections, *Earth Planet. Sci. Lett., 90,* 411.

Zoller, W. H., J. R. Parrington, and J. M. P. Kotra (1983), Iridium enrichment in airborne particles from Kilauea volcano: January 1983, *Science, 222,* 1118.

A. F. Grachev, D. M. Pechersky, V. A. Tsel'movich, Institute of Physics of the Earth, Russian Academy of Science, 10 Bol'shaya Gruzinskaya ul., Moscow, 123995 Russia

H. A. Kollmann, National Museum of Natural History, Vienna, Austria

O. A. Korchagin, Geological Institute, Russian Academy of Science, 7 Pyzhevskii per., Moscow, 119017 Russia